

Flow Characteristics in Abdominal Aortic Aneurysms: An *in vitro* Study

Shahrzad Norouzi

A Thesis
in
The Department
of
Mechanical, Industrial & Aerospace Engineering

Presented in Partial Fulfillment of the Requirements
For the Degree of
Master of Applied Science (Mechanical Engineering) at
Concordia University
Montréal, Québec, Canada

November 2020

© Shahrzad Norouzi, 2020

**CONCORDIA UNIVERSITY
SCHOOL OF GRADUATE STUDIES**

This is to certify that the thesis prepared

By: Shahrzad Norouzi

Entitled: Flow Characteristics in Abdominal Aortic Aneurysms:
An *in vitro* Study

and submitted in partial fulfillment of the requirements for the degree of

Master of Applied Science (Mechanical Engineering)

complies with the regulations of the University and meets the accepted standards with respect to originality and quality.

Signed by the final examining committee:

_____	Chair
Dr. Carole El Ayoubi	
_____	Examiner
Dr. Carole El Ayoubi	
_____	Examiner
Dr. Rolf Wuthrich	
_____	Thesis Supervisors
Dr. Lyes Kadem, Dr. Giuseppe Di Labbio	

Approved by _____
Dr. Mamoun Medraj, MASC Program Director

November 2020

Dr. Mourad Debbabi, Dean
Gina Cody School of Engineering & Computer Science

ABSTRACT

Flow characteristics in abdominal aortic aneurysms: an *in vitro* study

Shahrzad Norouzi

An abdominal aortic aneurysm (AAA) is a vascular disorder that emerges when the aortic wall degenerates and the abdominal aorta undergoes a permanent expansion of at least 1.5 times its normal diameter. If an AAA is left undiagnosed and untreated, it can eventually rupture with an associated mortality risk of 81%. Clinically, a maximum diameter exceeding 5 cm is considered the decisive criterion to identify at-risk AAAs. The present work investigates the flow dynamic variations associated with aneurysm experimentally, using compliant AAA models and time-resolved particle image velocimetry (TR-PIV). For this purpose, an *in vitro* setup is designed and developed to simulate the flow inside 6 idealized phantoms mimicking *in vivo* physiological properties. The instantaneous flow fields in two orthogonal planes reveal that the flow behavior in the early stages of an aneurysm does not deviate significantly from that of the healthy aorta. An increase in the size and number of bulges triggered the evolution of features such as flow detachment, swirling motion, wall impingement and the collapse of the vortical structures within the aneurysm sac. All these characteristics are more noticeable in the AAA model with a maximal diameter equal to the clinical threshold. Therefore, in the context of fluid dynamics, this perception can provide physical support to the $D_{\max}=5$ cm criterion to nominate an AAA patient for elective surgery. It is assumed that the onset and propagation of large vortical structures in the deceleration phase and the formation of stagnant flow regions near the proximal neck of the largest model can lead to unfavorable hemodynamic changes that escalate the weakening, enlargement and rupture of the aortic wall. Following recent applications of viscous energy dissipation in the severity stratification of cardiovascular diseases, as part of this thesis, the associated energy loss is quantified in order to examine its correlation with changes in the geometry and flow topology of each model. Although the two largest models were identified with the highest energy losses, which can be attributed to their higher shear stresses, this parameter does not follow a clear increase with the aneurysm expansion. In the other four cases, the kinetic energy was almost equally well preserved. The experimental AAA flow data in this work is also inspected from a modal analysis perspective, in particular proper orthogonal decomposition (POD), to identify and extract the dominant structures, which can provide more insights on the disease progression. The Shannon (global) entropy demonstrates that as the aneurysm expands, the modal energy distribution becomes dispersed, meaning that more modes are required to describe and model the flow. This parameter, in turn, can potentially be applied in clinical assessment of the severity of patient-specific AAAs.

ACKNOWLEDGEMENTS

*“There is no real ending.
It’s just the place where you stop the story.”*
Frank Herbert

My master’s story has a principal character, Dr. Lyes Kadem, who approved my request to join his team and be the narrator of this thesis. Lyes, I am grateful to you for everything you have done for me. For your patience, understanding and genuine care. Thank you for making me always feel comfortable to walk to your office with questions, suggestions and challenges; sorry for the inadequate supply of high-quality Swiss-made dark chocolate. After all, thank you for letting me be brave and push myself beyond my limits. When I started working in the LCFD, I was a novice with little hands-on experience. You gave me the time, resources and confidence to become independent, confront my problems and explore different ideas, all the while learning so many new skills. I owe to you what I have accomplished and truly hope that I can return the favor in some way in the future.

Special thanks to Dr. Giuseppe Di Labbio for making research more appealing and fundamental to me. Giuseppe, you are gifted at providing a straightforward explanation of everything from its concept to the implementation. Thank you for always answering my questions. They resolved some main conflicts in this story. I hope that the final resolution can at least partially reflect these efforts.

This story could not have gone on without the generous help and compassion of our lab members. The LCFD gave me the chance to work and make unforgettable memories with amazing people. I want to thank Mahdis for being a super kind and caring friend, Amanda, for being a patient listener, Ghassan, for being supportive and cheerful, Ahmed, for his immense help, Max, for his positive vibes, and Maziar, for his tolerance. Also, sincere gratitude to Marzieh for keeping me company during the hard times. You can indeed be awarded honorary membership of the LCFD.

Finally, and above all, I could not have come this far without the affirmation and encouragement I received from my lovely Maman, my awesome Babajaan, my sweet Sharare, and my charming Shayan. At the very beginning, it was so unbelievable to be away from home for more than a week, as in your presence, I was never alone. Your words were the best remedy and incentive to keep moving forward. Thank you for your unconditional love and support. I love you and see you soon.

And, a tip for future members of the LCFD; do not be afraid to embrace your ideas. You can learn and progress incredibly if you keep being curious and resilient.

CONTENTS

List of Figures	viii
List of Tables	ix
Acronyms	xi
Nomenclature	xii
1 INTRODUCTION	1
1.1 Cardiovascular System	1
1.2 Abdominal Aortic Aneurysm	1
1.2.1 Epidemiology	2
Prevalence of AAAs	2
Initiation of AAAs	3
1.2.2 Natural history	5
Risk factors	5
1.2.3 Complications	6
Rupture	6
Intraluminal Thrombus	6
Renal failure	6
1.2.4 Diagnosis	6
Symptoms	6
Imaging techniques	7
1.2.5 Management	7
Management of small aneurysms	7
Threshold for elective repair	8
Elective AAA repair	8
1.3 Thesis Outline	10
2 RELEVANT WORKS	11
2.1 AAA Flow Characterization	11
2.1.1 Summary of <i>in vivo</i> studies	11
2.1.2 Summary of <i>in vitro</i> studies	12
2.1.3 Summary of <i>in silico</i> studies	15
2.2 AAA Flow Patterns	15
2.2.1 Flow features in the normal abdominal aorta	15
2.2.2 Flow features in the abdominal aortic aneurysm	16
2.3 AAA Energy Loss	17
2.4 Modal Analysis	18
2.5 AAA Rupture Assessment	19
2.6 Thesis Objectives	20
3 METHODOLOGY	21
3.1 Experimental Apparatus	21
3.1.1 Flow circulatory system	21
3.1.2 Pressure and flow measurements	25

3.1.3	Replica of the aorta and AAAs	26
3.1.4	Blood-mimicking fluid	29
3.2	Particle Image Velocimetry	30
3.2.1	Basic principles	31
3.2.2	Implementation	31
Tracer particles		31
Optical system and recording parameters		33
3.3	Post-Processing	35
3.3.1	Velocity vector computation	36
Vector validation		36
Uncertainties		37
3.3.2	Velocity gradients calculation	37
3.3.3	Viscous energy dissipation	38
3.3.4	Proper orthogonal decomposition	39
POD implementaion		39
Shannon entropy		41
4	RESULTS	42
4.1	Instantaneous Velocity Fields	42
4.2	Energy Loss Analysis	46
4.2.1	Statistical analysis	48
4.3	Modal Decomposition	49
4.3.1	Data reduction with POD	55
5	CONCLUSION	59
5.1	Recommendations	60
	Bibliography	70

LIST OF FIGURES

Figure 1.1	Human aorta: a) position of the aorta within the body; b) selected segments of a normal aorta; c) abdominal aortic aneurysm (AAA). Reproduced from Emory School of Medicine	2
Figure 1.2	Simplified sketch of fusiform and saccular aneurysms with structured layers of the aorta. Reproduced from Sakalihan et al. (2018)	3
Figure 1.3	Elective repair methods for an abdominal aortic aneurysm: a) open surgical method (OSR); b) endovascular aneurysm repair (EVAR). Reproduced from Sakalihan et al. (2018)	9
Figure 1.4	EVAS repair for an infrarenal abdominal aortic aneurysm which uses endobag insufflation to seal the aneurysm. Reproduced from Brownrigg et al. (2015)	10
Figure 3.1	Schematic representation of the simulator.	22
Figure 3.2	Components and configuration of the experimental setup.	23
Figure 3.3	Distortion test. Left: flexible sheet with polka-dot pattern, outside the box. Right: the target device placed inside the AAA filled with the mixture. The image intensity is low since it is recorded via the high speed camera when the laser was switched off.	24
Figure 3.4	Acquired waveforms for the flow and the pressure for the normal case. Left: instantaneous flow rate at the inlet of the test section. Right: instantaneous pressure measured at 4 cross-sections: 1) right above the aortic valve; 2) upstream of the renal arteries; 3) in the proximal region of the aneurysm; 4) close to the aortic bifurcation.	25
Figure 3.5	Dimensions and planar view of the 3D printed models that were used to fabricate the silicone phantoms.	27
Figure 3.6	Fabrication process of a sample AAA silicone model.	29
Figure 3.7	Principle concept of velocity vector computation in a 2D planar PIV system.	32
Figure 4.1	Healthy abdominal aortic flow. Left: peak systole. Right: mid-diastole.	43
Figure 4.2	Flow in the model with a short aneurysm. Upper row: sagittal plane. Bottom row: coronal plane.	44
Figure 4.3	Velocity vectors in the fusiform and bi-lobed aneurysms. Upper row: sagittal plane. Bottom row: coronal plane.	45
Figure 4.4	Velocity vectors in the most severe case (d5.3A). Upper row: sagittal plane. Bottom row: coronal plane.	46
Figure 4.5	Viscous energy dissipation rate. Left: sagittal plane. Right: coronal plane. (The non-dimensionalized time, $t^* = \frac{t}{T}$, is defined such that $t^* = 0$ and $t^* = 1$ correspond to the beginning of systole and end of systole, respectively.)	47
Figure 4.6	Total viscous energy loss for all the cases. Left: sagittal plane. Right: coronal plane.	48

Figure 4.7	The energy spectra for the first 10 POD modes. Left: sagittal plane. Right: coronal plane.	49
Figure 4.8	The first and the second POD mode and the corresponding temporal coefficients for n.Ao in the sagittal plane. The scale for the spatial distribution of the POD modes in all the related figures is accompanied by "unit" since the modes are normalized and do not have unit.	50
Figure 4.9	The first and the second POD mode and the corresponding temporal coefficients for d3.3A for the sagittal plane.	51
Figure 4.10	The first and the second POD mode and the corresponding temporal coefficients for s.3A. Upper row: sagittal plane. Bottom row: coronal plane.	51
Figure 4.11	The first and the second POD mode and the corresponding temporal coefficients for bi.3A. Upper row: sagittal plane. Bottom row: coronal plane.	52
Figure 4.12	Spatial distribution of the first 3 POD modes for d4.3A. Upper row: sagittal plane. Bottom row: coronal plane.	53
Figure 4.13	Spatial distribution and temporal coefficients of the first 4 POD modes for d5.3A. Upper row: sagittal plane. Bottom row: coronal plane.	54
Figure 4.14	Global entropy for all the cases. Left: sagittal plane. Right: coronal plane.	54
Figure 4.15	Power spectral density for POD modes of n.Ao and d5.3A in the sagittal plane. The vertical axis, power spectral density (PSD), demonstrates the intensity of the variations as a function of frequency.	55
Figure 4.16	Accumulated fraction of total kinetic energy as function of the number of modes. Left: sagittal plane. Right: coronal plane.	56
Figure 4.17	Velocity vector field at 4 snapshots for d5.3A and its truncated model with 98% KE. The vortex ring core trajectory is identified through vorticity contour maps.	57
Figure 4.18	Performance of the truncated model to capture 98%, 99%, and 99.9% in modelling energy loss.	58

LIST OF TABLES

Table 3.1	Summary of the experimental conditions.	35
Table 4.1	Summary of the AAA model features.	42
Table 4.2	One-way ANOVA results for total energy loss as the variable of interest.	49
Table 4.3	Required number of modes for the reconstruction based on the percentage of kinetic energy to preserve.	56

ACRONYMS

AAA	abdominal aortic aneurysm
ANOVA	analysis of variance
AR	aortic regurgitation
CDFI	colour Doppler flow imaging
CDU	colour Doppler ultrasound
CFD	computational fluid dynamics
CT	computed tomography
DUS	duplex ultrasonography
DUV	Doppler ultrasound velocimetry
EVAR	endovascular aneurysm repair
EVAS	endovascular aneurysm sealing
HFR CEUS	high frame rate contrast material enhanced US
ILT	intraluminal thrombus
IR	infrarenal
KE	kinetic energy
LDV	laser Doppler velocimetry
LV	left ventricle
MR	magnetic resonance
OSI	oscillatory shear index
OSR	open surgical repair
PC-MRI	phase-contrast magnetic resonance imaging
PIV	particle image velocimetry
PLA	Polylactic acid
POD	proper orthogonal decomposition
PWV	pulse-wave-velocity
RI	refractive index
SC	supraceliac
SMCs	smooth muscle cells
SPOD	spectral proper orthogonal decomposition
SVD	singular value decomposition
TPU	thermoplastic polyurethane

TR-PIV	time-resolved particle image velocimetry
US	ultrasound
VECs	vascular endothelial cells
VFM	vector flow mapping
WSS	wall shear stress

NOMENCLATURE

Latin

\mathbf{X}	Snapshot matrix
C	Temporal correlation matrix
d_p	Particle diameter (m)
D_{\max}	Maximum anteroposterior diameter (m)
f	Frequency (Hz)
H	Shannon (global) entropy
n	Number of PIV image pairs
p_i	Ratio between the eigenvalue and the global energy
Q_m	Infrarenal flow rate (L/min)
R	Covariance matrix
Re	Reynolds number
S	Strain rate (1/s)
Stk	Stokes number
T	Cardiac period (s)
t	Time (s)
t^*	Non-dimensionalized time ($\frac{t}{T}$)
u	Velocity component in the x direction (m/s)
V	Velocity vector (m/s)
v	Velocity component in the y direction (m/s)
$VEDr$	Viscous dissipation rate (W/m^3)
Wo	Womersely number

Greek

λ_j, Λ	Eigenvalue
μ	Dynamic viscosity (Pa.s)
ν	Kinematic viscosity (m^2/s)
ϕ_j, ϕ	POD mode
ψ_j, Ψ	Eigenvector

ρ	Density (kg/m^3)
τ	Viscous stress (Pa)
τ_p	Particle response time (s)
w	Vorticity (1/s)
w_z	Out-of-plane vorticity component (1/s)

1

INTRODUCTION

1.1 CARDIOVASCULAR SYSTEM

The cardiovascular system is essentially comprised of the heart, a hollow muscle lying at the center of the chest, and a closed circuit of vessels divided into two independent networks; the pulmonary and systemic circulations. The former is a loop through the lungs to replenish the poorly oxygenated blood and send it back to the heart. The blood rich in oxygen is then pumped and leaves the left ventricle through the aortic valve. The timing of ejection is regulated via the electrical system maintaining a regular rhythm and heartbeat. At each time a pressure pulse is generated and the flow with a mean forward impulsion propagates along the aorta and continues its journey to transport nutrients and waste material to and from the rest of the body within the systemic circulation.

The aorta is the main, and largest elastic artery. It begins at the top of the left ventricle with a short ascending length that is connected to an arch over the root of the left lung. It then descends within the thorax down to the diaphragm, where the descending thoracic aorta ends and the abdominal aorta begins. The abdominal aorta then branches toward each leg at the iliac bifurcation.

1.2 ABDOMINAL AORTIC ANEURYSM

An aneurysm is most commonly defined as a permanent dilation of an artery with a diameter that is at least 1.5 times larger than its normal adjacent diameter. Compared to the alternatives, this definition provides an inclusive basis since it is irrespective of gender, underlying etiology and location of the lesion (Wanhainen et al., 2019). Based on their morphology and location, aneurysms are classified as either fusiform or saccular. Saccular aneurysms have a berry-like shape, and dilation occurs only in one segment of the artery so that the opposing walls remain intact. They are frequently observed in the main arteries of the cerebral circulation. On the other hand, fusiform aneurysms have a spindle-like shape, and the artery is evenly dilated around its circumferential wall. Fusiform aneurysms are often found upstream of major branch points along the aorta like in the abdomen, which is known as an abdominal aortic aneurysm or triple-A (AAA) (Lasheras, 2007). The majority of AAAs evolve in the infrarenal segment downstream of the renal arteries' origin. However, they can also develop above or just below the renal ostia, namely, suprarenal and juxtarenal. A schematic drawing of the normal aorta and the infrarenal aortic aneurysm is shown in Fig. 1.1.

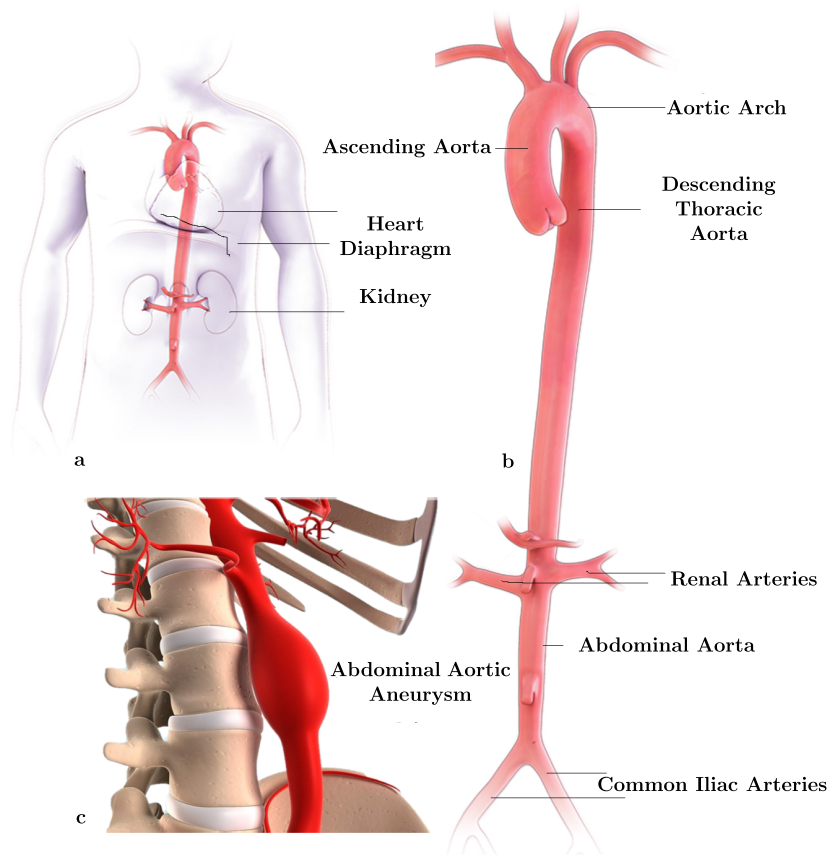


Figure 1.1: Human aorta: a) position of the aorta within the body; b) selected segments of a normal aorta; c) abdominal aortic aneurysm (AAA). Reproduced from [Emory School of Medicine](#).

1.2.1 Epidemiology

With ageing, to keep the structural integrity and to endure the wall stress, the living components of the arterial wall must continuously regenerate and remodel. In some cases, this regulatory system does not function properly, leading to an irreversible dilation of the arterial wall, formation of an aneurysm and potentially to its rupture. The potential risk of death due to the rupture and a subsequent internal bleeding is up to 81% ([Owens et al., 2019](#)).

Prevalence of AAAs

In screening studies, the prevalence of abdominal aortic aneurysms is 4-8% ([Ashton et al., 2007](#)). Annually, between 2.5 to 6.5 cases per 1000 people are diagnosed with a new AAA ([Wilmink et al., 2001](#)). Australia, North America and Western Europe report a higher rate of AAAs while in Latin America and Central Asia, fewer AAA cases were diagnosed. In Canada, the annual estimated number of patients with an AAA is 20,000, with 1244 annual deaths reported between 2009 and 2013 being attributed to AAAs and their fatal complications ([on Preventive Health Care, 2017](#)).

There are numerous risk factors associated with the dilation of the abdominal aortic wall including but not limited to the male gender, age and smoking. The risk of AAA formation is significantly

higher after the age of 55-60, and most studies show that men are up to four times more vulnerable to have this disorder than women. According to Wang et al. (2018a) in patients over the age of 65, 5% of men suffer infrarenal AAAs while the incidence rate is 1.7% in women. How different risk factors affect abdominal aortic aneurysms will be explained in more detail in Sec. 1.2.2.

Initiation of AAAs

In a healthy state, the vessel wall is made up of three well-structured layers: intima, media and adventitia (Fig. 1.2). The intima, or the inner layer, consists of a single layer of vascular endothelial cells (VECs) that lines the entire circulatory system. The media consists primarily of concentric layers of smooth muscle cells (SMCs) separated by layers of elastin fibres. Most of the wall's mechanical properties, including its elasticity, are determined through the media components. In fact, the smooth muscle cells within the media regulate the contraction and dilation of the arteries to adjust the demanded blood volume by the tissue. The adventitia, or the outer layer, is mainly composed of collagen fibres with a minor percentage of elastin fibres.

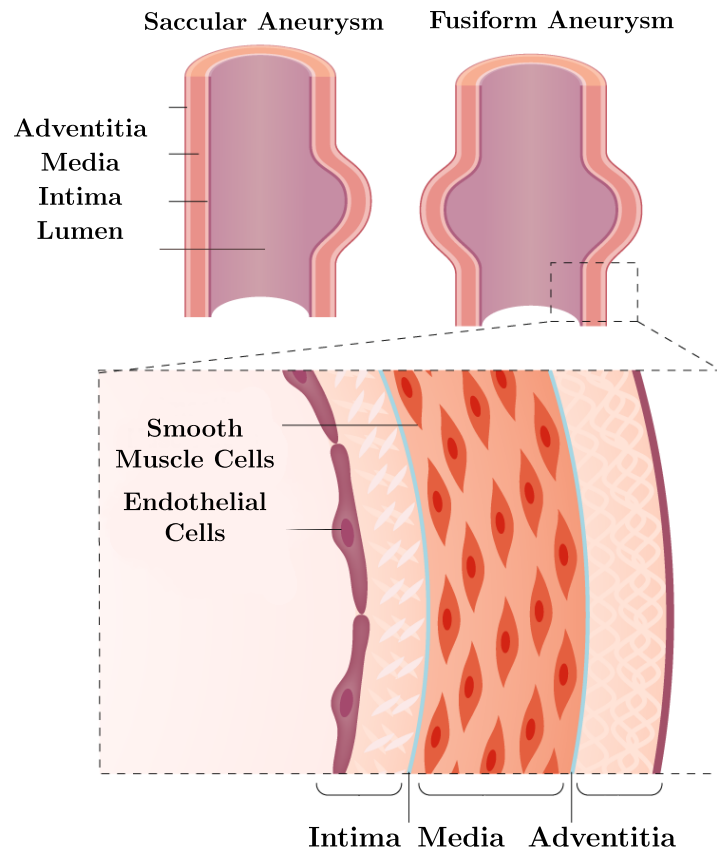


Figure 1.2: Simplified sketch of fusiform and saccular aneurysms with structured layers of the aorta. Reproduced from Sakalihan et al. (2018).

Elastin is a protein correlated with the wall's elasticity and is organized as sheets and fibres in connective tissue. In contrast, the vessel wall's stiffness is attributed to its collagen content, which is the main protein of connective tissue. On average, the respective composition ratio of collagen,

elastin and smooth muscle for a healthy wall is 54.7%, 22.7% and 22.6% (He and Roach, 1994). However, the percentage of elastin is higher for the aortic arch and thoracic aorta compared to the abdominal aorta (Dua and Dalman, 2010), which means that the abdominal aorta is less elastic and more vulnerable to any deformation, thus being prone to the formation of an aneurysm. In most AAA patients, and contrary to the normal aorta, the structural protein content of AAAs is not easily discerned (Kemmerling and Peattie, 2018) because wall layers are disorganized, tortuous and fragmented with an extensive overlap of the elastin, collagen and smooth muscle components within the wall.

What promotes AAAs to form is not yet clearly understood. However, since the first report of the disease in the 16th century, various hypotheses have been proposed that associate the origine of AAAs to aortic inflammatory diseases, hereditary connective tissue disorders, infectious diseases, degradation of the aortic wall and biochemical wall stress. An out-dated speculation was that infection on the arterial wall due to syphilis could lead to aneurysm formation. However, it is no longer regarded as an explanation since the primary causes of the infection on the wall of the artery are now quite rare. At the same time, AAAs are still very common and highly lethal. Currently, the most accepted hypothesis is that the formation of AAAs is multifactorial, resulting from a complex interaction between structural changes in the vessel wall and specific changes in hemodynamics that disrupt this otherwise stable system causing debilitation and gradual expansion of a portion of the abdominal aortic wall (Lasheras, 2007).

Many studies postulate that ageing plays a crucial role in changing the wall's structural composition. The median layer thins out by getting older, elastin content is reduced by up to 90%, and the wall becomes less compliant and distensible (He and Roach, 1994). When the wall becomes stiffer, pressure waves move down the vessel at an elevated speed. Also, a reduction in the ratio between the cross-sectional area of the iliac arteries and the parent aortic vessel fortifies the wave reflection at the bifurcation, which induces hemodynamic changes. All together, increased pulse wave speed and higher amplitude of the reflected wave lead to a rise in peak systolic pressure. As a result, the stress on the wall increases, and the tissue cannot endure the pressure and pulse deformation, losing its integrity, which accelerates the fragmentation of elastic sheets in the median layer. This process initiates a positive feedback loop including wall dilation, a further decrease in area ratio and thus an unstable progression of the disease. Finally, rupture occurs if the tissue fails to withstand the mechanical forces exerted by the blood at any location, irrespective of the global strength of the wall (Raghavan et al., 2011). Note that although the wall expands in this process, there is almost no change in total wall thickness (approximately 2 mm) since the media loses thickness, and the adventitia widens (Kemmerling and Peattie, 2018). An alternative mechanism for aneurysm formation is associated with disturbed flow conditions and unsteady turbulent stresses which develop inside the aneurysm sac. Over time, the geometry of the abdominal aortic artery progressively undergoes morphological changes like the formation of bends and kinks, which lead to successive disturbed flow conditions such as flow separation and weak turbulence inside the vessel. It is then argued that the abnormal response of the endothelial-regulated process to complex blood flow and wall shear stress distribution could contribute to an unstable gradual degradation of the arterial wall and, ultimately, to the formation of an aneurysm. This encourages AAA studies to incorporate WSS in their models to measure endothelial cell activation. However, such measures are likely biologically more relevant to the initiation phase of AAAs and irrelevant to disease progression since, according to Arzani (2016), it is likely enough that endothelial cells in AAAs are damaged and no longer able to sense and respond to the anomalies in the flow.

1.2.2 Natural history

In the majority of patients with an abdominal aortic aneurysm, the bulge undergoes a gradual expansion of 2.2 mm/year on average, which is reported to be the same in women and men. According to an individual patient meta-analysis of more than 15,000 patients with AAA diameter of 3-5.5 cm (Sweeting et al., 2012), aneurysms with larger diameters were found to expand at a higher rate of 3.6 mm/year for 5 cm aneurysms compared to 1.3 mm/year for 3 cm aneurysms. It was also observed that smoking results in a 16% (0.35 mm/year) increase in the growth rate. In contrast, the expansion rate has an adverse correlation (51% reduction) with diabetes, attributed to the usage of metformin to treat patients with type II diabetes.

Risk factors

Although it is still vague when discussing the underlying causes of aneurysm formation in the abdominal aorta, multiple risk factors contribute to the development and/or progression of the disease.

Smoking is known as the dominant risk factor. According to Chung (2018), 90% of all patients with AAAs have a history of tobacco use. It has been estimated that 75% of all AAA cases in the population are mainly attributable to smoking. Based on a study performed in the UK within a screening program for men above 50 years old with AAAs, the annual risk of AAA formation linearly increases by 4% for current smokers, which shows that the duration of smoking also increases the risk of AAA formation. Moreover, the meta-analysis of patient data by Sweeting et al. (2012) indicates that smoking cessation can lead to a nearly 20% reduction in growth rate, as well as a significant 50% decline in the potential risk of rupture. It is worth mentioning that smoking seems to have a more significant impact on the initiation phase of the disease.

As discussed earlier in Sec. 1.2.1, **age** and **gender** are also affecting AAA occurrence. Before the seventh decade of life, AAAs are rarely detected. Besides, while the incidence rate is remarkably higher in men, perioperative complications are more common in women, and the rupture may occur at smaller diameters as a result of less favourable female vascular anatomy (Lo et al., 2013).

Family history is another factor highlighted to increase the incidence of AAAs. Fifteen percent of patients with AAAs have a positive family history for the disease, and up to 20% of candidates for surgical intervention have a first-degree relative with an aortic disease (Wassef et al., 2007). Screening is recommended for all men and women over 50 years old with a first degree relative with an AAA. However, whether this has been beneficial has not formally been evaluated.

Hypertension is another frequently studied risk factor for the presence of AAAs with a 66% increased risk of developing the disease in hypertensive patients compared to non-hypertensive patients (Kobeissi et al., 2019). However, no significant association is found between hypertension and the expansion of an AAA (Takagi et al., 2017).

Atherosclerosis, the hardening and narrowing of arteries due to plaque deposition, has previously been considered to be actively involved in the process of aneurysmal degeneration. This idea was established based on clinical studies indicating the susceptibility of the infrarenal aorta to develop advanced atherosclerotic lesions due to the branching of the iliac and renal arteries (Chung, 2018). This traditional view has been challenged by the high number of patients diagnosed with an aneurysm without atherosclerosis. Currently, there is a relative consensus that atherosclerosis may aid the progression of AAAs but does not initiate the weakening of the wall (Lasheras, 2007).

1.2.3 Complications

Rupture

The most catastrophic complication of AAAs is rupture that is followed by massive internal bleeding and probably death. Immediate surgery to close and support the ruptured wall is the only method of repair. However, about 30-50% of the patients who survive before getting to the hospital die during the course of their hospitalization. Overall, the mortality rate on rupture is between 78 and 94% (Kemmerling and Peattie, 2018). Regardless of the rupture threshold, which will be brought into discussion in Sec. 1.2.5, an AAA ruptures when tension on the aortic wall surpasses the local strength, which more frequently takes place on the posterior wall of the aneurysm (Lasheras, 2007). The likelihood of rupture is correlated with several factors such as aneurysm size and morphology, expansion rate and gender (Aggarwal et al., 2011), although it is quite complex to predict and quantify the risk of rupture.

Intraluminal Thrombus

In nearly 75% of AAAs, the lumen is partially or fully covered by intraluminal thrombus (ILT) layers, a fibrin structure composed of platelets, blood proteins and red blood cells (Harter et al., 1982). The initiation of thrombus formation is the activation of platelets which may be triggered by both chemical and mechanical stimuli in the regions of high shear in the internal median layers, and then be transported to the slowly recirculating regions with blood stasis where they will build up on the wall of the aneurysm (Lasheras, 2007). Another factor that may be involved in the thrombus formation process is a compound in the blood plasma called the von Willebrand factor (Shankaran et al., 2003). It has been shown that the level of the von Willebrand factor is elevated during sleep, which is more likely occurs in men, possibly explaining the higher incidence of AAAs in men (Isselbacher, 2005).

Renal failure

Renal failure is a common postoperative morbidity associated with AAAs. Based on the analysis performed by Olsen et al. (1990), among 656 patients undergoing surgery for an abdominal aortic aneurysm, 81 patients (12%) developed renal failure.

1.2.4 Diagnosis

Symptoms

If present, symptoms of AAA are mainly localized pain or tenderness on palpation that can extend to the back or radiate to the genitals. However, clinical signs rarely show up through explicit bulging, and an AAA usually remains latent except when the expansion is occurring rapidly. This happens because pain receptors are located in the adventitia (outer layer of the arterial wall) so that as long as an intact structure is present, pain is not produced and felt (Erbel and Eggebrecht, 2006). Therefore, AAAs are often discovered incidentally during a clinical exam for other purposes or in the worst case when the aneurysm size has increased significantly, and the patient feels a growing pain in the abdomen spreading to the back with a sense of pulsation. Still, abdominal palpation

is not reliable for AAA diagnosis because its sensitivity to abdominal palpation is less than 50% and decreases with aneurysm growth (Karkos *et al.*, 2000). To decrease the risk of sudden rupture and mortality, population screening for abdominal aortic aneurysms is recommended for all men at age 65. Those with an aortic diameter of 2.5-2.9 cm at the initial screening should be revisited after 5-10 years. Although there is no such recommendation for women, all men and women aged 50 years or older with a first degree relative with an AAA should be considered for screening every 10 years (Wanhainen *et al.*, 2019).

Imaging techniques

In order to detect an AAA and assess its size, different imaging modalities are used by clinicians, including ultrasound (US), computed tomography (CT) scanning and magnetic resonance (MR) angiography. Among these, abdominal ultrasound and duplex ultrasonography (DUS) are more practically employed since they are noninvasive, versatile and provide high sensitivity (Baxter *et al.*, 2008).

Ultrasound is specifically used to monitor patients with small AAAs. The CT scan is the reference technique to decide to intervene, plan the treatment and diagnose the rupture, (Long *et al.*, 2012). Other imaging modalities including CT colonography and spinal imaging, may be utilized to diagnose an AAA. With each of these techniques, different diameters (i.e., anteroposterior, transverse, maximum in any direction) can be measured that should be specified with detail in the clinical report, specifying the plane and axis of measurement.

1.2.5 Management

When an abdominal aortic aneurysm is diagnosed, surgeons take several factors into account, including the risk of rupture, the patient's gender and life expectancy, smoking habits and operative risk to decide whether to intervene surgically or suggest regular surveillance. The right decision is of paramount importance given the high mortality rate of 50% among patients with a ruptured aneurysm that were left untreated. This number draws more attention when it is compared to a 1-5 % risk of mortality for undergoing an elective AAA repair (Schermerhorn, 2009).

Management of small aneurysms

For those patients who are not recommended repair, the alternatives are medical treatment and regular clinical evaluation through ultrasound to try to limit the rate of expansion and to reduce the cardiovascular risk for future AAA repairs. However, no class of inhibiting drug or therapy, including exercise, has been proven to be effective in reducing the rate of aneurysm growth. Therefore, the most common strategy is to do follow-up scans until the intervention threshold is reached. The frequency for surveillance of aneurysms 3-5.5 cm in diameter is determined based on the maximum diameter. For the incipient aneurysms (3-3.9 cm), the patients should be monitored every three years, while this is switched to annual surveillance for aneurysms 4-4.9 cm in diameter. When the diameter reaches 5.0 cm, the surveillance scans should be performed more frequently (every 3-6 months). Interestingly, in a trial study performed in the UK for medium-sized aneurysms (4 to 5.5 cm), regardless of age and gender, no overall difference in survival was reported between patients

who underwent immediate repair and those who were being monitored for up to 8 years (Filardo et al., 2015).

Threshold for elective repair

Primarily, the maximum anteroposterior diameter exceeding 5 cm in women and 5.5 cm in men is considered as the main indicator for treatment. At this stage, the risk of rupture presumably surpasses the potential risk of elective AAA repair. Clinically, it is well established that the risk of rupture increases with increased aneurysm size in terms of its maximum diameter. The annual risk of rupture for aneurysms smaller than 4 cm is almost 0% compared with 3–15% in aneurysms 5–5.9 cm. There is a dramatic increase in the risk of rupture (20–25% each year) for aneurysms larger than 7 cm (Brewster et al., 2003). Although larger aneurysms are likely to rupture more often, they can grow without bursting while some other asymptomatic smaller-sized AAAs might end up with serious difficulties instead. An autopsy investigation of 24,000 cases, including 473 non-resected AAAs, revealed that 60% of the AAA patients had died with a non-ruptured aneurysm larger than 5 cm, whereas only 13% of aneurysms with a diameter smaller than 5 cm ruptured (Darling et al., 1977). This example questions the adequacy and reliability of the maximum diameter criterion for severity assessment and rupture prediction. As mentioned earlier, the rupture follows the basic principles of material failure with a greater likelihood of occurrence for higher wall stress to strength ratio. Note that neither of these parameters can be determined merely from the diameter, which is a static measurement and does not consider dynamic interactions between physical forces and the biology of the aortic wall (Vorp, 2007). In order to make a proper prognosis, a fluid-structural analysis should be performed. However, flow-structure models have been far from being an ideal and a reliable tool to guide the clinical management of the disease because they do not provide precise information on the thickness, composition and structure of the wall at each location (Lasheras, 2007).

Another criterion taken into consideration to perform an elective repair is an expansion rate of 0.5 cm or more over six months or 1 cm over one year which is roughly estimated based on the change in maximal diameter (Hirsch et al., 2006).

Some other parameters that have been proposed to predict the risk of rupture include wall stiffness, increase in intraluminal thrombus (ILT) thickness, wall tension and peak wall stress. All these parameters depend on the aneurysm surface geometry and AAA wall mechanical behaviour, and are intertwined with shortcomings that could result in fatal errors in decision making.

Overall, although the maximum diameter is considered the determinant criterion for medical resection, a clearly defined protocol concerning the plane of acquisition, axis and temporal phase of measurement, caliper placement position and the selection of maximum diameter is missing which augments the variability and unreliability of the measurements. However, the common consensus is to take any action based on the measured anteroposterior aortic diameter in a plane perpendicular to the aortic longitudinal axis (Long et al., 2012).

Elective AAA repair

Regardless of whether relying on maximal diameter is safe enough to proceed with surgical repair, available options to treat infrarenal aortic aneurysms are open surgical repair (OSR), endovascular aneurysm repair (EVAR) and endovascular aneurysm sealing (EVAS). In the former, the surgeon makes a wide transverse incision to the abdomen and inserts a graft, a knitted synthetic textile

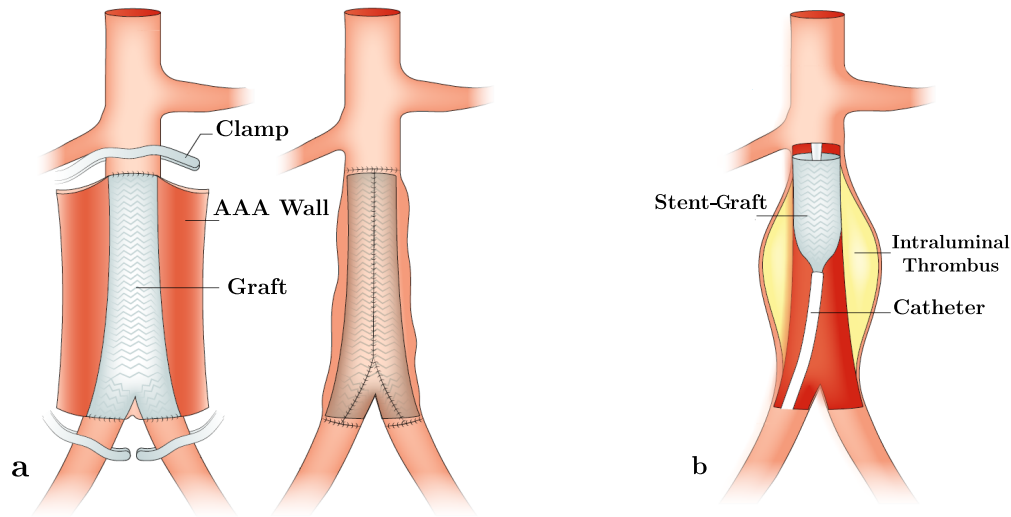


Figure 1.3: Elective repair methods for an abdominal aortic aneurysm: a) open surgical method (OSR); b) endovascular aneurysm repair (EVAR). Reproduced from [Sakalihan et al. \(2018\)](#).

sealed with collagen or albumin, into the aneurysmal area. In EVAR, which is minimally invasive, an expandable endovascular stent-graft is advanced into the aorta through the femoral arteries using guidewires to bridge the aneurysmal region. Therefore, the blood no longer exerts pressure on the walls of the aneurysm. Both options are sketched in [Fig. 1.3](#). Traditionally, the use of stent-grafts for endovascular repair of abdominal aortic aneurysms has generally been limited to older patients and those at high operative risk due to age, heart disease or other medical conditions ([Isselbacher, 2005](#)).

Currently, EVAR is the primary treatment method for the repair of infrarenal AAAs with lower rates of morbidity and mortality compared to OSR. Endovascular aneurysm repair is successful in about 78-94%. Nevertheless, 10 to 20% of patients face a major problem related to endoleaks occurring when blood enters the aneurysm sac due to failure of the implanted graft to exclude the aneurysm from the aortic circulation which in turn puts the patient at risk of further expansion or rupture. In a follow-up study carried out among 1000 stent-graft recipients within a year after the repair, almost 10% of patients each year required secondary interventions, suggesting that the decision to treat a patient with endovascular aneurysm repair should be made more cautiously.

To mitigate the risks of EVAR and to improve the clinical outcomes of AAA treatment, a novel approach, namely, endovascular aneurysm sealing or EVAS, has been proposed, with a better sealing to the aneurysm lumen. In this method, which is implemented using the Nellix system (Endologix, Irvine, CA), two balloon-expandable stents surrounded by polymer-filled endobags are introduced into the aorta in a similar way to EVAR. The catheter sheaths are then pulled back. The device is deployed and expands from the aortic neck to the common iliac arteries. The non-porous PTFE-based endobags will then be filled using a biocompatible polymer, which adjusts the endobag to fit the aneurysm sac and to create a sealing zone ([Brownrigg et al., 2015](#)). The procedure is depicted in [Fig. 1.4](#). Up to now, EVAS has opted for patients with challenging aortic morphology, which yields acceptable outcomes regarding endoleak prevention. However, its extensive use requires further investigation to certify if it is an advantageous alternative over the two conventional techniques described earlier.

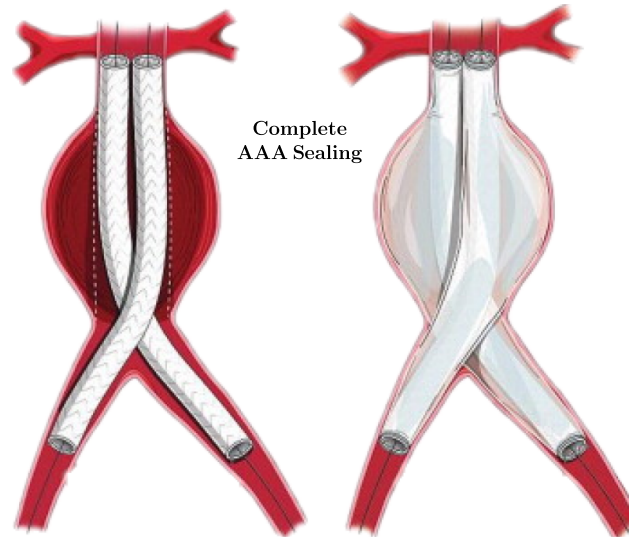


Figure 1.4: EVAS repair for an infrarenal abdominal aortic aneurysm which uses endobag insufflation to seal the aneurysm. Reproduced from [Brownrigg et al. \(2015\)](#).

1.3 THESIS OUTLINE

The current thesis is structured as follows. Throughout [Ch. 2](#), a summary of the literature survey is provided to familiarize the reader with the background of the research on flow dynamics in AAAs. Chapter [3](#) is devoted to a comprehensive description of the methodology related to the experimental and analytical phases. Subsequently, in [Ch. 4](#), the results of the experimental investigation of the flow within the aneurysms of various shapes are presented and discussed in detail. Finally, the essential findings and some recommendations for future work are summarized in [Ch. 5](#).

2 | RELEVANT WORKS

This chapter sheds light on the background of blood flow characterization within an abdominal aortic aneurysm. The objective is to look at AAAs from a fluid dynamic perspective to familiarize the reader with the noteworthy findings on the flow behaviour through the balloon-like bulge focusing on the velocity field, viscous energy loss and proper orthogonal decomposition. This will effectively help to validate and interpret the results included in the following chapter.

2.1 AAA FLOW CHARACTERIZATION

In the context of characterization of flow dynamics through AAAs, various *in vivo* and *in vitro* techniques have been used to measure the flow both qualitatively and quantitatively.

2.1.1 Summary of *in vivo* studies

To gain insight into the blood flow behaviour *in vivo*, data on the velocity field in the region of interest is required. However, most clinical studies with AAA patients have only addressed the waveforms (e.g., instantaneous velocity profiles, time varying pressure and flow rate profiles) at different locations and were less interested in flow visualization.

The conventional method for non-invasive assessment of the flow in the abdominal aorta with or without an aneurysm is Doppler ultrasound velocimetry (DUV), providing only limited volumetric flow information. In principle, using an ultrasound transducer, 1D flow velocity (a single peak and/or the average waveform) at a given cross-section can be obtained by detecting the Doppler shift in sound waves scattered from the moving blood components (e.g., red/white blood cells). In the work of Fraser et al. (2008), as one of the first attempts to compile AAA inlet flow data using ultrasound, centreline velocity waveforms at the infrarenal level were measured in 31 patients. In turn, the volumetric flow was determined by assuming a Womersely profile and using a mean aortic diameter measured from eight cases. The resulting waveform was triphasic with a maximum velocity of 45 ± 13 cm/s. However, this representation is not ideal since the actual infrarenal (IR) flow waveform is not periodic and axisymmetric.

Additionally, DUV does not provide any information regarding the flow structures within the aneurysm sac. It also has low resolution and high uncertainty and is challenging to use where bowel gas or imaging depth may lead to loss of signal. This problem, though, can be compensated by using US contrast agents. For flow visualization, colour Doppler ultrasound (CDU) can be utilized to detect the aneurysm as the region with a decelerated swirling flow.

A better choice for an *in vivo* exploration of flow in the abdominal aortic aneurysm is to use MR imaging techniques. Two-dimensional phase-contrast magnetic resonance imaging (PC-MRI), for example, has been extensively used for volumetric flow data acquisition by means of measuring

planar velocities and integration over the vessel lumen. The resulting waveforms can ideally be used as the inlet boundary condition for *in vitro* and *in silico* hemodynamic simulations.

Les et al. (2010b) measured and presented volumetric flow at the suprarenal (SC) and infrarenal (IR) aorta from 43 patients. The flow waveforms at both locations were found to be biphasic in shape for older patients. However, the temporal resolution of 23.8–25.4 ms was not adequate to faithfully resolve the flow. Infrarenal flow is characterized by a notable reversal portion at end-systole and remains fairly close to zero during diastole. At the SC level, the flow approaches zero at end-systole and remains positive and almost constant during diastole. The reverse IR flow serves as evidence for the hypothesized role of the abdominal aorta as a capacitor with the reverse flow likely being delivered upstream to supply the renal flow demand during diastole.

In more recent years, the advent of 4D flow MRI (a 3-dimensional, 3-directional and time-resolved PC-MRI) has enabled direct, non-invasive cardiovascular hemodynamic measurements. In the context of the abdominal aortic flow, Wang et al. (2016) captured the flow data in an axisymmetric aneurysm model using 4D flow MRI sequences and qualitatively compared the results with those of PIV measurements, which showed good agreement regarding the central jet and vortex evolution. In another *in vitro* application of 4D flow MRI, Ziegler et al. (2019) visualized and quantified regions of stasis inside AAAs, where pathlines that displayed consistently low velocities were considered to be in stasis.

In a nutshell, MR techniques require no optical access and yield more accurate results with a higher resolution than DUV. However, the process is slower and far more expensive than DUV. Similar to ultrasound, MRI scan protocols for AAA surveillance rarely include acquisition of PC-MRI flow data, due to the general lack of clinical application for flow data.

Echocardiographic particle image velocimetry (echo-PIV) is another technique initially finding use in the carotid artery to obtain two-dimensional velocity vector fields in the axial and lateral directions (Zhang et al., 2011). With this technique, PIV analysis is performed using images acquired through US. However, as mentioned earlier, the application of US in the abdominal aorta has shortcomings such as low resolution and loss of signal. Recent developments in the use of high frame rate contrast material enhanced US (HFR CEUS) have made it possible to quantify blood flow with echo-PIV. Nevertheless, flow velocities of approximately 1 m/s, which can be found in the human abdominal aorta, have not been successfully quantified until recently. Engelhard et al. (2018) performed the first human study using echo-PIV to quantify blood flow in healthy human abdominal aortas and compared the acquired velocity profiles with those from MRI showing a good agreement between both techniques (similarity index of 0.98).

2.1.2 Summary of *in vitro* studies

In vitro investigations of the flow characteristics within AAA phantoms and the normal abdominal aorta have been carried out through various methodologies. In general, the design process of an *in vitro* study involves 4 selection steps; the target parameter, the imaging technique, the model and the flow condition.

The target parameter, mainly flow or velocity, is determined by the study's objective. At the very beginning, studies were limited to a qualitative visualization of flow. In an early attempt to visualize the flow inside the abdominal aorta, Moore Jr et al. (1992) used dye injection inside a glass model (the working fluid being water) and recorded image and video sequences of the motions of the dye streaks under steady and pulsatile flow conditions. They found that contrary to the

suprarenal aorta where the flow exhibited a laminar pattern, flow in the infrarenal segment was more complex, being characterized by transient separation due to the curved morphology, regions of vortex formation below the renal arteries, and a horseshoe vortex which was created because of the presence of the aortic bifurcation downstream of the abdominal aorta.

Afterward, colour Doppler flow imaging was applied for direct observation of the flow fields in the aneurysm models through image acquisition with an ultrasonic imaging system whereby researchers could gain an overall perception of the flow and an initial estimation about the onset of turbulence within AAA phantoms (Asbury et al., 1995).

Later, with the development of 4D flow MRI, flow visualization has evolved toward 3D streamlines or time-resolved 3D pathlines. This is implemented by Wang et al. (2018b) in a study, where the velocity field in an anatomically realistic silicone phantom of an AAA is determined from 4D flow and MRI measurements. The flow data is then prescribed into a CFD model to calculate wall deformations. The use of MRI is advantageous since flow information can be retrieved with no need for a scatter material (e.g., particles or contrast agents) and the possibility of conversion to a patient study. Despite its merits, MRI is rarely preferred because it can often only be found in a clinical centre.

Given the shortcomings of MR velocimetry, including long acquisition times and insufficient resolution, several *in vitro* studies employed laser-based techniques such as laser Doppler velocimetry (LDV) to obtain velocity field information inside an AAA. LDV works based on the Doppler effect, two laser beams measure 3D velocity at individual points with a notably high temporal resolution. In a systematic investigation of bulge diameter's effect on the flow patterns and flow-induced wall stress magnitudes, Peattie et al. (2004) used LDV to assess velocity field evolution in fusiform, rigid AAA models under pulsatile flow conditions. They found that a bigger bulge diameter is accompanied by increased flow instabilities prolonged to a larger portion of the cardiac cycle. However, the data collection was limited to 50 points, implying a low spatial resolution. Laser Doppler velocimetry was also utilized by Yip and Yu (2002) to study the evolution of vortical structures in a straight tube with an axisymmetric bulge of two different sizes filled with a Newtonian viscous fluid. Instantaneous velocity profiles demonstrated gradual growth of instability during the acceleration phase with a transition to turbulence shortly after the beginning of the deceleration phase regardless of its location, which would flatten velocity profiles with a more prominent bulge. A few more applications of LDV in the case of AAA flow can be found in Peattie et al. (1996) and Egelhoff et al. (1999).

As mentioned before, being a single point measurement technique makes LDV unfavourable to fully resolve the velocity field. Particle image velocimetry is the alternative that has been frequently utilized in *in vitro* AAA related studies that can be categorized primarily based on the experimental flow condition and the phantom properties. Variations concerning the flow are attributed to the choice of flow waveform, working fluid and heart rate. Regarding the AAA model, geometry and wall elasticity are principle considerations. Although not realistic, in early studies (Bluestein et al., 1996), experiments were carried out only under the steady flow condition featured by a large potential core across the undilated portion upstream of the bulge. Based on their observation, inside the bulge, the adverse pressure gradient imposed by the sudden expansion creates recirculating vortices that surround the jet passing through the core.

Later in 2000, Yu conducted the first PIV measurements for both steady and pulsatile flow in a fusiform aneurysm with an imposed sinusoidal waveform. Under the pulsatile condition, the recirculation extent and the vortex core location were observed to vary at different instants of the cycle. For the steady flow, the location of the vortex core remained relatively constant.

Beside the pulsatile nature of the flow, the other parameter that can make the simulation unrealistic, if overlooked, is the wall deformation. In many studies, the aneurysm models were rigid and mainly made out of glass (Yu, 2000; Antón et al., 2015). The use of rigid models is justified in Salsac (2006) by referring to the lower compliance of the aortic segment with an aneurysm compared to the normal aorta. However, this is not adequate to disregard the compliance since it plays a chief role in generating the physiological pressure waveform, which contradicts what is claimed in Salsac regarding the irrelevance of the vessel compliance and the pressure. The effect of wall compliance was first included in an *in vitro* experimental design by Deplano et al. (2007) who compared the flow behaviour in two identical models; a solid glass model and a soft polyurethane model. The results were significantly different in terms of vortex dynamics within the AAA. Contrary to the rigid model whereby the vortex emerged during early deceleration with little convection, the vortical structures in the compliant model traveled downstream and impacted the wall at the distal end. This resulted in local pressure increase and further wall attenuation. The authors attribute the distinction in the secondary flow patterns to the expansion and retraction of the compliant wall resulting from the absorption and restitution of energy during the cardiac cycle. Again this suggests a discrepancy in the results obtained by Salsac who proposed that compliance has no effect on the general flow characteristics in an AAA.

Considering the phantom design, there are a few experimental investigations undertaken in patient-specific or anatomically accurate AAA models, the results of which have corresponded well with those from the analysis made using simple averaged geometries (Stamatopoulos et al., 2011). Effectively, most of the studies (Peattie et al., 2004; Salsac, 2006; Deplano et al., 2007), picked a branchless straight tube with a middle bulge to mimic the aneurysm, and neither the iliac bifurcation nor the aortic side branches are taken into account. The former reflects the pressure pulse wave travelling along the aorta, which partially amplifies the total pressure in the AAAs. In the case that the bifurcation is present, Deplano et al. (2014) observed a different trajectory for the vortex ring with a lower impact intensity compared to the model without the bifurcation.

The AAA replica is often designed and fabricated with aortic side branches excluded. However, the inclusion of the renal arteries in the design can make the simulation more realistic, especially in the proximal neck upstream of the aneurysm since they affect the local disturbances and the inflow jet's orientation (Arzani, 2016). Besides, according to Les et al. (2010a), there is a diastolic retrograde portion in the flow waveform at the infrarenal level, which is likely to occur in response to the continuous forward flow of the renal branch during diastole, which again advocates for the consideration of these arteries in the design. Referring to Kung et al. (2011) as the only experimental study (using PC-MRI) that includes 4 branches at the outlet, such a limitation is negligible when the flow is being mimicked in a small branch. However, the renal arteries are important branches of the abdominal aorta (they display unique waveforms), therefore neglecting them severely hinders a realistic simulation. The phantom in Van Noort et al. (2018) was also made with the renal arteries, although flow investigation was not done with PIV, and aimed at investigating the influence of different aortic endoprostheses on pulse-wave-velocity (PWV) and structural stiffness.

Fluid dynamic studies on AAAs with PIV have been mostly confined to 2D acquisitions, and 3D versions of PIV (e.g., tomographic PIV and holographic PIV) have not yet been implemented to delve into the flow characteristics in the abdominal aorta. Nonetheless, efforts have been made to look at the case from a 3D perspective. Stamatopoulos et al. (2011) applied the conventional planar PIV to measure phase-averaged velocity (14 instants) of the flow in the dilated region in 14 consecutive planes; 8 planes parallel to the sagittal plane and 6 parallel to the coronal plane.

They used interpolation to find the instantaneous velocity vectors in the planes of measurement and also the transverse velocity component at eight cross-sections within the bulge. Note that the non-dimensional parameters (i.e., Reynolds and Womersley numbers) were not reproduced faithfully due to the limitations of their experimental apparatus. Other than that, the aneurysm model was rigid, the drawbacks of which were already discussed.

Measuring the out-of-plane velocity component is also feasible through the stereoscopic PIV technique and was conducted by [Deplano et al. \(2016\)](#) to assess the evolution of vortical structures in a 3D framework, but the flow was not time-resolved.

2.1.3 Summary of *in silico* studies

Computational fluid dynamics (CFD) has also been widely used in AAA flow evaluation. The simulations are differentiated depending on the adopted numerical scheme and the input parameters such as the geometric properties of the aneurysm, boundary conditions, blood rheology and turbulence model.

Early studies were mainly grounded on idealized geometries and focused on exploring the general features of the flow inside the aneurysm with more interests towards the calculation of hemodynamic parameters such as wall shear stress (WSS), oscillatory shear index (OSI) and intraluminal pressure ([Taylor and Yamaguchi, 1994](#); [Finol and Amon, 2001](#)). Later, simulations were performed on patient-specific or image-based geometries in which arterial wall interaction with the blood flow was also considered through coupling solid mechanics with CFD ([Leung et al., 2006](#)). Particle residence time, global stability, the effect of exercise and turbulence are other areas of interest in computational studies of AAAs ([Arzani, 2016](#); [Gopalakrishnan et al., 2014](#); [Rawat et al., 2019](#)).

Currently, the focus in CFD studies of AAAs is to simulate the remodeling and investigate the hemodynamic mechanisms underlying AAA expansion to provide tools that can predict the aneurysm growth and risk of rupture ([Joly et al., 2020](#)).

2.2 AAA FLOW PATTERNS

The nature of blood flow through the arterial system, particularly in areas with complex geometry, is well known to play a role in altering the constituents, geometry and mechanical strength of the arterial wall. Analysis of flow patterns within aneurysms can lead to a better understanding of the mechanical forces associated with further dilation of the wall and its eventual rupture. In order to better interpret and correlate the changes in the flow behaviour with the development and progression of the aneurysm, a *priori* knowledge on the flow pattern in the normal abdominal aorta is required.

2.2.1 Flow features in the normal abdominal aorta

Pulsatile blood flow in a healthy abdominal aorta with a mean Re of about 600 is expected to be laminar with similar velocity profiles repeating every pulse ([Ku, 1997](#)). This holds for the suprarenal segment where the flow is relatively undisturbed with a laminar pattern throughout the cardiac cycle ([Moore Jr et al., 1992](#)). However, for the infrarenal aorta, the flow is attached and unidirectional

only during systole. When the flow starts to decelerate, it exhibits a different behaviour induced by the upstream and distal outflow vessel branches.

In brief, four main characteristics of the infrarenal flow were highlighted by Moore Jr et al. in an experimental visualization of the flow in a glass model of the abdominal aorta: 1) formation of time-varying vortex patterns below the renal arteries due to flow separation from the upstream branches at the level of the diaphragm; 2) skewed velocity profiles toward the anterior wall due to the presence of lumbar curvature meaning that the flow at the posterior wall has less momentum; 3) a region of transient flow reversal in late systole with a prolonged residence time along the postero-lateral wall; and 4) formation of a horseshoe vortex at the terminal aorta due to the aortic bifurcation. The results comply with *in vivo* flow measurements led by the same group and supported by the computational study of blood flow in an idealized abdominal aortic geometry carried out by Taylor et al. (1998). It was also deduced in Pedersen et al. (1992) that the flow in the abdominal aorta is quite complicated and different from the forward-moving flow in a straight tube. In fact, from a hemodynamic standpoint, flow in the abdominal aorta can be viewed as a superposition of unsteady flow in a straight tube, flow through a curved tube, flow through a vessel with branching and flow in a symmetric bifurcation. Rawat et al. modelled the flow in the normal aorta to be used as the baseline in their study on the mechanism of transition to turbulence in AAAs. Given that none of the branches were included, they observed the same flow field in successive cycles with no turbulence, which they suggested to be the inadequacy of the temporal deceleration occurring right after peak systole to trigger turbulence in an intact abdominal aorta.

2.2.2 Flow features in the abdominal aortic aneurysm

Extensive analysis of the fluid dynamics inside AAAs has been undertaken through the several available modalities and has been represented predominantly by velocity, vorticity, wall shear stress and turbulence intensity, with a significant variation indicating that the aneurysmal flow is notably patient-specific and associated with the upstream flow patterns (Arzani, 2016). Nevertheless, speaking of the abdominal aortic aneurysm, some features are invariant and entailed in AAA flow models. The general characteristics of the flow field in AAAs are discussed in Kemmerling and Peattie (2018) and will be briefly summarized here.

Separation is the first feature which occurs when the near-wall streamline deviates away and creates a recirculation region which is poorly mixed with the central jet. According to Arzani (2016), however, there is also evidence that mixing between the separated region and the higher speed jet is not negligible in many AAAs. It is worth noting that in some geometries, turbulence promotes mixing and prevents the formation of a recirculating zone, while it is ineffective in some other geometries.

Second, AAAs are often accompanied by a transitional flow regime and resulting instabilities, while small perturbations can consequently alter the flow patterns. Temporal deceleration due to the pulsatile nature of the flow and spatial deceleration due to bulge shape are known to be responsible for this behaviour (Gopalakrishnan et al., 2014; Peattie et al., 2004). Temporal deceleration refers to the systolic deceleration, whereas spatial deceleration should be explained by considering the expansion region with an increased diameter, where the blood flow is subjected to an adverse pressure gradient. Such a flow deceleration destabilizes the flow field and promotes transition to turbulence at a Reynolds number far less than the pipe flow threshold. Also, the long time scale of

instabilities indicates that they do not disappear quickly which makes the flow nonperiodic (Poelma et al., 2015).

The third common trait of the AAA flow field is vortex formation after peak systole. Vortices have been observed to form at either the proximal or distal ends of the aneurysm. Once formed, they convect downstream due to their self-induced momentum and the velocity of the bulk flow. The vortex formation is the same from cycle to cycle. It occurs due to the velocity discontinuity on the jet's boundaries, which generates a separated near-wall shear layer that rolls up into a vortex. The number of vortices, their size, exact trajectories and eventual breakdown are highly patient-specific (Arzani, 2016).

2.3 AAA ENERGY LOSS

Energy loss is a normal phenomenon in blood flow. In principle, due to the viscous friction caused by the velocity gradients, blood flow kinetic energy can be irreversibly converted into heat, which means a lower efficiency for the circulatory system. Nonetheless, this physiological energy loss can be aggravated with the occurrence of pathologies, such as valvular stenosis, regurgitation and aneurysm. Quantification of the excess loss is likely to be pragmatic in risk stratification and severity assessment (Binter et al., 2016).

Several studies have been conducted to investigate the energy loss characteristics of cardiovascular flows. In the left ventricle (LV), for instance, energy loss is suggested to be a useful indicator of the severity of aortic regurgitation (AR). By nature, the well-structured vortical motion of the intraventricular flow in a healthy state results in minimal energy dissipation. This optimality can get compromised with the onset of a defect in LV function. In this case, to maintain a regular circulation of blood flow, the heart is obliged to work harder to compensate for the additional dissipated energy at the expense of increased stress on the myocardium due to the elevated LV systolic pressure and/or its volumetric capacity (Pedrizzetti and Domenichini, 2005; Akins et al., 2008). In earlier clinical attempts, pressure drop and flow rate were used to evaluate energy loss (Garcia et al., 2000). Later, fluid dynamic analysis of energy loss has evolved with the aid of the flow field's velocity information. The correlation of energy loss with the severity of AR is investigated in Stugaard et al. (2015) by using vector flow mapping (VFM) in dysfunctional LVs of dogs and human patients with different grades of AR, which revealed higher dissipation values in more severe cases. In an *in vitro* study, Di Labbio and Kadem (2018) also used 2D velocity data obtained from time-resolved PIV to quantify energy loss within the left ventricle affected by different severities of AR. Their analysis indicates that an increase in viscous energy dissipation follows atypical LV flow patterns distinguished by diastolic vortex reversal.

Elevated energy loss is also observed in cases with artificial valve implantation due to the altered vorticity. In a numeric simulation, Pedrizzetti et al. (2010) demonstrated that even a slight misalignment of the mitral prosthesis could lead to an increase in energy dissipation of up to 15%, which is considered as a post-procedural complication and potentially a precursor for the development of new pathologies.

Viscous energy loss evaluation has also been incorporated in studies on the abnormal flow through the aorta. In Barker et al. (2014), for instance, velocity data acquired from *in vivo* 4D flow MRI of cases with aortic dilation and/or stenosis was used to noninvasively quantify viscous energy

dissipation in the ascending and thoracic aorta. The results indicate that energy loss is augmented in both groups of patients compared to the normal subjects. Notably, in patients with an obstructed aortic valve, there was a strong correlation ($P < 0.001$) between energy loss and transvalvular pressure gradient as an established metric for the disease severity, which again upholds the idea of using energy loss as a clinical tool to assess the risks associated with the altered aortic hemodynamics due to the stenosis. However, the reliability of the viscous energy loss is controversial if the spatial resolution of the data is not adequate, as observed in PC-MRI based acquisitions (Binter et al., 2016).

Energy loss quantification has not gained much attention in aneurysmal flow analysis, neither in general nor specifically in the abdominal aortic aneurysm. Khe et al. (2015), in a numerical study of 5 cases with multiple intracranial aneurysms, showed that in three out of five cases, the viscous dissipation was lower in a ruptured aneurysm and proposed that in decision making for patients with multiple aneurysms, lower dissipation might be considered as a potential rupture indicator.

In an AAA-related computational study (Van Noort et al., 2018), calculation of energy loss in patient-specific endovascular graft models showed the dominance of energy loss in the systolic phase. Regarding the spatial distribution, higher values of energy loss were found in the vicinity of the vessel wall after peak systole, while the maximum values at the end of diastole were focused in the central zone.

2.4 MODAL ANALYSIS

In-depth analysis and translation of large quantities of data on various fluid flow phenomena examined through experimental measurements or numerical simulations can be facilitated with modal analysis techniques. Modal decomposition is the most common method that enables researchers to represent a dataset (e.g., velocity fields) as a linear combination of principle low-rank components referred to as modes. Depending on the different criteria used to compute the modes, the decomposition either leads to the extraction of energetically and/or dynamically important structures. In the former, the spatial modes are ranked based on the energy content, while in the latter, growth rates and frequencies are highlighted through capturing dynamic modes. (Mendez et al., 2018).

Proper orthogonal decomposition is a prominent data-driven method that decomposes the data, regardless of the system's governing dynamics, into an optimal set of orthogonal basis functions or spatial modes with their associated temporal coefficients and energy levels. The rank or dimensionality of the flow field information determines the number of modes. In essence, the algorithm of POD looks for the best low-dimensional representation of the field variable. The optimality stems from the fact that POD minimizes the mean-square discrepancy between the actual signal and its truncated approximation for a given number of modes (i.e., least \mathcal{L}_2 norm). In other words, POD can provide the best approximation in the sense of extracting as much kinetic energy as possible, for example, if the velocity information is being analyzed. Note that, based on their contribution to retaining the measured system's energy, the resulting modes are ranked in descending order. Also, for a known target error level, the number of POD modes that are required to extract the essential features of the flow field would be minimal (Taira et al., 2017). In the framework of fluid mechanics, POD has been originally applied to a random vector field to disclose the elusive flow features via spatial distribution of a chosen subset of modes (Lumley, 1967).

Currently, according to the research goal and interests, different variations of POD can be utilized for predictive modelling, pattern recognition or classification, data compression/ reconstruction, noise-filtering, experimental validation of computational fluid dynamics data, flow sensing and control, and data-driven identification of nonlinear systems (Mendez et al., 2018). For further details on POD theory and application, the reader is referred to Berkooz et al. (1993).

In cardiovascular flow analysis, although infrequent, POD has been applied to describe the flow structures using the information extracted from the optimal set of modes representing the initial large dataset (Grinberg et al., 2009; Kefayati and Poepping, 2013). Proper orthogonal decomposition is also useful in cutting out the noise from experimental data in the left ventricle (Charonko et al., 2013). Additionally, predictive models have been created by applying POD onto an existing dataset of the flow in the pulmonary artery, carotid artery bifurcation, and coronary bypass grafts to estimate clinically-relevant flow parameters in new patient-specific geometries (Guibert et al., 2014; Manzoni et al., 2012; Di Labbio and Kadem, 2019; Ballarin et al., 2016). Di Labbio and Kadem (2019) made use of POD to construct a reduced-order model of PIV data to represent the flow in the left ventricle in the presence of aortic valve regurgitation.

In the case of flow in the abdominal aortic aneurysm, POD applications have not drawn much attention. However, McGregor et al. proposed an original idea for taking advantage of POD to enhance the spatial resolution of an otherwise poorly resolved flow field obtained from PC-MRI. Their methodology was to use numerical data of flow simulation in AAAs of different geometries to create a standard model with a fine grid whereon the PC-MRI data could be mapped and interpolated and mapped back to the original geometry. POD has also been applied in the computational study of Chang et al. (2017) to construct two reduced-order models of the flow behaviour and estimate the flow-induced WSS of a simplified AAA with various inflow angles.

2.5 AAA RUPTURE ASSESSMENT

As already mentioned, the clinical evaluation of AAA rupture potential is based on the maximum transverse diameter from computed tomography (CT) images and a rough estimation of the expansion rate. From a solid mechanical outlook, the law of Laplace can rationalize the diameter criterion, relying on a linear correlation between the lumen diameter and the wall stress in cylindrical geometries. However, it cannot provide a genuine prediction of the actual loading for more complex geometries. It also fails to consider the patient-specific state of the arterial wall, which affects AAA formation and dilation (Vorp, 2007). Additionally, the aortic diameter is a static measure that neglects the dynamic interactions between local hemodynamic forces and the aortic wall's biology. Therefore, the fact that rupture occurs at a wide range of sizes (i.e., approximately 10–15% of the ruptured cases are below the threshold of 5–5.5 cm) confirms that additional criteria are required to assess a particular AAA's susceptibility to rupture. Studies have suggested that accurate quantification of shape, size, local wall thickness, flow patterns and dynamics, hemodynamic pressure, wall stress and structural properties can provide valuable information for predicting individual rupture risks in AAA management, establishing index thresholds for decision making and customized designs of endovascular grafts (Shum et al., 2011).

2.6 THESIS OBJECTIVES

As discussed earlier, the interplay between the hemodynamic forces and the aortic wall is deterministic in an AAA's initiation and progression. Nevertheless, in the context of a fluid dynamic analysis, despite extensive *in silico* research on blood flow characterization in AAAs (Les et al., 2010a; Arzani, 2016; Lozowy, 2017), the interaction between the luminal flow and the aortic wall is rarely taken into account. The existing FSI studies lack experimental validation using either *in vivo* or *in vitro* modalities. On the other hand, considering the few experimental studies on the fluid dynamics in AAAs, although the wall's displacement is modelled using a compliant material (Deplano et al., 2016), there are still shortcomings related to the design and implementation. For instance, the effect of upstream disturbances due to the presence of visceral branches and aortic curvature, and also the effect of the aortic bifurcation, are often ignored, which might undermine realistic modelling of the flow within the aneurysm sac. Furthermore, there is a substantial gap regarding the instantaneous flow field information that, if available, can provide a better insight into the complex flow characteristics in AAAs. Moreover, another original topic in experimental studies of AAA flow is the application of modal decomposition techniques such as proper orthogonal decomposition (POD), which can be employed for identification of the dominant structures, reduced-order modelling and classification of the clinical data.

Therefore, to elucidate our understanding of the flow inside the abdominal aortic aneurysms, the current work is proposed To answer the following questions:

- Can a customized experimental setup reproduce the complexity of the flow in AAA models as found *in vivo*?
- Do the size and the geometry of an AAA significantly impact the flow characteristics in terms of vortical structures and energy loss?
- Can modal decomposition using proper orthogonal decomposition allow for the identification of the dominant flow structures in AAAs and provide a robust reduced-order model?

3

METHODOLOGY

The abdominal aortic aneurysm has received considerable attention in *in vivo* studies to investigate the hemodynamic, structural and morphological characteristics of an AAA. Nevertheless, associated shortcomings such as complex geometry, burdensome clinical trial protocols, unrepeatability of *in vivo* experiments, low-resolution data, and the high expenses of performing multiple measurements with available modalities pushed researchers to complement the analyses through *in silico* and *in vitro* techniques.

Using computational methods to investigate the fluid dynamics and mechanical behaviour of the arterial wall has the privilege of ending up with a fully time-resolved 3D flow inside AAAs with patient-specific geometries if needed. It is also possible to consider material transport with the aid of multiphysics blood flow simulations. Moreover, to evaluate and predict the expansion rate, CFD can be a better choice since, for an *in vivo* study, it is essential and quite challenging to recall patients and repeat the measurements periodically. However, the boundary condition of the computational methods, which should be derived from *in vivo* measurements, lacks accuracy due to the complex mechanical environment of AAAs. Also, it is computationally expensive to incorporate the wall motion and its interaction with the luminal fluid. Hence, it is inevitable to simplify the model using a rigid arterial wall assumption and to prescribe an approximate velocity profile to the inflow, among others.

Using experimental setups to simulate the AAA flow *in vitro* is an alternative that addresses some of the issues with the methods mentioned above. First, the flow and the pressure waveform can match the physiological conditions using an adjustable actuator. Also, the rigid wall assumption is no longer required with the availability of compliant materials that can reproduce with quite a high fidelity the fluid-structure interactions. Furthermore, the obstacles of turbulence modelling in computational methods are not a matter of concern *in vitro*. In terms of the resolution of the velocity, *in vitro* studies end up with a lower spatiotemporal resolution than *in silico* studies. Needless to say that the results using both methods have to be validated against clinical data when available.

For the current thesis, which aims to provide insight regarding the flow dynamics in AAAs with different maximal diameters in a systematic way, an idealized geometry is assumed for the AAA. The experimental apparatus, working condition and the implemented laser-based imaging technique, particle image velocimetry (PIV), will be discussed in further detail in this chapter.

3.1 EXPERIMENTAL APPARATUS

3.1.1 Flow circulatory system

The circulatory system is modelled with components that emulate the physiological waveforms, geometry of the aorta and biomechanical properties of blood so that the flow in the abdominal

aortic aneurysm can be explored under circumstances that are closest to *in vivo* conditions. A corresponding photograph and schematic illustration of the test rig are provided in Fig. 3.1 and Fig. 3.2, respectively.

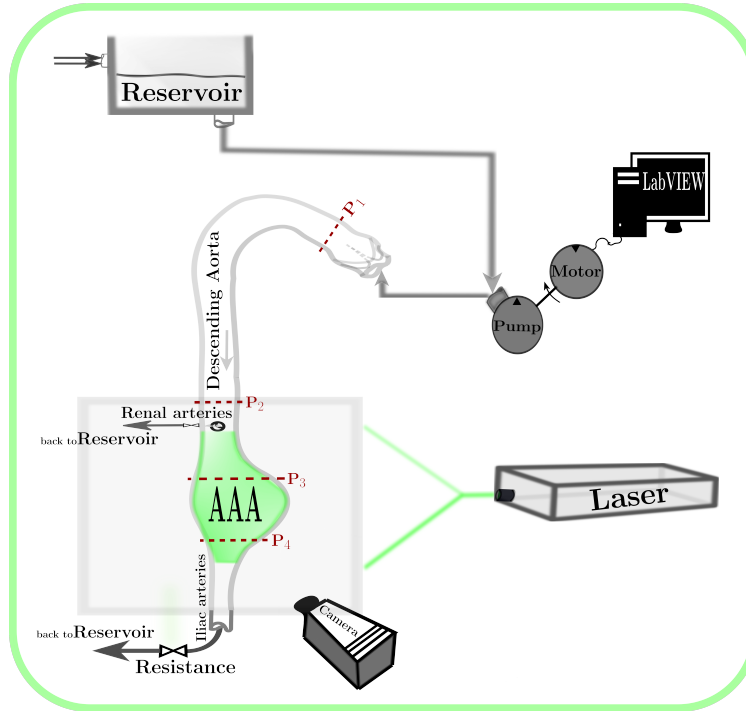


Figure 3.1: Schematic representation of the simulator.

The pulsatile flow circulation is generated and maintained using a positive displacement gear pump coupled with a motor. The choice of using this mechanism is favoured because the system was capable of working continuously for successive experiments and long-lasting hours. In order to run the pump, an input signal is sent to the system via a LabVIEW (National Instruments; Austin, TX, US) interface and a multifunction input/output device. The waveform is comprised of three segments; a half sine wave to simulate systole and regulate the flow rate similar to that in the abdominal aorta, a constant negative part to push the aortic valve leaflets backwards to close at the end of systole, and a final zero portion to complete diastole until the ejection starts over. The period of the sine wave and the frequency is adjusted to keep the heart rate at 63 bpm for all the experiments, which is selected to follow the clinically measured heart rate (62.9 ± 10.5 bpm) in Les et al. for AAA patients at rest. Womersely number (Wo) and Reynolds number (Re) are two dimensionless parameters that are generally used in blood flow studies. The Womersely number characterizes the unsteady nature of blood flow and is expressed as the ratio of the vessel diameter to the thickness of the unsteady boundary layer $Wo = \frac{D}{2} \sqrt{\frac{2\pi}{T\nu}}$, where D is the internal diameter of the cylindrical vessel and ν is the kinematic viscosity of blood. Here, for the time period of $T=0.953$ sec, the value of Wo is equal to 13.2. The corresponding expression for Reynolds number is $Re = \frac{VD}{\nu}$ where V is the normal velocity at the cross-section of interest. The computed average value for $Re_m = \frac{V_m D}{\nu}$ for all the cases is 344 ± 7 .

More details on the waveform properties are covered in Sec. 3.1.2. The pump is fed by an open reservoir, which is placed at a higher elevation than the test section to ensure the required pressure

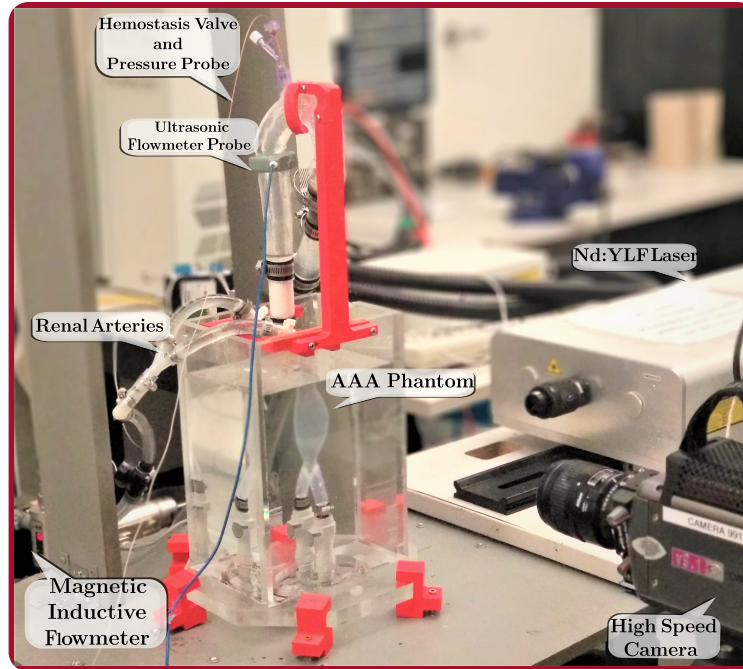


Figure 3.2: Components and configuration of the experimental setup.

head throughout the operation of the system. The reservoir is filled with a mixture of distilled water and glycerol (40% v/v) seeded with particles for visualization purposes; see [Sec. 3.1.4](#) and [Sec. 3.2.2](#). The blood analogue flows through a rigid tubing and gradually loses instabilities introduced at the pump exit. Hence, at a fully developed state, the flow reaches the aortic root where a trileaflet bioprosthetic aortic valve is mounted. The valve is a 25 mm Perimount Theon RSR valve (Edwards Lifescience; Irvine, CA, US), which is adopted to impose the cardiac cycle's pulsatile behaviour to the circuit. The flow continues its journey within the aortic arch, the descending aorta, and branches off to the renal arteries and the abdominal aorta. Inclusion of the right and left renal arteries along the longitudinal axis of the phantoms led us towards a more realistic flow pattern, specifically at the proximal neck of the infrarenal aorta. Indeed, these side branches induce a disturbance that affects the orientation of the inflow jet and in turn, impacts the pathway of the vortex formed after the peak systole in the proximal aneurysm ([Arzani, 2016](#)). The infrarenal flow waveform contains a diastolic retrograde portion, which is likely to occur in response to the high demanding anterograde flow of the kidneys during diastole, which again advocates for the presence of renal arteries ([Les et al., 2010a](#)). At the end of each cycle, the flow leaves the test section through the iliac arteries downstream. Two ball valves are installed on the way back to the main reservoir to mimic the peripheral resistance of the distal vasculature. They play a crucial role in reproducing the desired aortic pressure. To improve the performance of the simulator and optimize the flow distribution as well as the pressure magnitude, a separate line is designed to drain the renal flow and guide it back to the reservoir. For each round of measurement, the entire system is thoroughly drained using a variable speed pump; the water-glycerol solution is filtered in a separate circuit to remove the particles and stored for the next experiment. In order to better mimic the anatomy of the aorta and its elasticity, and in conjunction with the requirement of the visual inspection facility, compliant models of the aorta are made out of a two-part transparent silicone (40 Shore A hardness). The experiment is designed and carried out for 6 optically clear models of the abdominal aorta, five

aneurysmatic cases and a normal aorta, which is used to validate the results. The maximal diameter of the AAAs is between 30 mm, one of the standard baselines for AAA definition, and 50 mm, the conservative threshold for surgical intervention (Wanhainen et al., 2019). The geometries are not image or patient-specific based because this project is seeking to see how AAA progression in terms of maximum diameter as the primary therapeutic criterion results in varied flow patterns, turbulence and other characteristics including but not limited to the energy loss. Supplementary information regarding the choice of geometry and the model fabrication procedure is provided in Sec. 3.1.3.

As mentioned, the abdominal aorta begins at the level of the diaphragm where it is connected to the descending aorta. However, the test section only includes the segment between the renal arteries and the aortic bifurcation. Each model is vertically placed in an acrylic box. Note that for the case of internal flow through a model with curved walls it is essential to take this design parameter into account that a box with flat walls (view box) which is filled with the same mixture as the one circulating should surround the model so that the flow can be observed perpendicularly without refraction errors (Budwig, 1994).¹ In this work, the indices of refraction of the phantoms, the working fluid are in good accordance. To ensure that there is no distortion in the images, a bright colour target covered with a dot pattern with known dimensions is placed in the middle of the phantoms, and an image is taken while the box and the test section are filled with the working fluid. The distance between the centres is obtained, given that the system is calibrated, and the device pixel ratio is known. The distance on the image and the target should be the same to rule out the distortion, at least from the surface facing the camera. Fig. 3.3 shows that no difference is noticed between the target inside and outside the test section.

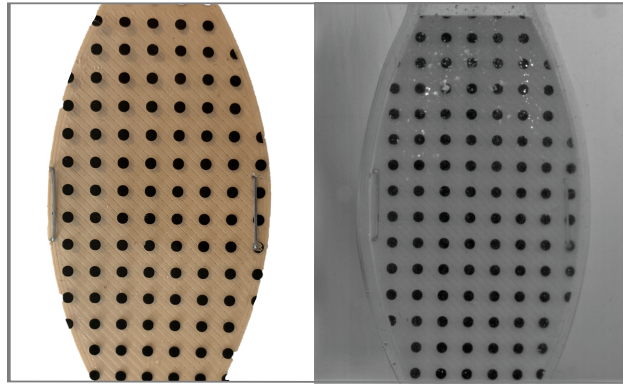


Figure 3.3: Distortion test. Left: flexible sheet with polka-dot pattern, outside the box. Right: the target device placed inside the AAA filled with the mixture. The image intensity is low since it is recorded via the high speed camera when the laser was switched off.

The replacement of different geometries is facilitated with the aid of two quick-disconnect connectors that are screwed to the bottom of the chamber from their coupling body side. The abdominal aorta is mounted on the coupling inserts and can be easily removed by pushing the button on the connectors.

The planes for PIV measurements are chosen to be the two orthogonal planes of interest used for screening and decision making namely, the sagittal and coronal planes. It has already been

¹ The liquid surrounding the aneurysm model can also be beneficial to mimic the environmental pressure inside the vessel.

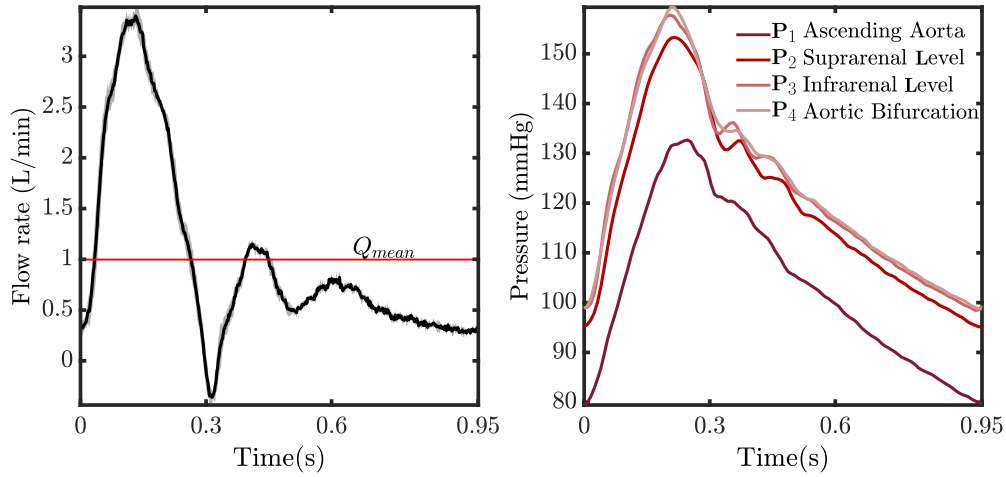


Figure 3.4: Acquired waveforms for the flow and the pressure for the normal case. Left: instantaneous flow rate at the inlet of the test section. Right: instantaneous pressure measured at 4 cross-sections: 1) right above the aortic valve; 2) upstream of the renal arteries; 3) in the proximal region of the aneurysm; 4) close to the aortic bifurcation.

discussed in [Ch. 1](#) that the overall consensus favours the anteroposterior diameter in the sagittal plane to be taken as the determining factor for diagnosis and intervention. The background theory, application and different steps of the method of acquisition are exclusively described in [Sec. 3.2](#).

3.1.2 Pressure and flow measurements

For the *in vitro* experimentation on the cardiovascular flow, one of the main concerns is to obtain realistic waveforms, which other than implementing an appropriate input profile is accomplished by mimicking the impedances along the arteries. Just as explained in [Sec. 3.1.1](#), in our setup, the peripheral resistance is mimicked with the adjustable valves, and the compliant aorta serves as the capacitor storing the energy during the ejection phase. For all the cases, pressure measurement is done at four locations (see [Fig. 3.1](#)); P₁: in the vicinity of the aortic valve, P₂: right before the renal arteries in the descending aorta, P₃: below the inflection point inside the aneurysm, and P₄: near the aortic bifurcation. The pressure is monitored and logged using a fibre optic pressure sensor (FOP-M200) with an FPI-HR2 module (FISO Technologies Inc.; Quebec, QC, CA). A small port is created on the aortic arch where a homeostasis valve is fixed to introduce the sensor (the port is also used to remove the trapped air). The fragility of the sensor requires careful treatment while guiding it to the target location. The measurement is then plotted in real-time and recorded with the EVOLUTION software (FISO Technologies Inc.; Quebec, QC, CA). The measured systolic and diastolic pressures are 153 ± 3 mmHg and 95 ± 3 mmHg, respectively. The numbers can be validated by referring to the *in vivo* data in [Les et al.](#), where it is stated that hypertension is commonly found in AAA patients explaining the slightly high values of pressure.

The average infrarenal flow rate is detected using a magnetic-inductive flow meter (AutomationDirect's ProSense FMM Series (-1002), Munich, BY, DE) which is positioned at the outflow trajectory of the iliac arteries and was kept away from any source that could cause a disturbance

in the flow (e.g., pump, valves, bend in the piping, reductions). This type of flow meter operates by using the magnetic-inductive measuring principle. When the measuring pipe is filled with a conductive fluid, the current-carrying coils generate a magnetic field. The ions of the liquid are diverted perpendicularly to the magnetic field, with the positive and negative charge carriers flowing in opposite directions. The induced voltage is measured by the two electrodes that are in contact with the fluid. Since the internal diameter is known, the measured voltage determines the average flow rate given its correlation with the average velocity. So, keep in mind that the functionality of the flow meter depends on the choice of the working fluid in terms of its conductivity to be more than $20 \mu\text{S}/\text{cm}$ and its viscosity to be less than 70 cST at 40° C . The properties of water-glycerol solution used in this thesis are compatible with these requirements. The computed average rate of the flow entering the abdominal aorta in the sagittal and coronal plane is 1 ± 0.18 and 0.97 ± 0.08 L/min. The acquired values comply with physiological flow properties reported in [Les et al. \(2010b\)](#) where 2D PC-MRI is employed to directly obtain volumetric flow data in 36 patients diagnosed with an aneurysm in the abdomen. The total inlet flow is equal to the sum of infrarenal flow and renal flow, which is measured roughly to be $0.9 \text{ L}/\text{min}$ ([Naidich et al., 1993](#)). When it comes to the validation of the blood flow simulations, it is preferable to validate the acquired pressure and flow values referring to the studies that examine the physiological parameters in AAA patients and not in healthy young individuals ([Olufsen et al., 2000](#)) because ageing and stiffened arteries make changes in the morphology and flow pattern of the infrarenal aorta, which is quite different from the normal aorta. Also, ultrasound data-driven references ([Fraser et al., 2008](#)) are likely not accurate since they measure centreline velocity waveforms at the infrarenal level. The volumetric flow waveform is then calculated assuming a Womersley velocity profile, which is not ideal since it maps an axisymmetric and periodic profile at the infrarenal level and can result in inappropriate inflow conditions and consequently misleading information regarding turbulence ([Les et al., 2010b](#)).

3.1.3 Replica of the aorta and AAAs

As depicted in [Fig. 3.1](#), the simulator includes a transparent silicone model of the aorta extending from the aortic root to the common iliac arteries, while the visualization is restricted to the segment between the aneurysm neck and the aortic bifurcation at the level of the fourth lumbar vertebra. Flow through the aorta before reaching the abdomen makes the infrarenal inlet boundary condition deviate from a laminar and periodic waveform, which actually turns out to be more realistic and counts as an asset when it comes to studying turbulence in the region of interest, namely, in the AAA.

The aorta is modelled in two parts that merge together at the hiatus of the diaphragm. Anatomically speaking, the reconstructed geometry does replicate some of the essential features of the human aorta, including the length, the three-dimensional curvature and the sinuses of Valsalva. Except for the renal arteries, which originate between the L1 and L2 vertebrates and presumably affect the AAA flow, other aortic branches and their corresponding flow rates are excluded from the design for simplicity. The model keeps a constant diameter of 30 mm along its centreline and before the isthmus, where a gradual radial reduction occurs to connect the upper part to the aneurysm model. The dimensions are consistent with the average measured values of the aorta ([Hager et al., 2002](#)).

As already explained, the focus of this study is to identify the fluid dynamic changes that occur in an AAA by increasing maximum anteroposterior diameter. For this purpose, the models are assumed idealized with different sizes and location of maximal diameter. Also, they are axisymmetric along

their longitudinal axis from the frontal view. Since diagnosis and management of an AAA is done on the basis of its size, one might think that realistic, patient-specific models ought to provide more clinically relevant findings. However, idealized models facilitate the study of different geometric features of aneurysms by changing the geometric parameter of interest while keeping the other features constant. The models do not involve complexities of the anatomical AAAs, although the initial design is inspired by the morphological parameters. Also, the effect of lumbar curvature has not been included in the design; however, the cases with $D_{\max} \geq 4$ cm are made non-symmetrical (with respect to the sagittal axis) to apply the effect of the spinal column. Detailed dimensions of the models are specified in Fig. 3.5. The length of the abdominal aorta extending to the bifurcation apex for all 6 cases is 16 cm. There is a tubular section at the entrance with the same diameter as the healthy abdominal aorta (20 mm). In 4 cases, the bulge starts 2 cm distal to the origin of the lower renal artery and lengthens 8 cm, while this length for the remaining aneurysmal case is 3.5 cm to check the effect of aneurysm length (Espinosa et al., 2002). The diameter of the renal arteries and the iliac arteries are 11 mm and 13 mm, respectively. The distance between the origin of the lower renal artery and the aneurysm neck is 20 mm. Compared to the literature, the renal arteries are made bigger to make sure that the flow is moving forward during the entire cycle and to maintain the desired distribution of the inlet flow.

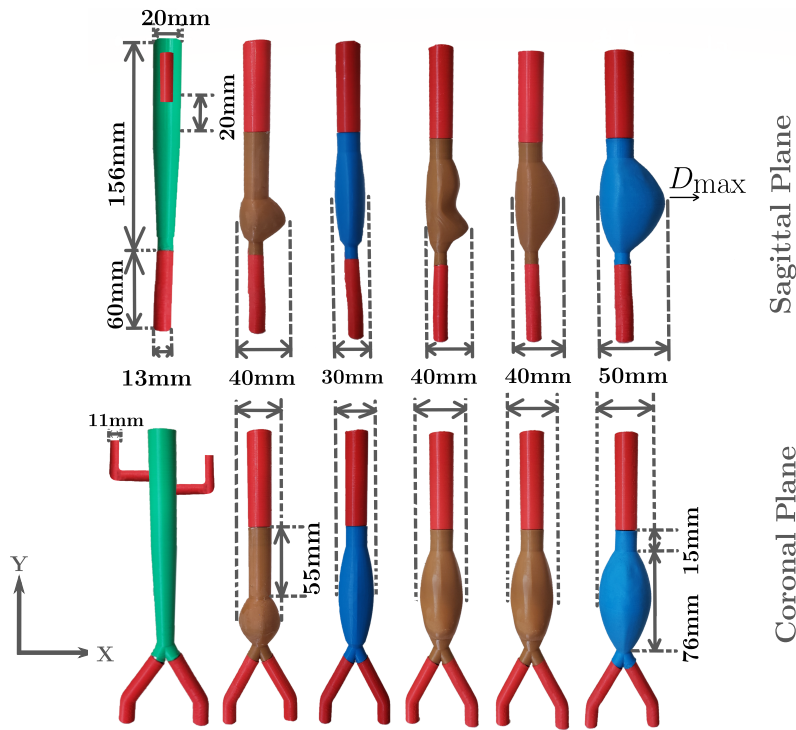


Figure 3.5: Dimensions and planar view of the 3D printed models that were used to fabricate the silicone phantoms.

The fabrication process of all the physical models is carried out in two steps; rapid prototyping and silicone moulding. First, they are all modelled in 3D design software and their surface geometry information is stored in an STL file, which is then imported to a slicing software, Cura LulzBot Edition (Fargo Additive Manufacturing Equipment 3D; Fargo, ND, US), to generate the required G-code to send to the 3D printer, LulzBot TAZ6 (Fargo Additive Manufacturing Equipment 3D;

Fargo, ND, US). Polylactic acid (PLA) is used as the feeding filament to print the upper section of the aorta in a single part at a layer resolution of 0.2 mm. The prototype is gently sanded and made ready for casting silicone onto it. The convex shape of the aneurysm constrained between the two narrower regions of the abdominal aorta makes it quite tricky to retrieve the silicone mould intact. The primary solution to deal with this issue is to cut through the mould (positives), detach it from the 3D printed models, suture, and seal it up. However, this is often highly susceptible to leak and also troublesome for visual inspection. An alternative approach adopted by [Mix et al. \(2018\)](#); [Doyle et al. \(2008\)](#); [Marconi et al. \(2018\)](#) is to use a mould composed of two outer and inner shells with a gap in between which is filled by pouring or injecting the mixture in. The inner shell in this technique is usually made up of dissoluble material and can be used only once, which is neither environmentally nor economically efficient. A straightforward but less affordable method is to use a 3D polyjet printer that can be fed with a broader range of material, such as flexible material that can mimic the tissue ([Cloonan et al., 2014](#); [Polanczyk et al., 2018](#); [Biglino et al., 2013](#)). Nevertheless, this method's major problem arises from the fact that the commercially available material might not have transparency, which is a critical feature required in PIV applications. Therefore, to avoid the problems mentioned above, an original technique is employed to manufacture the 3D printed parts of the aneurysm, which is inexpensive, versatile and reusable. The AAAs are printed in different pieces that are bonded together via neodymium magnets (Magnet Montreal; Montreal, QC, CA), see [Fig. 3.6](#). The middle part (bulge) is printed with a flexible filament (NinjaFlex), which is made from a specially formulated thermoplastic polyurethane (TPU) material. The layer resolution is set to be 0.1 mm with an infill density of 0%, to prepare moulds that can be inflated and deflated. For the straight parts, the setting is adjusted the same as what was used for the upper part of the aorta. Each piece is printed with a cylindrical hole where the magnets are secured in place using super glue.²

The compliant phantoms are made by painting a two-component silicone material (Polycraft T-4, MBFiberglass; Newtownabbey, ANT, NIR) over the surface of the 3D printed parts. The product (base and the curing agent) with a Shore hardness of 40A provides sufficient flexibility to extract the mould without breaking it with a 400% elongation at break and 26 kN/m tear strength. The cured mixture is transparent and compatible with PIV in terms of having a similar refractive index (RI) as those of the working fluid and the acrylic chamber wherein the AAA is submerged. The mixture is prepared in a ratio of 10 parts silicone base to 1 part curing agent by weight while the total mass varies for each case due to differences in surface area of the geometries. The two parts are mixed very well and carefully to suppress the formation of air bubbles, although it is unavoidable, and if left untreated can interfere with the laser sheet. Thus, to remove the air bubbles, the silicone batch was placed in a container connected to a vacuum pump for ten minutes and then was exposed to the open air for five more minutes to get rid of the remaining bubbles. Leaving the batch for an extended period is not recommended since it starts to cure and becomes difficult to brush. Each model is mounted on a rotating mechanism. The silicone mixture is painted on the surface with homogeneous brush strokes. It is critical to keep pushing the brush onto the surface to prevent the redevelopment of air bubbles. For the flexible section, this cannot be done freely, so the bubbles are eventually removed from the surface using a tiny needle. When the mould is coated thoroughly, the machine is switched on to rotate slowly, which provides an even and smooth coverage. The curing process is expedited by heating the ambient air. The procedure is repeated for five extra layers. Finally, the walls are detached, the rigid parts are removed by pulling against the magnetic force.

² The pieces will better attach if the coupling magnets exactly coincide.

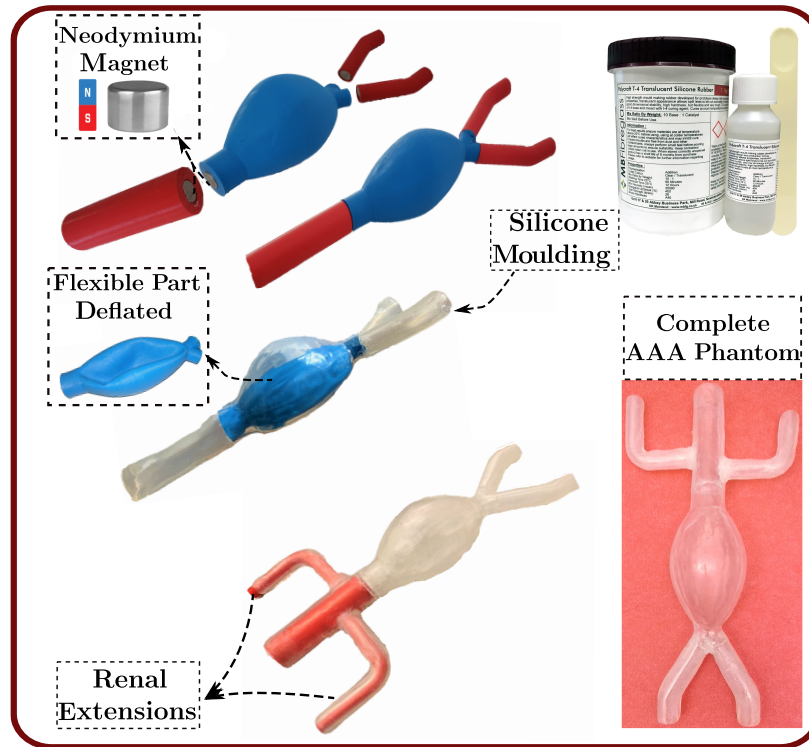


Figure 3.6: Fabrication process of a sample AAA silicone model.

Now, the flexible part can be accessed through the straight inlet. First, the walls are detached using a medical spatula (injecting a small amount of a lubricant (e.g., oil) can be helpful; however, it is essential to wash the mould thoroughly before proceeding with the rest of the process). Then, a tiny hole is punched with a syringe to deflate the balloon-like aneurysm and make it easy to come out. An extra layer of silicone is painted on the internal wall of all the physical models to make the replica transparent and ideal for PIV. Ultimately, the right and left renal branches are added to the phantoms by coating on two elbow-shaped 3D printed extensions placed parallel to the lateral plane of the abdominal aorta.

Overall, the wall thickness of the aorta and AAAs are 2 mm, consistent with the literature (Kemmerling and Peattie, 2018), albeit the adopted manual technique cannot guarantee a constant thickness all over the moulds.

3.1.4 Blood-mimicking fluid

An optically clear aqueous glycerol solution with a volume percent of 40% glycerol and 60% distilled water is used as the working fluid in the mock loop system. The reason for this choice lies, in its ability to reproduce the bulk dynamic viscosity of the blood and a refractive index (RI) matching that of the phantom material. The adjustment of both properties is made simultaneously by changing the concentration rate of the suspending fluid (glycerol). However, the latter is compromised because a perfect RI match is achieved by adding more glycerol, which entails a higher viscosity and sequentially needs an elevated temperature for the mixture to reduce the viscosity. Another common practice to increase the RI is adding sodium iodide (NaI) to the mixture. In this method,

which is not employed here, fluid viscosity does not change though the resulting density is well above blood. Additionally, In terms of cost, safety and solution discoloration concerns, NaI is not profitable and has been reported to disrupt non-Newtonian fluid behaviour (Brindise et al., 2018). The dynamic viscosity is obtained by multiplying the density and the kinematic viscosity at the working temperature.

The density is calculated by weighing different volumes of the liquid on a digital scale with a resolution of 0.01 g. The measured value equals $1106 \pm 20 \text{ kg/m}^3$, which is close to the reported values ($1043\text{-}1060 \text{ kg/m}^3$) for density of blood (Vitello et al., 2015).

A Cannon-Fenske routine viscometer (size 75, Cannon Instrument Company, State Colege, PA, US) is used to find the kinematic viscosity. For any calibrated viscometer, the time for a fixed volume of fluid pulled by the gravity to flow through its capillary at a specific temperature is proportional to the kinematic viscosity with a constant that is provided by the company and can be found on the associated specification sheet. Note that, depending on the working temperature, the constant should be either interpolated or extrapolated. To measure the efflux time, the viscometer is inserted into a holder and placed in a bath (not necessarily filled with the same liquid) to reach thermal equilibrium (e.g., at room temperature). The water-glycerol sample is poured into one side of the viscometer, and suction is applied to the other side using a syringe and a tight tube. When the negative pressure is removed, the flow starts flowing downward, and the time it takes for the fluid to pass through the specified marks is recorded with a stopwatch. The process is repeated multiple times, and a kinematic viscosity of $3.7 \pm 0.04 \text{ cSt}$ is computed as the product of the efflux time and viscometer constant. Therefore, the dynamic viscosity of the blood analogue used in this thesis is 4.1 cP, which falls within the reported physiological range for blood's viscosity at the normal human body temperature ($37 \text{ }^\circ\text{C}$), $4.4 \pm 0.5 \text{ cP}$ (Yousif et al., 2011). It should be recalled that this similarity is attained while the experiments are performed at room temperature ($23.5 \pm 0.5 \text{ }^\circ\text{C}$). The observed refractive index of the mixture is 1.39 and close enough to the index of refraction of the silicone phantoms and also to that of the acrylic box, which reduces light deviations and improves the visualization quality. Regarding the shear-thinning (non-Newtonian) behaviour of the blood, this feature does not apply in arteries with a diameter of more than 0.5 mm and shear rate higher than 100 s^{-1} like in the abdominal aorta (Vlachopoulos et al., 2011; Fahraeus and Lindqvist, 1931; Brooks et al., 1970), which justifies the use of water-glycerol as a Newtonian blood analogue since the minimum lumen size of the region of interest (the abdominal aorta) is 20 mm. However, this choice would lead to a higher rate of viscous dissipation. Still, in studies such as Deplano et al. (2014), to emulate the macroscopic shear-thinning feature of the blood, Xanthan gum is added to the solution. However, this can be a burden to the experiment if the flow is activated with a gear pump, which can induce large deformations that deteriorate the molecular network of the Xanthan gum and therefore reduce the dynamic viscosity (Benard et al., 2007).

3.2 PARTICLE IMAGE VELOCIMETRY

The instantaneous abdominal aortic flow velocity field in the presence of an infrarenal aneurysm is quantitatively extracted with the aid of 2D (planar) time-resolved particle image velocimetry. The concept and the details regarding the implementation and evaluation of the PIV data will be presented in this section.

3.2.1 Basic principles

The velocity of a moving fluid (e.g., a pure liquid medium) cannot be easily revealed through measuring the travelled distance for a given duration. Also, indirect methods of obtaining the velocity via measuring other quantities such as the pressure are problematic. This is because the probe can disturb the flow and the information is limited to a single point or at most to the averaged velocity of a region of interest. In turn, these methods are inappropriate and incapable of resolving detailed information about a flow with a transient nature, such as in cardiovascular applications. These shortcomings have been addressed with the development of non-intrusive optical measurement techniques such as particle image velocimetry (PIV), which integrates digital image processing and flow visualization. In PIV, the position of an ensemble of tracer particles is captured remotely and instantaneously. In this method, the velocity is obtained indirectly by evaluating the displacement of particles between two time instants. To perform a time-resolved 2C-2D PIV measurement, the working fluid is initially seeded with properly selected tracer particles, which will be exposed twice (with a short time delay) to a laser light sheet over a known time duration which should be short enough to freeze the particle motion. The light is then scattered by the particles, and the fluid motion in a target plane of the test section (e.g., the sagittal plane of the abdominal aorta) can be observed. A camera that is usually positioned perpendicular to the light sheet records the flow either on two separate frames for each illumination or on a sequence of single frames at a specified frequency. The imaging system calibration is applied by defining the physical flow field dimension to proceed with PIV evaluation. In the next step, the particle (recorded) images are divided into small sub-areas called the interrogation area, an area around the point where we want to find the velocity, assuming a uniform displacement for its surrounding particles. Corresponding interrogation areas in each particle image pair are compared by means of a cross-correlation technique yielding the most probable displacement of the particles. A velocity vector map for each window in all the successive images is constructed. In effect, it is assumed that the particles faithfully follow the fluid motion, and the local flow velocity can be deduced from the resulting particle velocities with small differences. Figure 3.7 briefly sketches a typical procedure of velocity vector field computation within the plane of interest. The raw data is then validated based on different criteria; false vectors are detected and replaced, and the 2D flow field information on an Eulerian basis and with a desired spatial resolution is extracted, which can be analyzed to quantify secondary parameters related to the flow.

3.2.2 Implementation

Tracer particles

As described earlier, in PIV, the velocity of the particles is substituted for the flow velocity. In order to select an ideal tracer particle, optical properties and dynamic response of the particles with respect to the flow should be taken into account. Both aspects are tightly dependent on the size, shape, density of the particles, as well as the fluid properties (e.g., density, viscosity and acceleration). In order to pick the right particles, an optimization is required since smaller ones can faithfully track the fluid motion and do not alter the flow, whereas the light is more efficiently scattered with larger particles. In this work, polyamide seeding particles (PSP-50, Dantec Dynamics; Skovlunde, CPH, DK) with a mean particle diameter of $50\ \mu\text{m}$ are added to the blood analogue. In terms of

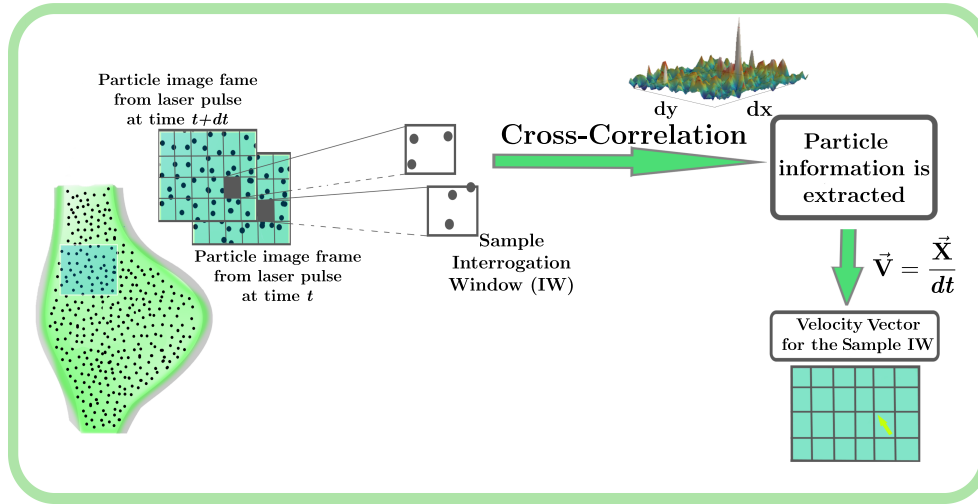


Figure 3.7: Principle concept of velocity vector computation in a 2D planar PIV system.

shape, they are round but not perfectly spherical, with a deviation of $\pm 20 \mu\text{m}$. Aside from the size, the ratio of the refractive index of the particles to that of the medium affects the light scattering intensity. In the case of PIV applications for liquid flow (e.g., water-glycerol solution) seeded with polyamide seeding particles, the RI ratio is small, roughly 1.08, which yields a lower scattering efficiency. Therefore, to maintain enough scattering, larger particles (for water flow experiments) should be employed. Also, in water flow, the neutral buoyancy condition can be obtained effortlessly by using materials as heavy as water (e.g. polyamide, hollow glass spheres). Particles used for this thesis have a density of 1030 kg/m^3 . Note that a close match between the density of the fluid and the particles prevents errors due to velocity lead/lag related complications. Furthermore, the light scattering also depends on polarization and observation angle. In general, the light scattered paraxially (i.e., at 0° or 180°) from a linearly polarized incident wave is linearly polarized in the same direction, and the scattering efficiency is independent of polarization. In contrast, the scattering efficiency for most other observation angles (90° for the current work) strongly depends on the polarization of the incident light (Raffel et al., 2018). For spherical particles with diameters larger than the wavelength of the incident light (typically $\lambda=527 \text{ nm}$ for PIV), the Mie-scattering regime is applicable.

To inspect whether or not the particles follow the fluid motion with enough fidelity, response time and Stokes number should be evaluated. The former, defined as $\tau_p = \frac{d_p^2 \rho}{18\mu}$, is a measure of the likelihood of the particles to reach velocity equilibrium with the fluid in response to sudden variations in the flow field. It is however not adequate, and particle Stokes number ($Stk = \frac{\tau_p}{\tau_f}$) should also be considered. τ_f stands for the characteristic time scale in the flow. The flow following fidelity is marked acceptable for a threshold of the Stokes number below 10^{-1} which complies with its value in this work (Raffel et al., 2018).

In liquid flow analysis using PIV, with seed particles smaller than $1 \mu\text{m}$, the cumulative effect of collisions between the particles and fluid molecules triggers random motion of particles and prevents them from following the flow exactly (Raffel et al., 2018). This phenomenon, called Brownian motion, is only a matter of concern in μPIV and its effect is trivial in this work.

For each round of measurements, seeding is done by stirring particles first in a small container and then into the reservoir until they are all evenly distributed over the field of interest. In order to preserve a high-quality PIV recording, the particle density is a critical factor that has to be adjusted since failure in identifying individual particles in a heavily or sparsely seeded area will lead to difficulties in computing the velocity vectors. A higher amount of seed particles nonetheless can contribute to a better scattering efficiency, although it is not practical due to its adverse effect on background noise. In a nutshell, according to [Adrian et al. \(2011\)](#), to obtain a valid correlation peak with a certainty of 70-80% or a higher certainty of 98%, the average number of particles per interrogation window is recommended to be 3-4 or above 10, respectively. To fulfill this criterion, at the beginning of each experiment, the liquid was seeded gradually. Preliminary images of the area of interest were recorded, and a sample number of interrogation windows was randomly examined to see if they contained the desirable number of particles (> 10). If not, more particles were added to the mixture until the density of the particles and intensity of the images were satisfactory.

Optical system and recording parameters

The object plane in this work is adjusted to include the proximal neck downstream of the renal arteries and the dilated portion, extended to the aortic bifurcation. The side branches are not explicitly covered in the image acquisition, although their presence in the model helps to simulate the flow in the aneurysm more accurately. The particles in the region of interest are illuminated with a thin light sheet presumed to have a uniform intensity parallel to the field of view. The light source was a diode-pumped Nd:YLF laser (LDY301, Litron; Rugby, Warks, GB) emitting light pulses each lasting for 100 ns at a frequency of 0.2-20 kHz. The maximum energy offered per pulse is 10 mJ at the wavelength of 527 nm. The light sheet is generated through a cylindrical lens and is emitted toward the test section while being tuned with an additional lens to be as thin as possible with a roughly uniform thickness of 1 mm cutting across the midplane of the phantom in each configuration. In addition, using a right angle triangle ruler placed on the edge of the acrylic box, the laser sheet is aligned perpendicular to the box to avoid any light refraction. Note that the box and the laser system are both leveled using a standard spirit level.

A high-speed camera (Phantom v9.1, Vision Research Inc.; Wayne, NJ, US) with an AF Micro NIKKOR 60mm f/2.8D lens (Nikon; Tokyo, JP) is used to capture the particle images. The camera has a CMOS sensor (36×24 mm) with a maximum acquisition frequency of 1016 Hz for 1632×1200 px image size. The spirit level indicator on the tripod is monitored to level the mounted camera. The camera is initially placed in front of the acrylic chamber so that the acquired image includes the desired field of view. The camera's position was optimized by making its sidewall parallel to the acrylic chamber's sidewall while observing the spirit level indicator on the camera. Fulfilment of perpendicularity for all three components (camera, laser, and the simulator) would prevent the problems associated with distortion due to the small mismatch in the refractive indices. Finally, the lens of the camera was adjusted to ensure that the particle images are focused, and the diameter of the tracer particles in the image is of the order of 20-30 μm . Note that the evaluation technique that is chosen affects the optimal particle image diameter. This diameter is reported to shift to larger values from around 2 pixels for single-pass evaluation to 3-6 pixels for multi-pass evaluation ([Raffel et al., 2018](#)). One more factor to be considered is the minimum size of the particle images not to be too small to avoid a systematic error, called peak-locking, which occurs because a continuous intensity distribution of very small particle images is insufficiently sampled by the discretized digital

camera sensor. Thus, if the low intensities of the pixel next to the one containing the maximum intensity of a particle image are on the order of the image noise level, the sub-pixel position is lost and cannot be reconstructed. The pixel-based dimension should be converted to the physical dimension of the system to evaluate the recorded data. To do so and before proceeding with the measurements, a 3D printed part with an attached ruler coinciding exactly with the measurement plane was placed in the silicone model and an image was recorded (no need to have the laser on). By selecting two points with a known distance on the ruler image, the conversion factor was found to be 13.18 px/mm with slight variations in different cases.

As discussed in [Sec. 3.1.1](#), two orthogonal planes are used for the PIV measurements. So, for each plane, once the system was assembled and calibrated for the first silicone phantom, no more change was made to the position of the camera, laser and the simulator except the silicone model that was replaced, although due to unexpected displacements and human errors, the calibration was checked in advance before starting to record the flow for each case.

In a double-pulsed acquisition system, the decision on the optimal time delay between the pulses should be made by taking four criteria into account, which will be described briefly here. It should obviously be larger than the estimated time response of the seeding particles, and large enough to resolve even the smallest displacements. The interval between the light pulses should be assigned so that in-plane and out-of-plane loss of particles is minimized. The former is satisfied by trial and error while requiring that the fastest particles not to move more than 1/4 of the interrogation window length, or the initial window size in case a multi-pass approach is taken (i.e., no more than 16 pixels for a 64×64 px window) ([Adrian et al., 2011](#)). If this works for the selected particles with the highest velocity and they remain in both frames, it can be generalized to the slower particles as well. However, using iterative evaluation with window-shifting techniques in modern algorithms allows in-plane loss of pairs to be treated with conformity ([Scarano and Riethmuller, 2000](#)). Furthermore, regarding the out-of-plane loss-of-pairs, the general practice recommended in [Scharnowski et al. \(2017\)](#) is to keep its value sufficiently small to ensure the presence of a minimum required number of particle image pairs within the interrogation window (typically more than 5). Another guideline to address this issue is to make sure the particles do not move more than 1/4 of the laser sheet thickness. Detailed methodology to evaluate the out-of-plane behaviour of the particles can be found in [Di Labbio \(2019\)](#).

In summary, in this work, the time delay between two laser pulses was set to $900 \mu\text{s}$. The number of images and the frequency of the acquisitions were optimized to improve the temporal resolution and to keep the recording time close to the cardiac cycle period ($T=0.952$ sec for the heart rate of 63 bpm). Five hundred (500) double-frame images were recorded at a frequency of 525 Hz. A summary of the experimental conditions is provided in [Tab. 3.1](#). For all the cases, the system was kept working well ahead of the PIV recording to skip any disturbances that occurred at the beginning of the simulator's function. For each recording, the flow waveform in the descending thoracic aorta was recorded and transmitted to LabVIEW, where the beginning of the systole was accompanied by a the digital trigger to be sent to the high-speed controller of the PIV system which would let all the recordings begin at the same specific time instant. To check if the experiments were repeatable, the PIV measurements were repeated 4 times for each case while the system had been kept working continuously. Also, an extra recording was made when the system started to operate after it was switched off for a while. For each case, this whole recording procedure was shortened as much as possible because the slow nature of the flow could cause particles to stick to the anterior wall due to flow stagnation, which could affect the intensity of the scattered light.

To question the effect of using phantoms fabricated manually, for the geometry with the largest diameter, the experiment was carried out with two similarly made silicone moulds, which yielded the velocity variations within the same range. The variations can stem from the imperfections in the simulator and the activation system, noise, mild turbulence, and uncertainties related to the velocity vector calculations.

Regardless of the efforts made to improve the quality of the experiments, the study suffers a constraint regarding the PIV measurements on a planar basis. As previously discussed, the current study aims to inspect flow characteristics in AAAs while the disease becomes severe in terms of increased maximal anteroposterior diameter as the main decision-making criterion. Therefore, since the third velocity component in the target plane is relatively small (Deplano et al., 2016), the flow in the targeted plane can be assumed 2D and resolved by standard 2D-2C PIV. Note that a full 3D analysis of the flow dynamics in the abdominal aortic aneurysm has not yet been done neither *in vivo* nor *in vitro* except for the study conducted by Deplano et al. (2016) in which 3 velocity components were assessed in consecutive planes through stereoscopic PIV but at specific time instants. In Ziegler et al. (2019) 4D MRI was employed to quantify blood stasis in an AAA in the same sagittal plane although the temporal resolution of 35-40 ms is far less than the one that can be achieved with time-resolved PIV (i.e., 1.9 ms in this work) which is the first of its kind in the case of AAAs.

Table 3.1: Summary of the experimental conditions.

Working Fluid Properties	Water-glycerol ratio	60-40 (% by volume)
	Density (ρ)	1160 kg/m ³
	Dynamic viscosity (μ)	0.0041 Pa s
	Refractive index (RI)	1.39
	Temperature	23.5±0.5°C
Simulator Operating Conditions	Infrarenal flow rate (Q_m)	1±0.18 L/min
	Cardiac period (T)	0.952 sec
	Heart rate (HR)	63 bpm
	Systolic pressure (SBP)	153±3 mmHg
	Diastolic pressure (DBP)	95±3 mmHg
Image Acquisition Settings	Number of images (n)	500
	Frequency (f)	525 Hz
	Laser time delay (dt)	900 μ s

3.3 POST-PROCESSING

The PIV images should be further processed to obtain the velocity vectors, which have to be validated before further steps are made to extract essential features of the flow field. The procedure will be explained in greater detail in this section.

3.3.1 Velocity vector computation

After the images were recorded, in order to reduce the computation time, a mask is applied to exclude the particles outside of the region of interest from the evaluation. Statistical evaluation of PIV recordings is performed to match particle pairs and to find the displacement between two patterns of randomly distributed particle images. Each pair of images is subdivided into correspondingly small interrogation windows (typically 30–250 samples in each direction). In this work, a double frame/single exposure recording technique was employed; the evaluation is performed by cross-correlation with a standard fast Fourier transform. For the sampling, an iterative multi-pass scheme is implemented starting from a 64×64 px interrogation window, automatically halved to a 32×32 px and finally refined to a 16×16 px window size with a round Gaussian weighting function. Using a larger initial window is beneficial since it is large enough to obey the one-quarter rule, and a full range of particle displacements can be captured. On the other hand, using a smaller final window (iteratively repeated three times) leads to the resolution of smaller flow scales. The final spatial resolution with 50% overlap is $0.6 \text{ mm} \times 0.6 \text{ mm}$. For more details regarding the implementation of the interrogation algorithm and the software settings, the reader is referred to Raffel et al. (2018) (chapter 5) and Di Lobbio (2019).

Vector validation

In order to detect false vectors (outliers), we need to validate the computed velocity vectors and replace the outliers. To begin, a median filter is applied 2 times to the velocity field. By using a local median filter for vector validation which was proposed by Westerweel (1994), a vector is recognized as valid if its deviation from the median of its neighbouring vectors (typically 8) divided by the standard deviation of the neighbours is lower than a specified detection threshold. It is convenient to use a median filter since it works irrespective of the frame of reference (i.e., it treats the spurious vectors inside a moving vortex and inside a stationary vortex similarly). Also, the magnitude of the vectors does not impact how it functions since the threshold for elimination is a user-defined factor of somewhere between 1 and 3 times the standard deviation (e.g., 2 in this work). Moreover, it is somehow tolerant of surrounding false vectors, and it adapts to variations in the velocity gradient since the standard deviation increases in regions of higher velocity gradients. The PIV software implements the median filter by first checking if any of the 8 neighboring vectors in a 3×3 window are spurious and does not consider them for the average and deviation computation. If a vector is suspected as false, the other 3 highest correlation peaks (stored in the vector buffer) are checked and if applicable substituted for the spurious vectors (LaVision, 2007).

Another criterion used to eliminate the spurious vectors is the peak ratio factor or the Q-factor, which is defined as $Q = \frac{P1-min}{P2-min}$. P1 and P2 are respectively the first and the second highest correlation peaks, and *min* is the lowest value in the correlation plane. The ratio can serve as a visual indicator of the vector quality. This ratio is usually in the range of 1.2-1.5. A high ratio (above 1.5 or 2) indicates that the vector is quite reasonably valid. In contrast, a ratio close to 1 implies that the highest peak is likely to be a false random peak (LaVision, 2007). In this work, vectors with Q value lower than 1.5 are regarded as spurious and removed.

Eventually, the empty spaces are replaced by interpolation. An average of the 4 non-zero valid neighbour vectors is calculated and inserted (a bilinear interpolation can recover more than 80% of the data). At this stage, comparing the filtered vector field with the raw velocity vectors, the total number of replaced vectors in the normal case accounts for about 0.25% and 3.8% in the

sagittal and coronal plane, respectively. For the former, the most uncertain dataset is related to the case with a maximal diameter of 4 cm, where approximately 4% of vectors were detected spurious after applying the median filter and the Q-criterion. In the coronal plane, the maximum number of replaced vectors is 4.4%, attributed to the model with $D_{\max} = 3$ cm.

Uncertainties

A combination of different factors, in the entire measurement chain related to the experimental set-up (e.g., flow characteristics, recording procedure, choice of evaluation techniques) contribute to the total inaccuracies and imprecision of a PIV measurement. Using *a priori* information in the experimental design can minimize these errors; however, this is not always applicable. Since the total error affecting the measured value (velocity vector) is unknown and nonuniform throughout the entire flow field, it is indispensable to quantify the instantaneous local uncertainty of PIV velocity fields. In principle, the role of uncertainty quantification (UQ) is to estimate the interval of the total error with a certain confidence level (Sciacchitano, 2019). The uncertainty of a PIV measurement is affected by several parameters. These include the size and shape of particle images, seeding density, illumination intensity variations, turbulent fluctuations, velocity gradients, noise and image interrogation algorithm. There are also systematic errors (hidden in nature) related to the tracer particle response, timing and synchronization, perspective and calibration errors. The relevant uncertainty of the latter type cannot be quantified through analyzing the image recordings (Raffel et al., 2018).

Practically, the uncertainty analysis can be undertaken with either *a priori* methods using theoretical modelling of the image analysis algorithm and/or Monte Carlo simulations or using one of the developed *a posteriori* approaches listed in Sciacchitano et al. (2015). Uncertainty quantification can be performed by identifying all the aforementioned parameters and determining their effect on the overall uncertainty (Timmins et al., 2012). It can also be implemented by analyzing the correlation functions inspired by the fact that the effect of all the parameters is implicitly embodied in the correlation (Wieneke, 2015; Xue et al., 2014). However, the necessity of calibration of each particular method for the PIV evaluation software makes the uncertainty quantification relatively complicated (Raffel et al., 2018).

The uncertainty of the PIV data in this work, following the guidelines in Raffel et al. (2018), is estimated to be less than 5% with the minimum 95% confidence level in the velocity fields.

3.3.2 Velocity gradients calculation

Performing standard planar PIV will result in a velocity vector field made up of only the u and v components, which can be differentiated in the x and y directions. As a result, the out-of-plane vorticity component, w_z , the in-plane shearing and elongation strains are the only components of the deformation tensor that can be computed. Since the velocity components are projected into an evenly 2D spaced grid, finite differencing has to be used to estimate the velocity gradients yielding a relatively high error and uncertainty, highlighting an important drawback of particle image velocimetry. Nonetheless, in order to take advantage of the higher-order derivative schemes to reduce the truncation error and to deal with their disadvantage which is noise amplification, a noise-optimized fourth-order scheme, namely, the hybrid compact-Richardson scheme, is applied to the grid points inside the flow domain. The expressions provided in Eq. 3.1 & Eq. 3.2 were used,

for instance, to evaluate the derivative of the velocity component (u) in x direction at a selected gridpoint (k).

For the nodes at the boundary, the forward compact scheme with the highest possible order corresponding to the available points is used (Etebari and Vlachos, 2005).

$$\frac{\partial u}{\partial x} \Big|_k = \sum_{j=1,2,4,8} \frac{w_j}{w} \frac{\partial u}{\partial x} \Big|_{k,j} \quad (3.1)$$

$$w = 1239, \quad w_1 = 279, \quad w_2 = 1036, \quad w_4 = 0, \quad w_8 = -69$$

$$\frac{\partial u}{\partial x} \Big|_{k-1,j} + \frac{\partial u}{\partial x} \Big|_{k,j} + \frac{\partial u}{\partial x} \Big|_{k+1,j} = a \frac{u_{k+1,j} - u_{k-1,j}}{2j\Delta x} \quad (3.2)$$

$$\alpha = 1/4, \quad a = 3/2$$

The uncertainty in the differentiated components of a PIV measurement (i.e., the velocity gradients) is proportional to the uncertainty estimation for the velocity divided by the local spatial differences Δx on the neighbouring data which means that the finer the grid, the more noise is produced. Hence, the uncertainty quantification in the velocity gradients may end up in higher values around $\pm 10\%$ for interior nodes to $\pm 20\%$ for the nodes at the boundary (Di Labbio, 2019).

3.3.3 Viscous energy dissipation

With the velocity gradients calculated, energy loss characteristics can be quantified and analyzed in terms of the viscous energy dissipation rate $VEDr$ and the total energy loss during one cardiac cycle for different cases. Viscous dissipation refers to the irreversible process whereby the work done by adjacent fluid components moving at a different velocity is transformed into internal energy (i.e., heat). Similarly, VED rate is a measure of how adversely the flow is losing its kinetic energy due to viscous friction and deformation. It is more dominant in regions with a higher rate of elongation and shearing strain (e.g., in shear layers). As mentioned in Sec. 4.2, clinically speaking, VED rate is an important metric representing the increase in workload on the left ventricle and serving potentially as a hemodynamic marker of valvular disease severity. In the theory of classical fluid dynamics, the point-wise viscous energy dissipation rate is defined as the scalar product of viscous stress (τ) and strain rate (S) (Batchelor, 2000). In the case of a 2D incompressible flow field similar to the dataset used throughout the current thesis, $VEDr$ is calculated via equation Eq. 3.3 (Pedrizzetti and Domenichini, 2005; Di Labbio and Kadem, 2018).

$$VEDr = \frac{\mu}{2} \int_A \left(\sum_{\forall i,j} \left(\frac{\partial V_i}{\partial x_j} + \frac{\partial V_j}{\partial x_i} \right)^2 \right) dA \quad i, j = 1, 2 \quad (3.3)$$

μ is the dynamic viscosity of blood, V is the velocity vector, and i and j account for the coordinates of the 2D Cartesian coordinate system. Note that the total energy loss during one cardiac cycle is further computed by integrating the dissipation rate values over the entire domain for all time instants.

3.3.4 Proper orthogonal decomposition

As mentioned in [Sec. 2.4](#), as a means to decompose a dataset into a linear combination of a set of modes and their corresponding expansion coefficients, the POD algorithm is fundamentally looking for an optimal set of basis functions that fulfills the orthonormality relation. Depending on the flow properties and the desirable information, the decomposition can split time and space or it can result in modes that are functions of time and space. While the latter is more employed in the early applications of POD (classical POD), in the framework of this work, the space-only POD modes are computed to be spatially dependent ($\phi_j(\mathbf{x})$) with their time dependent weights ($b_j(t)$). The steps to take in order to apply POD on a fluid flow are described as follows.

$$\mathbf{X} = \sum_{j=1}^n b_j(t) \phi_j(\mathbf{x}) \quad (3.4)$$

POD implementaion

- **Step 1**

First, we need to construct the input data or snapshot matrix (\mathbf{X}) using the variable field of interest, which is considered here as the velocity vectors acquired over n equispaced discrete time instants through PIV measurement.

$$\mathbf{X} = \begin{bmatrix} \mathbf{x}(t_1) & \mathbf{x}(t_2) & \dots & \mathbf{x}(t_k) & \mathbf{x}(t_n) \end{bmatrix} \quad \mathbf{x}(t_k) = \begin{bmatrix} u_{1k} \\ u_{2k} \\ \vdots \\ u_{mk} \\ v_{1k} \\ v_{2k} \\ \vdots \\ v_{mk} \end{bmatrix} \quad (3.5)$$

Each column of \mathbf{X} in [Eq. 3.5](#) contains the velocity at a given time instant t_k along the entire period while u and v denote the two velocity components at m spatial grid points. It should be recalled that it is common practice to focus on modal structures associated with fluctuations leading to the extraction of spatial modes that capture only the regions with fluctuation. For this purpose, the temporal mean of the vector field being examined is often subtracted, which impacts the interpretation of the results although the subsequent calculations for POD remain the same. However, this is not implemented in this work since the mean flow can serve as a reference when comparing the acquired modes with a lower rank. Also, the mean flow would be essential to reconstruct the flow field using a truncated number of modes.

- **Step 2**

When the flow data is properly rearranged, POD can be performed through three different approaches; the classical POD method, the method of snapshot, and the singular value decomposition (SVD). The classical method solves the eigenvalue problem of size $2m \times 2m$ for the covariance matrix of $R = \mathbf{X}\mathbf{X}^T$. The computed eigenvectors are known as the POD modes and the eigenvalues correspond to the kinetic energy captured by the respective POD modes. But, in the case of PIV measurements with vector fields including a significantly high number of grid points $m \gg n$, it is not practical to solve the eigenvalue problem $\in \mathbb{R}^{2m \times 2m}$ (Taira et al., 2017). The method of snapshots presented by Sirovich (1987) has addressed this issue by replacing the covariance matrix with the temporal correlation matrix ($C = \mathbf{X}^T \mathbf{X}$) with a smaller size ($n \times n$) that makes the eigenvalue problem computationally easier to solve. The method is relying on the similarity of the nonzero eigenvalues yielded from both eigenvalue problems.

$$C = \sum_{i=1}^n (x(t_i)^T x(t_i)) = \mathbf{X}^T \mathbf{X} \quad (3.6)$$

- **Step 3**

The smaller eigenvalue problem (Eq. 3.6) is solved. Since, the velocity vectors are chosen for the decomposition, the resulting eigenvalues (λ_j), which are sorted from maximum to minimum determine the kinetic energy content of the POD modes.

$$C\psi_j = \psi_j \lambda_j, \quad \psi_j \in \mathbb{R}^n, \quad \lambda_1 \geq \dots \geq \lambda_n \geq 0 \quad (3.7)$$

$$C\Psi = \Psi\Lambda$$

Ψ denotes the eigenvectors of the temporal correlation matrix and Λ is the diagonal matrix of eigenvalues.

- **Step 4**

The eigenvectors of the temporal correlation matrix (C) make up an expansion basis to recover the eigenvectors of the original correlation matrix or the POD modes (ϕ_j) through the shared eigenvalues. Proper orthogonal modes include flow structures with different spectral information.

$$\phi_j = \frac{\mathbf{X}\psi_j}{\sqrt{\lambda_j}} \quad (3.8)$$

$$\Phi = \frac{\mathbf{X}\Psi}{\sqrt{\Lambda}}$$

- **Step 5**

Finally, back to Eq. 3.4 which implies that the flow at each time instant can be represented by a linear combination of the modes, we can calculate the POD mode weight matrix (B) which contains the temporal coefficients in its rows. The columns of B can be employed as the amplitudes required for flow reconstruction at a given time.

$$B = \Phi^T \mathbf{X} \quad (3.9)$$

As mentioned, an alternative to the classical and snapshot methods is SVD which is more robust against roundoff errors and can be applied directly to the data matrix (\mathbf{X}) to extract the POD modes without any need for the correlation matrix. However, it's not the method of choice for large datasets (Taira et al., 2017).

Shannon entropy

Finally, the Shannon or global entropy of each decomposition is computed using Eq. 3.10. This parameter, which can vary between 0 and 1, can represent the energy distribution among different modes. H has its minimal value if all the energy is captured by the first mode and its maximal value if the eigenvalues are equal, meaning that the energy is uniformly distributed among the structures. The value of entropy can be indicative of the complexity of the flow (Aubry, 1991).

$$H = -\frac{1}{\ln(n)} \sum_{i=1}^n p_i \ln(p_i) \quad p_i = \frac{\lambda_i}{\text{tr}(\Lambda)} \quad (3.10)$$

p_i is the ratio between the eigenvalue and the global energy (i.e., the sum of the nonzero eigenvalues).

4

RESULTS

The results of the investigation of the flow within models of AAAs are presented and discussed in this chapter. First, the general flow behaviour is described by plotting the velocity fields. Then, to gain insight into the effect of aneurysm expansion on energy loss characteristics, viscous energy dissipation is calculated and compared between the cases. In the end, velocity-based POD is implemented to identify the flow field's coherent structures and demonstrate the flow complexity in each of the geometries. To easily identify the different cases tested throughout this chapter, each model is designated with a name and tagged with a sticker, summarized in [Tab. 4.1](#).

Table 4.1: Summary of the AAA model features.

Case	Description	Sagittal	Coronal
n.Ao	Normal Aorta, $D_{\text{nominal}}=2$ cm		
s.3A	Short Aneurysm, $D_{\text{max}}=4$ cm		
d3.3A	Axisymmetric Aneurysm, $D_{\text{max}}=3$ cm		
bi.3A	Bi-lobed Aneurysm, $D_{\text{max}}=4$ cm		
d4.3A	Asymmetric Aneurysm, $D_{\text{max}}=4$ cm		
d5.3A	Asymmetric Aneurysm, $D_{\text{max}}=5$ cm		

4.1 INSTANTANEOUS VELOCITY FIELDS

For the normal abdominal aorta (n.Ao), the experimental results are here provided to offer a baseline for the upcoming discussion on the flow behaviour in the presence of an aneurysm. As expected, during the acceleration phase, the flow follows almost the same pattern as a laminar attached flow. By mid-deceleration, the flow at the entrance (just distal to the origin of the renal arteries) slightly deviates from a unidirectional flow with random fluctuations at the inlet ([Fig. 4.1](#)). Overall, although a direct comparison with the literature is hindered due to the anatomical differences (e.g., exclusion of the visceral branches and the bifurcation), the findings are still in good accordance with the general description of the blood flow in the abdominal aorta.

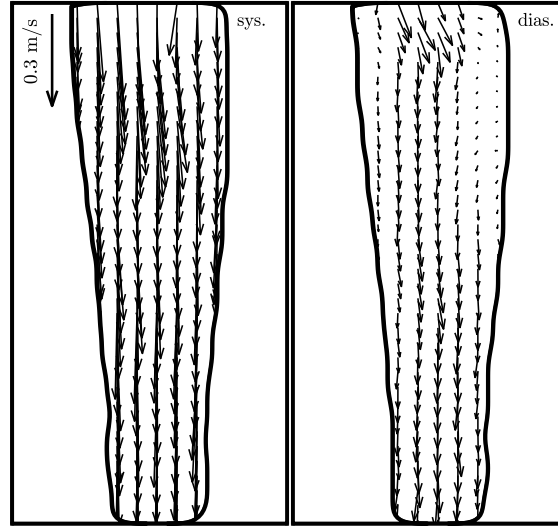


Figure 4.1: Healthy abdominal aortic flow. Left: peak systole. Right: mid-diastole.

Before proceeding with the bulge growth effect on the flow topology, we will discuss the typical flow field behaviour observed in the selected AAA models. Figures 4.1-4.4 show the coloured velocity vectors for 5 aneurysmal cases at selected time instants to highlight the essential features. Note that, for all vector fields, no colour bars are provided. Instead, the velocity magnitude is gradually decreasing from red to black. Regardless of their size or shape, a laminar flow dominates the AAA field during the acceleration phase for all investigated cases. Also, for the purposes of visualization, a median filter with a high threshold (5) is used with the universal outlier detection algorithm by [Westerweel and Scarano \(2005\)](#). After peak systole, the flow undergoes a temporal deceleration and loses momentum in response to the lumen's local enlargement. Therefore, to maintain mass conservation in an incompressible flow, such as what we have here, an unfavourable pressure gradient counterbalances the kinetic energy reduction. Therefore, a high-speed jet flow structure forms at the aneurysm's proximal neck, which is evident from the velocity field at the first snapshot. Since there is no angulation at the test section's inlet (i.e., the undilated abdominal aorta is straight), the jet penetrates the aneurysm sac. How far it overcomes the increasing pressure and propagates downstream depends on the inlet bulk velocity, the size of the aneurysm, and the wall properties. In the case of a compliant wall that expands during the acceleration phase, the increase in cross-sectional area is followed by a reduction in axial velocity that allows the jet to expand more radially. Nevertheless, the jet takes advantage of penetrating a fluid volume with low momentum to surpass the negative effect of the spatial deceleration and advect further downstream. Subsequently, the discontinuity of the jet boundary velocity generates a shear layer with a higher velocity on the side close to the wall. The shear layer rolls up and detaches and turns into a tight spiral shape. During the rolling-up process, the shear layer's consecutive turns gradually get closer with the closest neighbouring turns being at the spiral centre. The viscous diffusion smears out the tight spiraling structure into a vortex. The number, strength, and the trajectory of the vortices might be different for each geometry. For more localized aneurysms with a smaller width, if present, the vortices are less intense. The diastolic retraction of the wall releases the energy stored during the acceleration phase and drives the vortical structures downward. Depending on the geometry, the ring either breaks down into smaller vortices before it exits the aneurysm or comes in contact

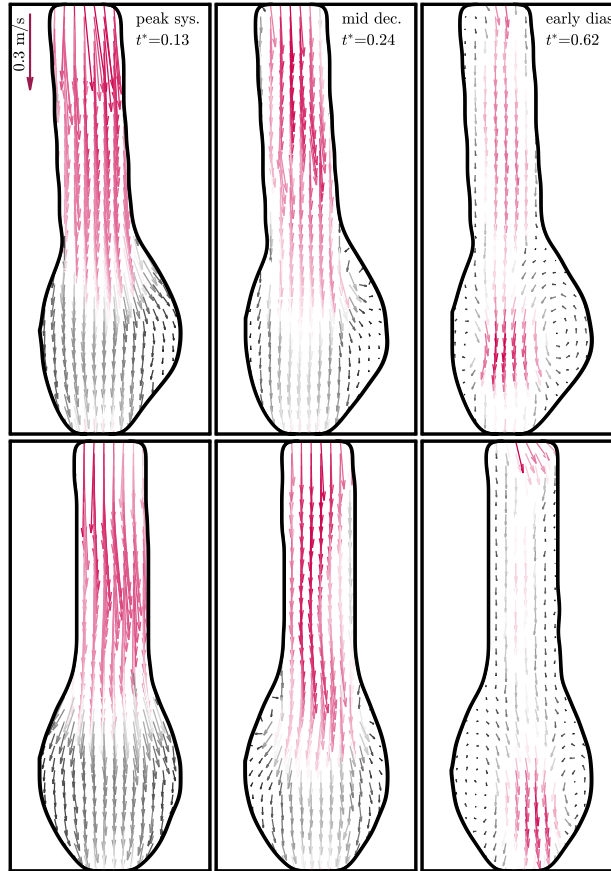


Figure 4.2: Flow in the model with a short aneurysm. Upper row: sagittal plane. Bottom row: coronal plane.

with the aneurysm distal end on the anterior wall and then breaks down. Either way, the vortex breakdown causes turbulence and the exact manner of breakdown is different from cycle to cycle, which leads to a fluctuating flow field. At the start of each cycle, there are residual vortices from the previous cycle that are interacting with the distal wall.

In the model with a longer neck and shorter aneurysm (s.3A), the flow remains attached to the wall during the systolic phase in both planes and starts to separate as it slows down, resulting in the formation of low strength vortices near the proximal neck. The vortices convect along the longitudinal axis while remaining close to the walls. Therefore, there is no sudden impingement, and the vortices gradually dissipate during diastole before they reach the convergent region at the exit. Even though the bulk flow rate is zero in the remaining duration of the cycle, the flow is characterized by regions of nearly stagnant flow with very low velocity along the walls. The representative instants of the velocity vector field associated with this case is shown in Fig. 4.2.

For the case with symmetric walls and the least value of maximal diameter (d3.3A), the flow behaves almost identical to the flow in the healthy abdominal aorta with a non-disturbed flow and no sign of aortic wall impingement, recirculation or turbulence. The vector field is therefore not shown to avoid redundancy.

For the aneurysm with the second-largest maximal diameter (d4.3A), After the peak flow jet is formed, it starts to separate and roll up from the anterior wall around the inflection point. A large

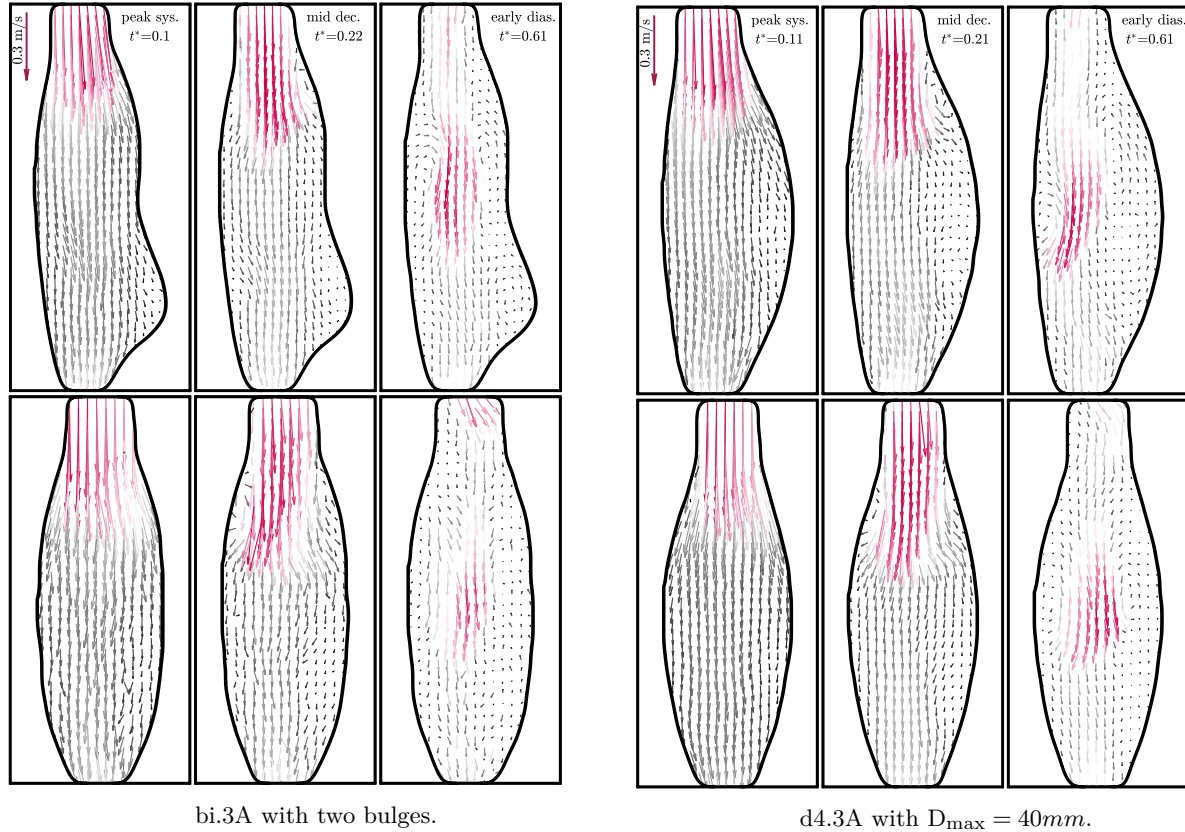


Figure 4.3: Velocity vectors in the fusiform and bi-lobed aneurysms. Upper row: sagittal plane. Bottom row: coronal plane.

region of recirculating flow with low velocity near the bulge pushes the jet to the opposite side until it impacts the distal posterior wall and generates shear along the wall for the rest of the cycle.

For the model with the largest maximal diameter (d5.3A), the flow field goes through a more complex evolution, although it still exhibits standard AAA flow features. As is evident from Fig. 4.4, the peak systolic velocity field concerns a laminar flow with the formation of a high-momentum coherent jet structure at the core. The onset of deceleration instigates the formation of a pair of counter-rotating vortices on both sides of the jet at the throat. In the coronal plane with symmetric walls, when the so-called vortex ring is developed, it travels downstream and moves away from the wall following a relatively straight line. The vortex ring has traversed the centre of the aneurysm sac by early diastole, while a low-velocity recirculating zone is developed in the proximal anterior bulge. However, as it gets closer to the bifurcation, the left vortex approaches and impinges on the adjacent lateral wall resulting in disturbances that dissipate by the end of the pulse.

In the sagittal plane, the same flow pattern is observed at the peak. During the vortex formation process, the loss of symmetry causes the vortex emerging near the anterior wall to become stronger and span a greater area. The vortical structures propagate downstream with almost the same speed as their counterparts in the frontal plane. As they move further, their pathlines curve toward the anterior wall leaving an enlarged recirculation zone at the upstream and in the vicinity of the posterior wall where most AAA ruptures occur (Darling et al., 1977). Up to the end of the cycle, the velocities no longer vary, and the second vortex remains intact. With regard to the initial

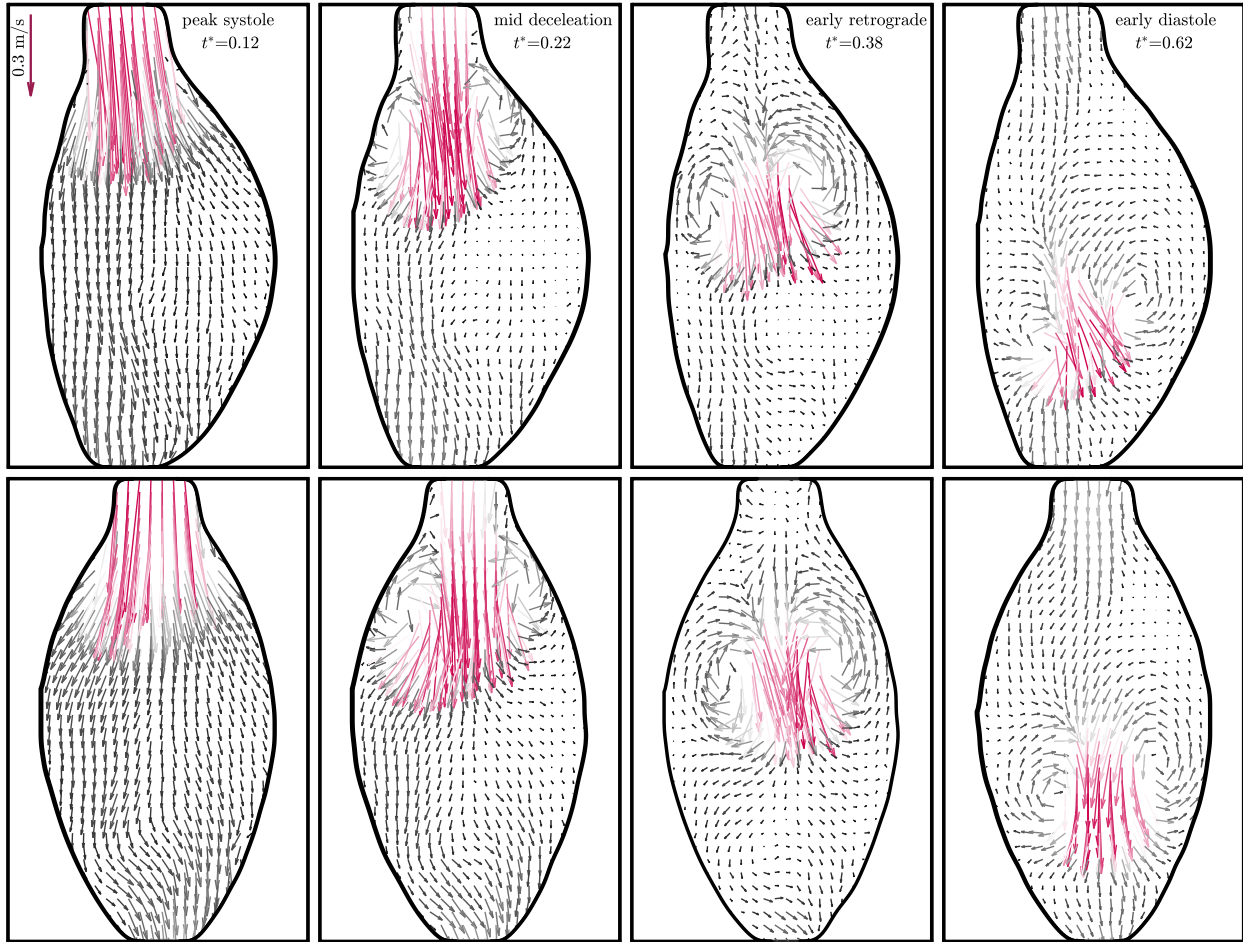


Figure 4.4: Velocity vectors in the most severe case (d5.3A). Upper row: sagittal plane. Bottom row: coronal plane.

observation of residual vortices fluctuating near the distal end of the AAA at the beginning of the cycle, one can infer that the second vortex from the previous cycle has ultimately collapsed while leaving the aneurysm.

4.2 ENERGY LOSS ANALYSIS

As discussed in [Ch. 1](#), AAA initiation and progression are complex, non-linear, and correlated with changes in the wall structure and blood flow topology. Therefore it is unsafe to make a prognosis and evaluate the associated risks only based on a 1D local parameter related to the geometry (i.e., maximal diameter). Other proposed indices related to the morphology and the wall thickness have never been considered in standard guidelines for AAA management ([Shum et al., 2011](#); [Wanhainen et al., 2019](#)). From a fluid dynamic point of view, low WSS and high OSI have been recommended as indicators of sites susceptible to expand and burst. However, there have been controversies on their correlation with aneurysm growth that made them inapplicable for real patient treatment ([Lozowy, 2017](#)).

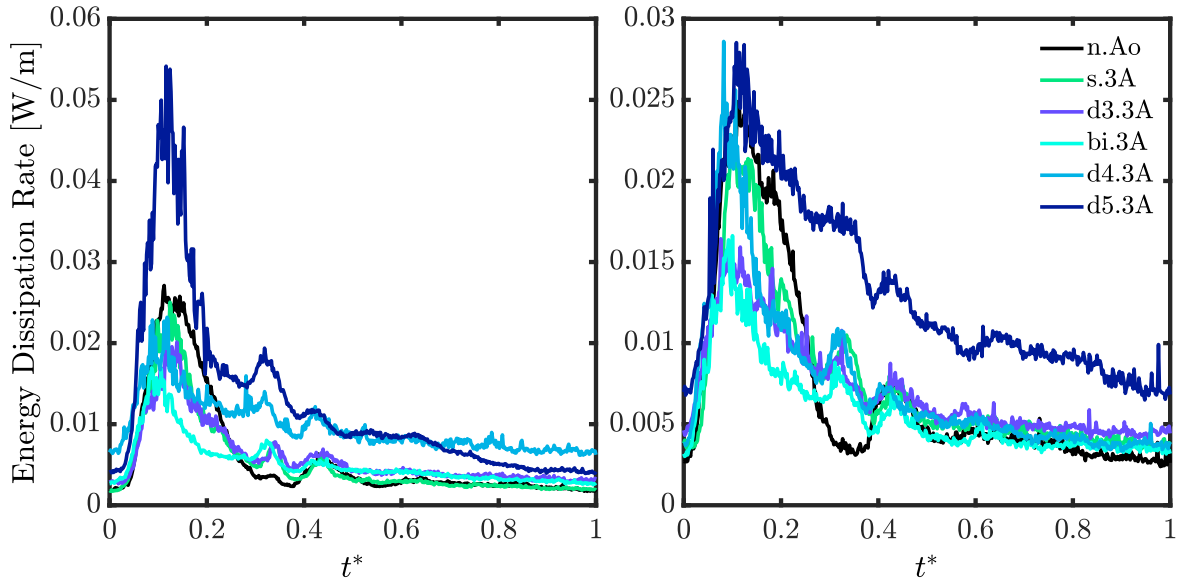


Figure 4.5: Viscous energy dissipation rate. Left: sagittal plane. Right: coronal plane. (The non-dimensionalized time, $t^* = \frac{t}{T}$, is defined such that $t^* = 0$ and $t^* = 1$ correspond to the beginning of systole and end of systole, respectively.)

In this section, energy loss is examined and compared through $VEDr$ or the rate at which the energy is dissipated via viscous stresses in the flow field. In blood flow with vortical motion and perturbations, $VEDr$ is a measure of how kinetic energy in a cycle is wasted due to the viscosity, and the extra work should be done by the heart to overcome the loss and maintain regular circulation. Here, the hypothesis is that the value of energy loss is higher for the cases with a larger diameter, a more complex geometry, and higher flow disturbances. The temporal evolution of the viscous energy dissipation rate corresponding to the six cases investigated in both planes is plotted in Fig. 4.5. As expected, the viscous stresses lead to a higher rate of energy loss during systole characterized by the jet structure and vortex formation with subsequent mild fluctuations and notably higher strain rates. As is evident, the instantaneous rate of viscous dissipation is distinctly higher for d5.3A in both planes. Even though wall impingement and breakdown cause some random fluctuations during diastole, the energy loss is negligible due to the almost zero velocity of the bulk flow.

The total energy loss calculated by integrating the instantaneous $VEDr$ per unit depth over the entire cycle is portrayed in Fig. 4.6. With its highly disturbed flow, the most dilated aneurysm is the most severe case regarding energy loss concerns. In the sagittal plane, except for the cases with a maximal diameter of 4 cm (d4.3A) and 5 cm (d5.3A) wherein we observed asymmetric flow separation and mural impact, the kinetic energy in the other geometries is relatively well-preserved. The same pattern is observed in the coronal plane except for the lower value of energy loss for d4.3A compared to its corresponding value in the sagittal plane where the anterior wall is expanded more, and shear stresses are higher due to flow detachment. Comparing the total energy loss for the first four models from n.Ao to bi.3A indicates that although the wall dilation is getting worse and the maximum diameter increases, the kinetic energy is preserved almost equally with minimal energy loss due to the viscous forces. One way to justify this similarity is to refer to the less intricate flow

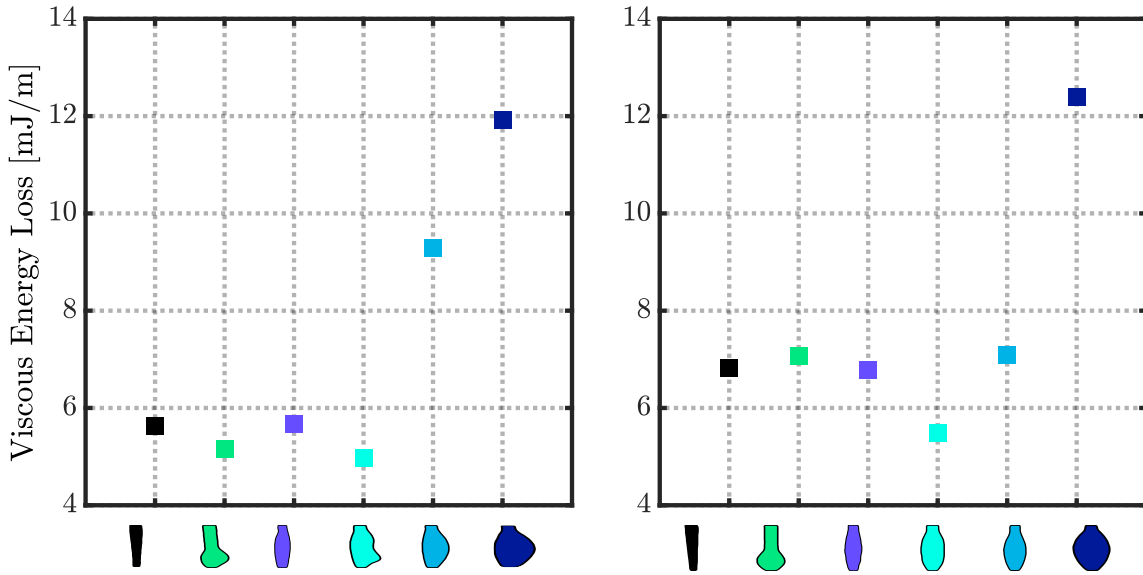


Figure 4.6: Total viscous energy loss for all the cases. Left: sagittal plane. Right: coronal plane.

patterns in these models, which implies that more complexity in the geometry is not necessarily followed by a noticeable increase in viscous energy dissipation.

4.2.1 Statistical analysis

To quantify whether the gradual enlargement in the average size of the AAA models in this study leads to a significant variation in total energy loss, statistical analysis is performed using one-way ANOVA.¹ The analysis of variance (ANOVA) technique uses a p -value to evaluate a null hypothesis that if a set of group means (e.g., mean value of total energy loss in all the case studies, each with 4 rounds of realization) are equal. Note that, targeting a confidence level of 95%, a p -value of less than 0.05 would reject the null hypothesis and indicate that the changes in the mean of the variable of interest are statistically significant. Higher values of p suggest that the means are not statistically different. Here, the small corresponding p -values (<0.005) indicate that the difference in the total viscous energy loss across cases with different sizes is significant. This result, however, does not provide further information on which cases are different. Therefore, multiple pairwise comparisons are performed between every two groups. The resulting p -values are summarized in Tab. 4.2, which confirm the earlier discussion that while there is a lack of statistical difference between the amount of energy loss in smaller models, there is a statistical distinction (minimal p -value) between the two larger aneurysms and the rest of the models.

In healthcare applications, viscous energy loss quantification is possible using patient-specific *in vivo* velocity data. Therefore, clinicians can gain insight into the disease severity from a fluid dynamic perspective, potentially reducing uncertainties in decision-making that stems from the standard metric (i.e., maximal diameter).

¹ MATLAB built-in function.

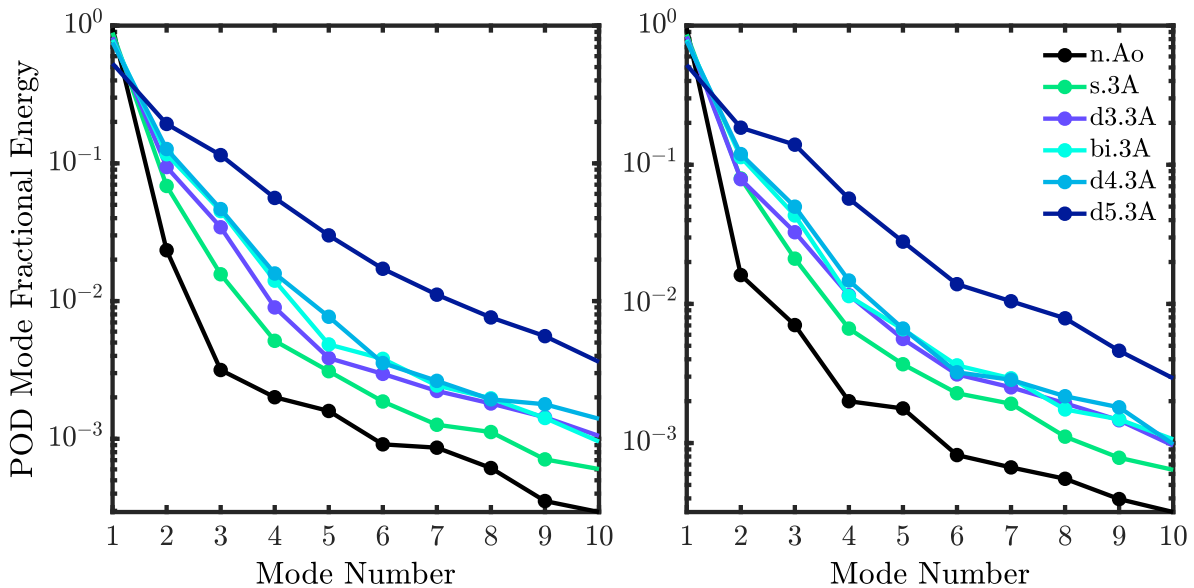
Table 4.2: One-way ANOVA results for total energy loss as the variable of interest.

Case	Sagittal plane					Coronal plane				
	s.3A	d3.3A	bi.3A	d4.3A	d5.3A	s.3A	d3.3A	bi.3A	d4.3A	d5.3A
n.Ao	0.696	0.851	0.970	0.011	<0.005	0.659	0.927	1	0.003	<0.005
s.3A		0.145	0.981	0.190	<0.005		0.186	0.530	0.069	<0.005
d3.3A			0.420	<0.005	<0.005			0.975	0.005	<0.005
bi.3A				0.054	<0.005				0.002	<0.005
d4.3A					0.017					0.020

4.3 MODAL DECOMPOSITION

Earlier in this chapter, the principle flow characteristics in AAA models were qualitatively described by looking at the velocity vector fields at selected instants during the cycle. However, suppose the flow pattern inspection is to serve as a tool in diagnosing and managing diseases such as AAAs. In that case, it is much more enlightening if, in each case, we search for structures that evolve coherently (i.e., regions of highly correlated velocity and synced displacement). This goal cannot be accomplished without comparing all snapshots. Modal decomposition and, in particular POD, can be employed to extract the key energetic structures of AAA flow in each configuration from visual inspection of the distribution of the primary modes. For this purpose, snapshot POD is performed using a data matrix compiled from 500 snapshots of the velocity field, and the deterministic modes are provided along with their eigenvalues and temporal coefficients.

To begin with the POD analysis, the fractional energy content in terms of the eigenvalue spectrum up to the first 10 POD modes of all the probed cases in two planes of measurements is presented in Fig. 4.7. As one would expect from POD intuition, the energy is dominantly held by the first mode

**Figure 4.7:** The energy spectra for the first 10 POD modes. Left: sagittal plane. Right: coronal plane.

with the highest values found for the normal case (95.81% and 95.77% in the sagittal and coronal planes, respectively). Cardiovascular blood flow is a superposition of a mean component with an oscillating pulse profile. As discussed in the methodology, when the temporal mean-subtraction is not applied to the POD algorithm, the first mode resembles the time-averaged velocity field, which, in the case of a non-aneurysmal aorta, is identified with a dominating laminar flow. The process of time-averaging removes time-dependent flow features such as vortices and provides an overall representation of the flow dynamics that occur during a pulse. The time-averaged velocity field gives an overall description of the flow, but it does not capture the instantaneous dynamics and distinct features such as vortex motion. Temporally speaking, the first POD mode undergoes the same evolution curve as the imposed flow waveform. The subsequent primary modes, although contributing less to the total energy (e.g., 2.34% for the second mode for the simplest model), still reveal information about the dominant energetic structures that exist in the flow.

To complement the premise about the energy distribution, Fig. 4.8 portrays the spatial structure associated with the first and the second POD modes for the normal case. The diastolic flow reversal can be partially observed from the second mode in the normal case. Overall, if the idea is to reconstruct the flow using POD modes, the first two modes would be sufficient regarding the trivial contribution of the remaining ones to the system energetically and physically. Evidently, the number of essential modes to preserve the key features and minimize the discrepancy between the low-dimensional representation and the actual field vary depending on the nature of the flow. Note that, due to the similarities of the extracted POD modes and the coefficients, the coronal plane results are not included in this case.

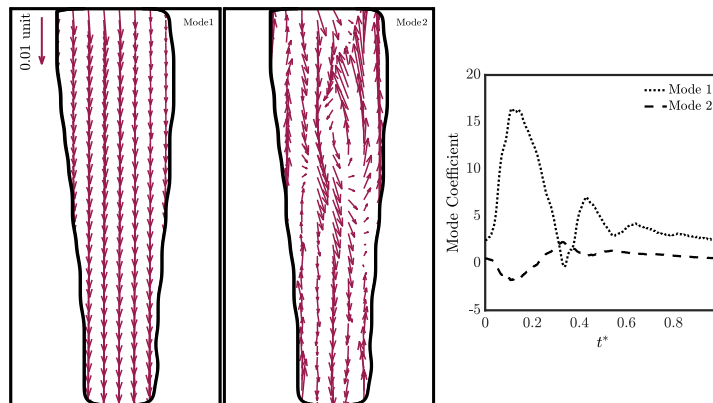


Figure 4.8: The first and the second POD mode and the corresponding temporal coefficients for n.Ao in the sagittal plane. The scale for the spatial distribution of the POD modes in all the related figures is accompanied by "unit" since the modes are normalized and do not have unit.

Applying POD on the dataset related to the incipient aneurysm (d3.3A) provides almost the same information as the normal case (see Fig. 4.9), which sounds logical due to the similarities of their flow fields. As the abnormalities such as detachment, shear layer roll-up, and vortex formation appear in the flow pattern, the number of modes required to preserve a desirable percentage of kinetic energy goes up while the initial modes are still playing the pivotal role.

The distribution of the first two spatial modes and their coefficients pertaining to s.3A is illustrated in Fig. 4.10. In the sagittal plane, the vortex emerging at the anterior wall's proximal neck during the deceleration phase is extracted by the second mode. However, with regard to the reconstructed model using only two modes, the vortex core does not move and remains in its primary location.

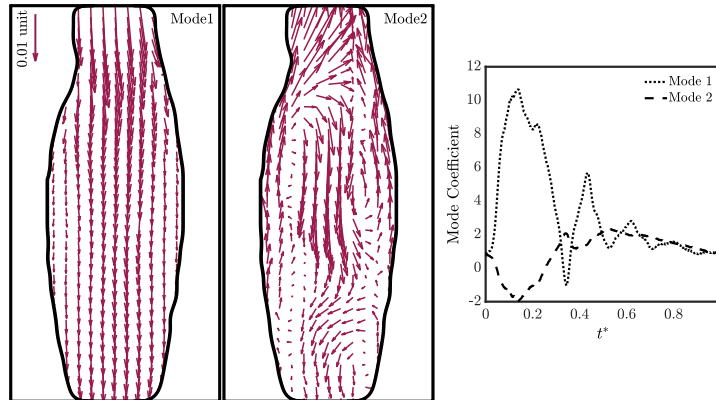


Figure 4.9: The first and the second POD mode and the corresponding temporal coefficients for d3.3A for the sagittal plane.

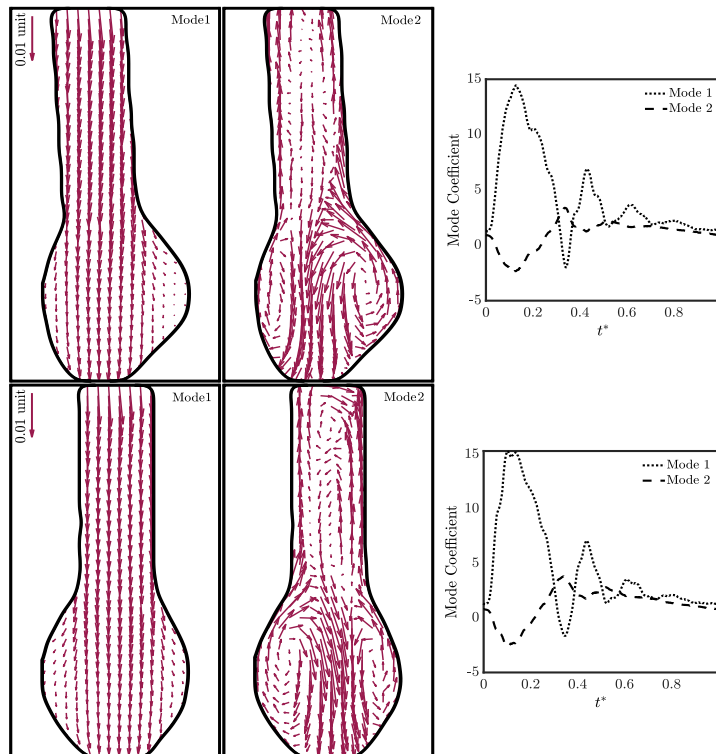


Figure 4.10: The first and the second POD mode and the corresponding temporal coefficients for s.3A. Upper row: sagittal plane. Bottom row: coronal plane.

Adding the third mode can slightly help capture the vortex evolution. However, due to the missing structures such as the smaller vortex on the opposite side near the posterior wall, the reconstructed flow field still deviates from the original one. Therefore, to model all the essential processes, extra modes are needed owing to an increase in the system's complexity.

For bi.3A with 2 bulges and d4.3A with the second-largest maximum diameter, reduction in the cumulative energy content using three modes indicates that the energy is redistributed to higher POD modes and again more than three modes are required to represent the entire system. This is consistent with the observations made from the truncated model including three modes, in which some features of the actual flow are missing. The POD decomposition information for these two cases can be found in Fig. 4.11 and Fig. 4.12.

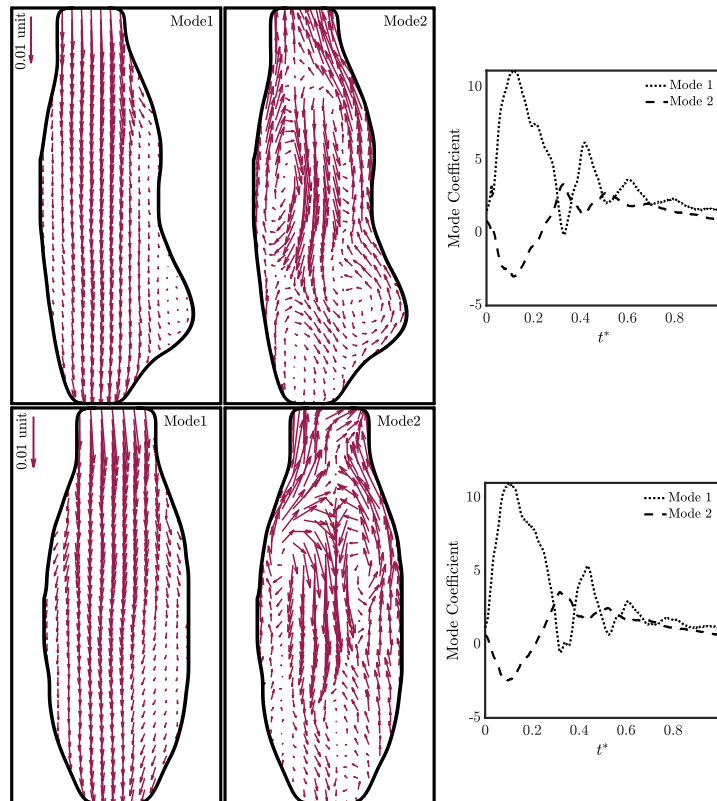


Figure 4.11: The first and the second POD mode and the corresponding temporal coefficients for bi.3A. Upper row: sagittal plane. Bottom row: coronal plane.

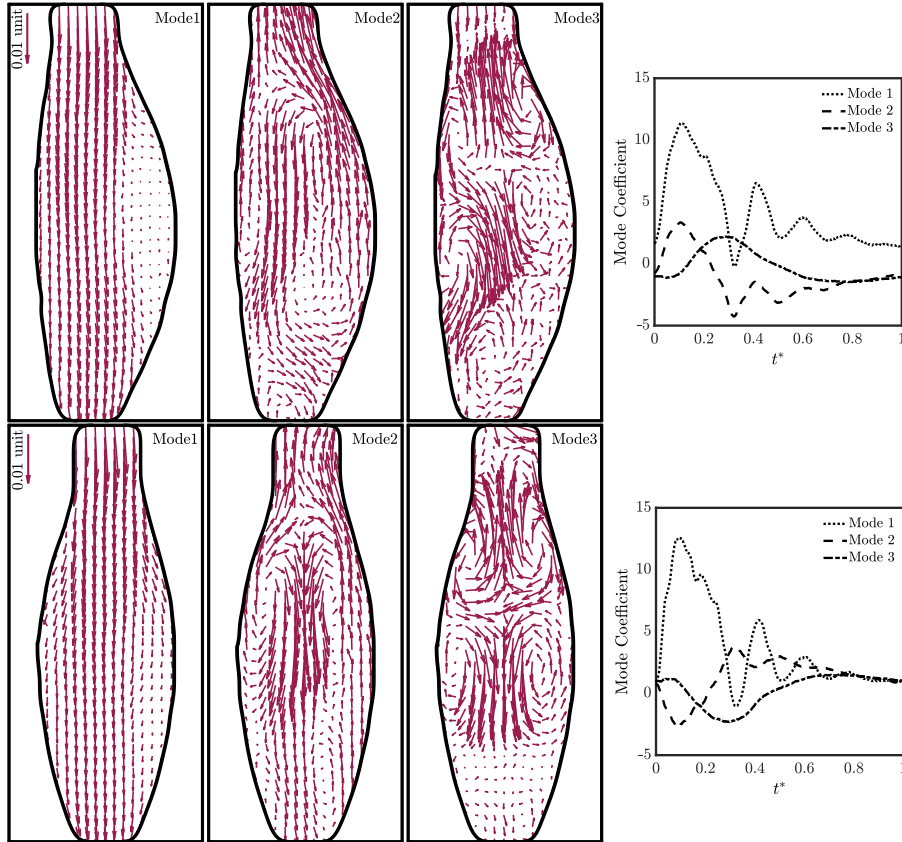


Figure 4.12: Spatial distribution of the first 3 POD modes for d4.3A. Upper row: sagittal plane. Bottom row: coronal plane.

Flow in the largest aneurysm is the most delicate case to look at using modal decomposition (see Fig. 4.13). From the POD energy hierarchy, the first two modes contain a much lower fractional energy, meaning that more modes are important to the energetic dynamics of the system (i.e., 7 modes are required to capture 95% of the energy). The first mode delineates a channeled flow along the centre surrounded by structures of lower magnitude near the walls. The second mode is likely to capture similar processes as the other cases with the bulge, namely, the jet emergence and the shear layer roll-up. The third mode can be divided into two segments. The lower part correlates with further penetration of the jet. The upper part encapsulates regions of separated vortical structures that originated in the second mode. The fourth mode, based on the truncated model, contributes to the evolution of structures extracted from the third mode with an additional middle segment, referred to as the recirculating region formed near the anterior wall. In the lateral plane, there is a sudden decline in energy fraction starting from the fourth mode, which regardless of its lower energy, is shown to improve the low-dimensional approximation of the system in a meaningful way by adding the further progression of the jet towards the distal end of the left wall.

In order to gain an insight into the distribution of the energy among different modes, which would therefore give us an idea about the degree of flow complexity, global (Shannon) entropy proposed by Aubry et al. (1991) can be used as an indicator. Higher values imply a more homogeneous contribution of different POD modes in capturing the energy. Here, the Shannon entropy is found to follow a positive trend as the bulge is expanding longitudinally or transversely.

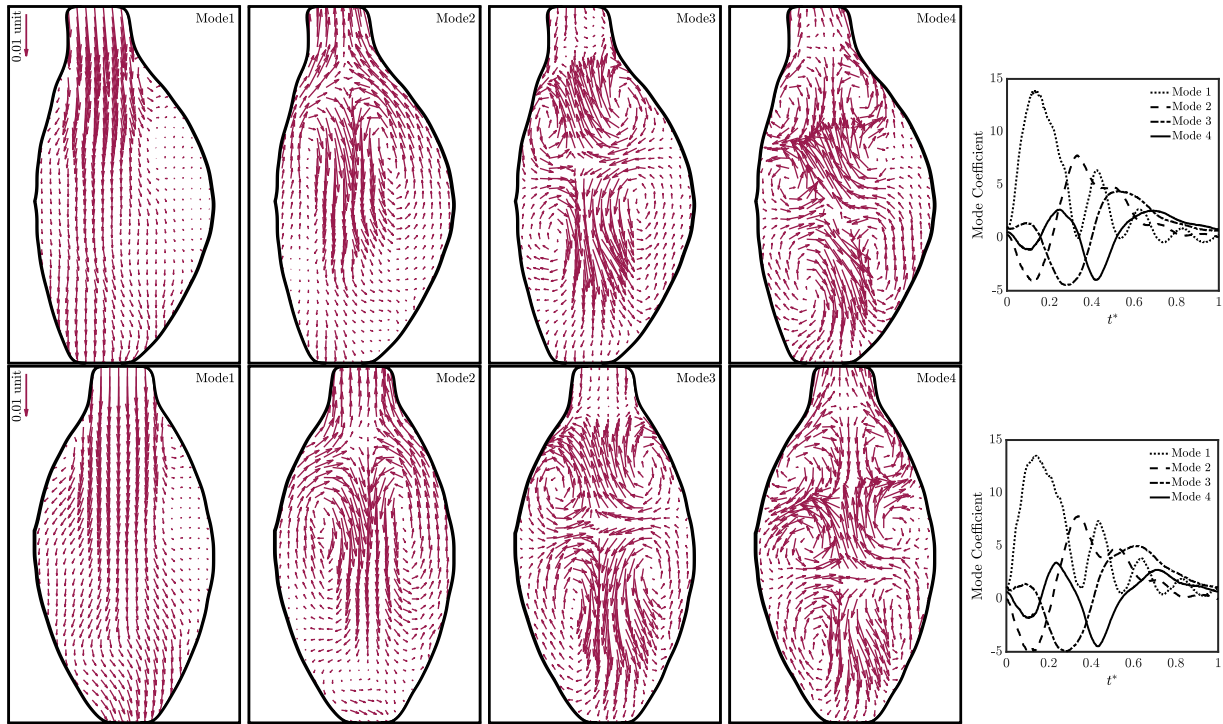


Figure 4.13: Spatial distribution and temporal coefficients of the first 4 POD modes for d5.3A. Upper row: sagittal plane. Bottom row: coronal plane.

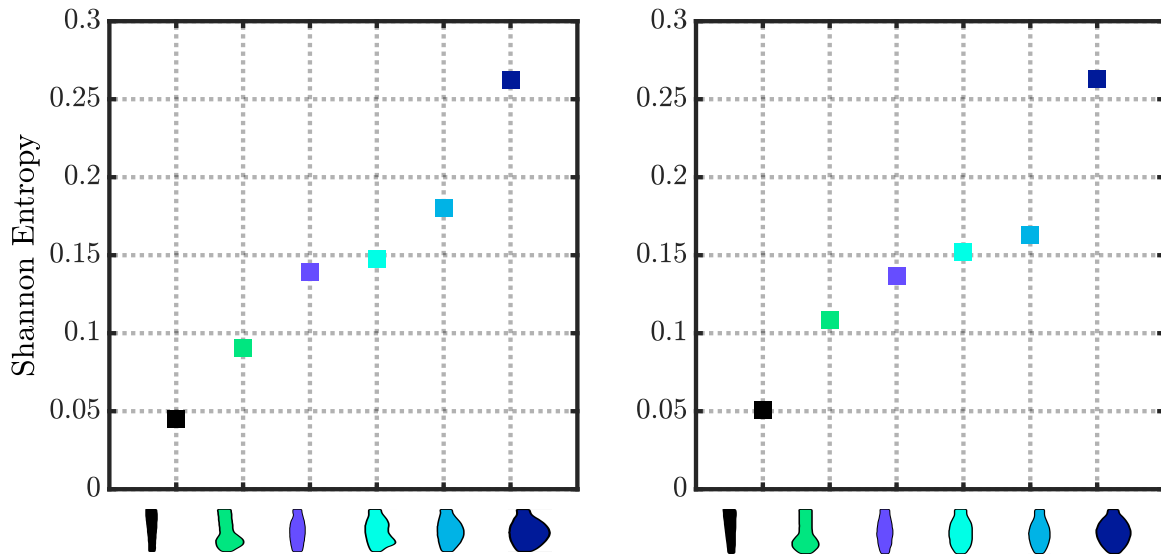


Figure 4.14: Global entropy for all the cases. Left: sagittal plane. Right: coronal plane.

As is observed in Fig. 4.14, the highest value is attributed to the most dilated case (d5.3A) with a higher dispersion of modal energy content whose first mode accounts only for 53% of the accumulated energy contrary to the healthy aorta with the least value of entropy wherein the first mode itself captures nearly 96% of the kinetic energy. This is in agreement with the velocity fields discussed in Sec. 4.1 since the larger aneurysm went through a considerably sophisticated evolution compared to the normal case, which exhibited a laminar and undisturbed behaviour over the entire cardiac cycle. The entropy value for this case is even remarkably higher compared to the previous case (d4.3A), with a far less complex flow structure, which again supports the great impact of the flow behaviour on modal energy distribution.

Since POD only considers energy to rank the modes regardless of their dynamically-relevant frequencies, resulting modes share frequency content while higher frequencies are more dominant in noisier modes ranked lower in terms of energy. However, these modes may capture small-scale, albeit essential features of the system that might also be found in the primary modes with higher energy levels and less noise. This unpleasant frequency mixing is depicted in Fig. 4.15 through characterization of the intensity of the amplitudes of the first four modes in the frequency domain, obtained for the normal case (n.Ao) and the most severe case (d5.3A). Including similar frequencies forms the hypothesis that different modes can capture similar processes, which can be verified by examining the mode shapes.

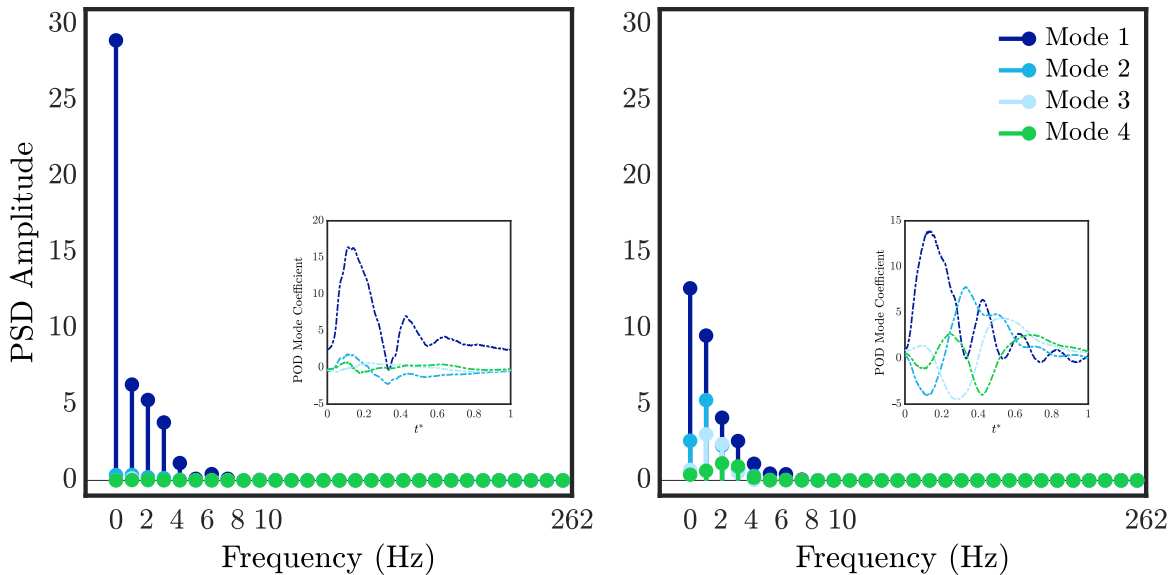


Figure 4.15: Power spectral density for POD modes of n.Ao and d5.3A in the sagittal plane. The vertical axis, power spectral density (PSD), demonstrates the intensity of the variations as a function of frequency.

4.3.1 Data reduction with POD

In the context of model reduction, instead of using a large number of grid points to represent the flow field, POD can be used to reconstruct the variables of interest from an optimal set of modes that

account for a given amount of cumulative energy with the least relative error. The reconstruction is done by projecting the POD modes onto the snapshot basis using the matrix of POD mode weights as the transformation matrix with the temporal dynamics in its rows and the essential coefficients for the reconstruction in its columns (Di Labbio and Kadem, 2019).

Table 4.3: Required number of modes for the reconstruction based on the percentage of kinetic energy to preserve.

KE	Sagittal plane				Coronal plane			
	95%	98%	99%	99.9%	95%	98%	99%	99.9%
n.Ao	1	2	7	268	1	3	26	345
s.3A	2	4	19	353	3	7	53	385
d3.3A	3	25	117	422	4	23	110	419
bi.3A	3	10	61	406	4	18	99	417
d4.3A	5	53	165	441	4	27	132	427
d5.3A	7	16	62	401	7	17	102	425

The convergence of the POD modes can be tested using the \mathcal{L}_2 norm of the normalized eigenvalue spectrum. Suppose we are seeking a reduced-order representation of the velocity. In that case, kinetic energy is regarded as a standard of POD mode truncation. The required number of modes would be minimal compared to using higher-order flow characteristics such as viscous energy dissipation as the target of low-dimensional modelling.

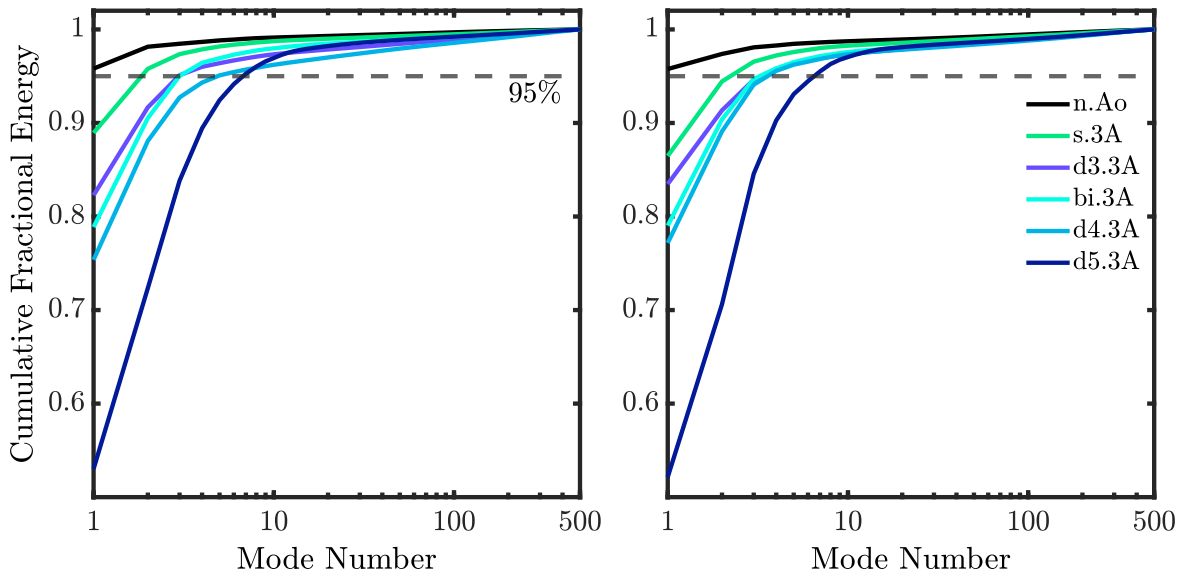


Figure 4.16: Accumulated fraction of total kinetic energy as function of the number of modes. Left: sagittal plane. Right: coronal plane.

The number of modes required to capture 95%, 98%, 99% and 99.9% of the total kinetic energy is summarized in Tab. 4.3. Also, from Fig. 4.16, we can notice a rapid convergence for all the cases if

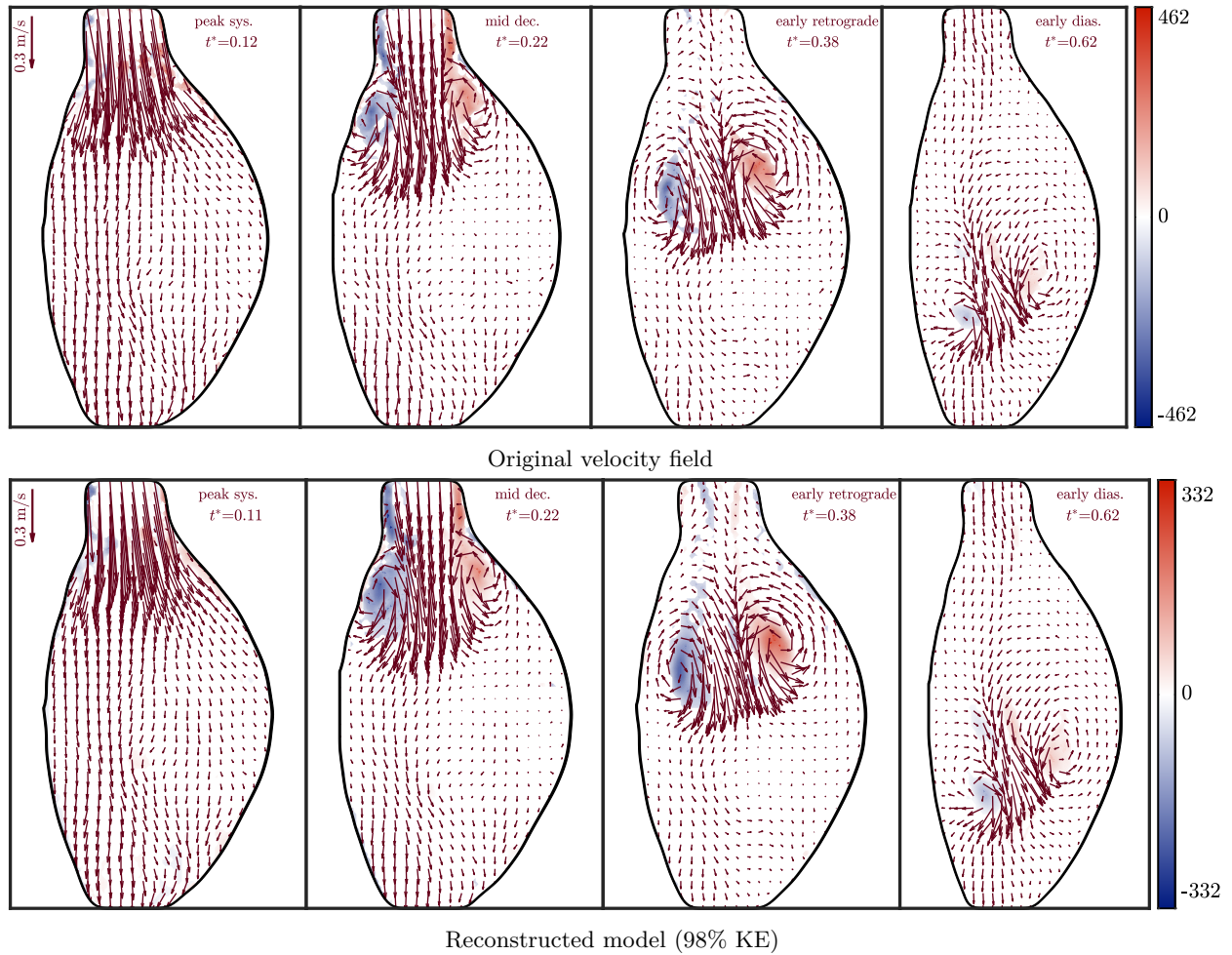


Figure 4.17: Velocity vector field at 4 snapshots for d5.3A and its truncated model with 98% KE. The vortex ring core trajectory is identified through vorticity contour maps.

retaining 95% of the kinetic energy is set as the target. That is to say, a significant data reduction in the dataset can be obtained to represent the flow using only a few primary modes with the highest value for the most severe case (d5.3A). As we observed in Fig. 4.7, this case had the more disperse POD energy spectrum. If we increase the threshold of KE, a greater number of modes with a higher rank and insignificant energy level have to be added to the low-dimensional model to faithfully represent the original flow field with the specified energy content. Note that, after a certain level (i.e., 95% of KE), the required number of modes is not necessarily increasing with the flow complexity. This is due to the dominant structures that characterize the important flow features in each aneurysm model which are hidden in the low-rank, energetic modes. By contrast, the additional higher-rank POD modes included in the reconstruction to satisfy a more strict energy criterion (i.e., 99% of KE), are not playing any role in representing the flow structure.

The qualitative comparison between the reconstructed field using 18 POD modes (for 98% of the KE) and the actual flow field can be made by plotting velocity distributions at particular time instances. The sample result is provided only for d5.3A (Fig. 4.17b). As we can see, the velocity and vortex location in the corresponding snapshots are quite well reconstructed. Note that the reconstructed field seems to be smoother than the velocity field from PIV, which is one of the

consequences of using POD. Therefore, the magnitude of the vorticity is lower in the truncated model.

To further evaluate the truncated model's performance, the deviation between the approximated value for the total energy loss from the reference value has been quantified and presented in Fig. 4.18. As one can notice, reconstruction of the flow field (unless up to 99.9% of the kinetic energy) does not faithfully model the viscous energy dissipation and, in turn, leads to an underestimation.

In fact, by defining the cut-off mode in an energy-wise manner, only the most energetic structures and fluctuations are considered. From a physical point of view, however, by limiting the number of modes included in the reconstruction, the desired information from higher-order snapshots with lower energy levels may be unintentionally discarded, particularly in a fluid flow system with dissipation or cyclic fluctuations like what we deal with in this work.

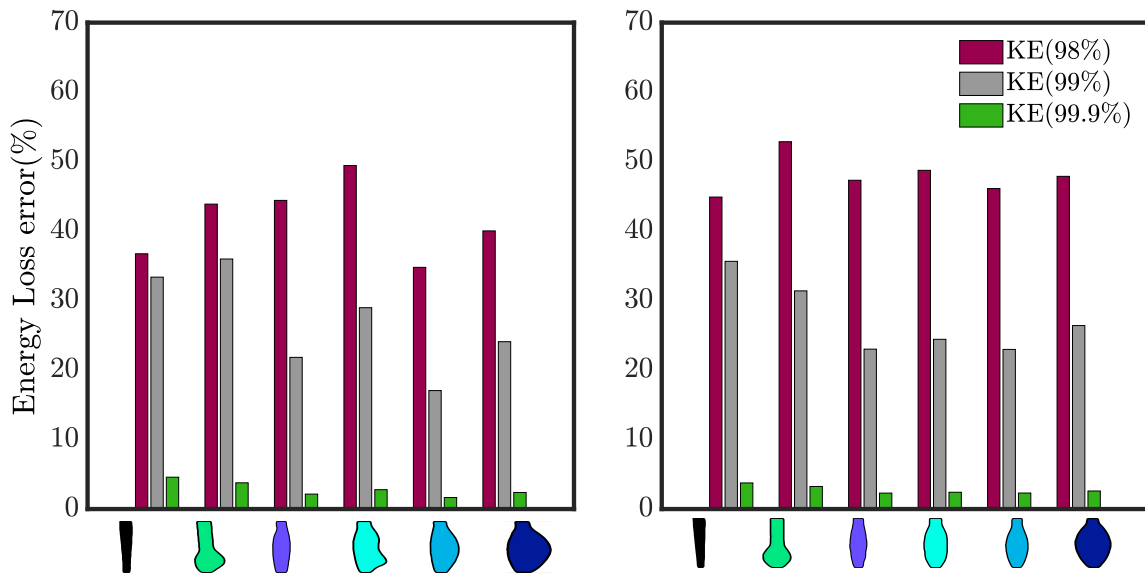


Figure 4.18: Performance of the truncated model to capture 98%, 99%, and 99.9% in modelling energy loss.

One way to fix this problem might be to exclude some primary modes with clearly insignificant information irrespective of their contribution to the energy and instead include POD modes that contain the desired information, but this ignores the purpose of POD to extract modes in an energy-optimal way. Also, if spurious vectors with large velocity magnitude had not been detected and replaced, the reconstructed model may be prone to corruption by including high but erroneous energy values.

5 | CONCLUSION

This chapter presents a summary of the thesis outcomes followed by recommendations for further investigation to build up on the current work.

This experimental project was initially conducted to explore the flow dynamics in a range of AAA models at different progression stages. The primary contribution is the design and development of an *in vitro* setup that accommodates a replica of the abdominal aortic aneurysm of any shape and faithfully simulates the physiological flow. It is worth recalling that as described in the methodology, a novel approach was employed for moulding transparent phantoms of AAAs that are made with less effort, at a lower cost while being eco-friendly and compatible with PIV.

The observations of instantaneous flow fields in two planes of measurement indicate that the flow in an incipient aneurysm with axisymmetric geometry still resembles the normal abdominal aortic flow. Further enlargement in the cross-sectional area was accompanied by the onset of features such as flow separation, vortex formation and occasionally wall impingement, which were remarkably more intense in the largest case with a maximal diameter of 5 cm. This perception can provide a physical proof to the deterministic threshold of 5 cm for the maximal diameter to proceed with clinical intervention. We hypothesize that the development and propagation of large vortical structures and the formation of recirculating regions near the largest AAA model's proximal neck compared to other investigated AAAs can result in an adverse hemodynamic effect that exacerbates the dilation and increases the risk of rupture.

The acquisition of the velocity vectors with time-resolved PIV in this work can serve as a means of validation for numerical studies of AAA flow. Needless to say, validation of FSI numerical simulations is an inevitable step before they can be clinically applicable for the purposes of patient-specific diagnosis and treatment.

Possible association of viscous dissipation with serial growth of AAAs was another hypothesis of this study. However, we found that this parameter is not necessarily increasing with aneurysm expansion. Again, the largest model was identified with the highest amount of viscous energy loss, followed by the second-largest case, which can be attributed to the higher shear values. The other four models exhibited an almost identically efficient behaviour in preserving the kinetic energy.

The current thesis is also the first to apply proper orthogonal decomposition to experimental AAA flow data to explore low dimensional flow patterns using the spatial distribution of the primary POD modes that can be further exploited for efficient reduced-order and data-driven modelling. Proper orthogonal decomposition analysis indicates that the dominant modes can represent the important features of the flow from an energetic perspective. The number of modes required for this purpose is greatly affected by the complexity of the flow field in the aneurysm. In addition, the value of Shannon entropy confirms that as the aneurysm expands, the modal energy spectra is distributed more dispersedly, and a higher number of modes are required to reconstruct the high dimensional flow system while for the normal abdominal aorta, a single mode would be sufficient to capture about 96% of the energy.

5.1 RECOMMENDATIONS

The present work can be further extended in future work with the following ideas:

- Regarding the complex flow dynamics in the abdominal aortic aneurysm, to expand our understanding of the underlying physics, it could be interesting to perform 3D measurements in the whole AAA volume using tomographic PIV.
- The results associated with the bi-lobed aneurysm (i.e., with 2 bulges) denotes a channeled flow with minor interaction with the wall, which was not expected prior to the measurements. Therefore, it is suggested to consider models with multiple bulges with various sizes to explicitly explore the effect of this factor on flow patterns and implications.
- In essence, it is difficult to predict the potential risk of rupture for abdominal aortic aneurysms, and numerous uncertain strategies might be taken to manage the disease around the world. This inconsistency emphasizes the need for a global patient-specific predictive approach that considers the AAA size, morphology and general patient information. Application of machine learning in healthcare has helped accomplish this goal by analyzing large datasets of patients to identify patterns between parameters that may be predictive of a patient's prognosis, AAA growth and rupture. For instance, in a successfully tested program in three clinical cases, eight biomechanical factors were integrated to calculate a patient-specific severity parameter that classified the patient status as low risk, observation, elective repair, or imminent rupture (Kleinstreuer and Li, 2006). Accordingly, the current thesis can be extended by incorporating systematic variations in morphological and geometrical parameters to generate a large dataset that can be fed into a POD algorithm and compressed into an appended reduced-order library of a limited number of dominant modes that represent the system's dynamics (i.e., the library can be considered as a supervised machine learning step). Therefore, the truncated modal information can be used to identify active modes using compressed sensing, which can be later utilized for reconstructing high-resolution data from low-resolution sampling. It can, in turn, assist clinicians with a better interpretation of *in vivo* data and the identification of parameters that are of great interest in personalized medicine. Also, the Shannon entropy might be considered as a new metric for severity classification.
- It is worth mentioning that the optimality of POD (i.e., least residual error in capturing energy for a given number of modes) is not priceless. The decomposition can end up mixing processes of multiple frequencies, which is recurrently observed in complex flows. Therefore, it is challenging to interpret the modes physically and identify the coherent structures accordingly. It becomes more problematic when the goal is to reconstruct a low-dimensional model of an otherwise high-dimensional system wherein the deterministic modes are not easily discerned. To address this issue, it is recommended to elaborate the modal analysis of this project's available data by applying the frequency domain form of POD, namely, spectral proper orthogonal decomposition (SPOD), which delivers modes that evolve coherently in space and time being well-suited for identifying physically meaningful structures (Towne et al., 2017).

BIBLIOGRAPHY

- Adrian, L., Adrian, R. J., and Westerweel, J. (2011). *Particle image velocimetry*. Number 30. Cambridge university press.
- Aggarwal, S., Qamar, A., Sharma, V., and Sharma, A. (2011). Abdominal aortic aneurysm: A comprehensive review. *Experimental & Clinical Cardiology*, 16(1):11.
- Akins, C. W., Travis, B., and Yoganathan, A. P. (2008). Energy loss for evaluating heart valve performance. *The Journal of thoracic and cardiovascular surgery*, 136(4):820–833.
- Antón, R., Chen, C.-Y., Hung, M.-Y., Finol, E. A., and Pekkan, K. (2015). Experimental and computational investigation of the patient-specific abdominal aortic aneurysm pressure field. *Computer methods in biomechanics and biomedical engineering*, 18(9):981–992.
- Arzani, A. (2016). *Hemodynamics and Transport in Patient-specific Abdominal Aortic Aneurysms*. PhD thesis, UC Berkeley.
- Asbury, C. L., Ruberti, J. W., Bluth, E. I., and Peattie, R. A. (1995). Experimental investigation of steady flow in rigid models of abdominal aortic aneurysms. *Annals of biomedical engineering*, 23(1):29–39.
- Ashton, H., Gao, L., Kim, L., Druce, P., Thompson, S., and Scott, R. (2007). Fifteen-year follow-up of a randomized clinical trial of ultrasonographic screening for abdominal aortic aneurysms. *British journal of surgery*, 94(6):696–701.
- Aubry, N. (1991). On the hidden beauty of the proper orthogonal decomposition. *Theoretical and Computational Fluid Dynamics*, 2(5-6):339–352.
- Aubry, N., Guyonnet, R., and Lima, R. (1991). Spatiotemporal analysis of complex signals: Theory and applications. *Journal of Statistical Physics*, 64(3-4):683–739.
- Ballarin, F., Faggiano, E., Ippolito, S., Manzoni, A., Quarteroni, A., Rozza, G., and Scrofani, R. (2016). Fast simulations of patient-specific haemodynamics of coronary artery bypass grafts based on a POD–Galerkin method and a vascular shape parametrization. *Journal of Computational Physics*, 315:609–628.
- Barker, A. J., van Ooij, P., Bandi, K., Garcia, J., Albaghdadi, M., McCarthy, P., Bonow, R. O., Carr, J., Collins, J., Malaisrie, S. C., et al. (2014). Viscous energy loss in the presence of abnormal aortic flow. *Magnetic resonance in medicine*, 72(3):620–628.
- Batchelor, C. K. (2000). *An introduction to fluid dynamicss*. Cambridge university press.
- Baxter, B. T., Terrin, M. C., and Dalman, R. L. (2008). Medical management of small abdominal aortic aneurysms. *Circulation*, 117(14):1883–1889.

- Benard, N., Jarny, S., and Coisne, D. (2007). Definition of an experimental blood like fluid for laser measurements in cardiovascular studies. *Applied Rheology*, 17(4):44251–1.
- Berkooz, G., Holmes, P., and Lumley, J. L. (1993). The proper orthogonal decomposition in the analysis of turbulent flows. *Annual review of fluid mechanics*, 25(1):539–575.
- Biglino, G., Verschuere, P., Zegels, R., Taylor, A. M., and Schievano, S. (2013). Rapid prototyping compliant arterial phantoms for in-vitro studies and device testing. *Journal of Cardiovascular Magnetic Resonance*, 15(1):2.
- Binter, C., Gülan, U., Holzner, M., and Kozerke, S. (2016). On the accuracy of viscous and turbulent loss quantification in stenotic aortic flow using phase-contrast MRI. *Magnetic resonance in medicine*, 76(1):191–196.
- Bluestein, D., Niu, L., Schoepfoerster, R., and Dewanjee, M. (1996). Steady flow in an aneurysm model: correlation between fluid dynamics and blood platelet deposition.
- Brewster, D. C., Cronenwett, J. L., Hallett Jr, J. W., Johnston, K. W., Krupski, W. C., and Matsumura, J. S. (2003). Guidelines for the treatment of abdominal aortic aneurysms: report of a subcommittee of the Joint Council of the American Association for Vascular Surgery and Society for Vascular Surgery. *Journal of vascular surgery*, 37(5):1106–1117.
- Brindise, M. C., Busse, M. M., and Vlachos, P. P. (2018). Density-and viscosity-matched Newtonian and non-Newtonian blood-analog solutions with PDMS refractive index. *Experiments in fluids*, 59(11):173.
- Brooks, D., Goodwin, J., and Seaman, G. (1970). Interactions among erythrocytes under shear. *Journal of Applied Physiology*, 28(2):172–177.
- Brownrigg, J., De Bruin, J., Rossi, L., Karthikesalingam, A., Patterson, B., Holt, P., Hinchliffe, R., Morgan, R., Loftus, I., and Thompson, M. (2015). Endovascular aneurysm sealing for infrarenal abdominal aortic aneurysms: 30-day outcomes of 105 patients in a single centre. *European Journal of Vascular and Endovascular Surgery*, 50(2):157–164.
- Budwig, R. (1994). Refractive index matching methods for liquid flow investigations. *Experiments in fluids*, 17(5):350–355.
- Chang, G. H., Schirmer, C. M., and Modarres-Sadeghi, Y. (2017). A reduced-order model for wall shear stress in abdominal aortic aneurysms by proper orthogonal decomposition. *Journal of Biomechanics*, 54:33–43.
- Charonko, J. J., Kumar, R., Stewart, K., Little, W. C., and Vlachos, P. P. (2013). Vortices formed on the mitral valve tips aid normal left ventricular filling. *Annals of biomedical engineering*, 41(5):1049–1061.
- Chung, J. (2018). Epidemiology, risk factors, pathogenesis, and natural history of abdominal aortic aneurysm.
- Cloonan, A. J., Shahmirzadi, D., Li, R. X., Doyle, B. J., Konofagou, E. E., and McGloughlin, T. M. (2014). 3D-printed tissue-mimicking phantoms for medical imaging and computational validation applications. *3D printing and additive manufacturing*, 1(1):14–23.

- Darling, R., Messina, C., Brewster, D., and Ottinger, L. (1977). Autopsy study of unoperated abdominal aortic aneurysms. The case for early resection. *Circulation*, 56(3 Suppl):II161–4.
- Deplano, V., Guivier-Curien, C., and Bertrand, E. (2016). 3D analysis of vortical structures in an abdominal aortic aneurysm by stereoscopic PIV. *Experiments in Fluids*, 57(11):167.
- Deplano, V., Knapp, Y., Bailly, L., and Bertrand, E. (2014). Flow of a blood analogue fluid in a compliant abdominal aortic aneurysm model: Experimental modelling. *Journal of biomechanics*, 47(6):1262–1269.
- Deplano, V., Knapp, Y., Bertrand, E., and Gaillard, E. (2007). Flow behaviour in an asymmetric compliant experimental model for abdominal aortic aneurysm. *Journal of biomechanics*, 40(11):2406–2413.
- Di Labbio, G. (2019). *On left ventricular fluid dynamics associated with progressive chronic aortic regurgitatio*. PhD thesis, Concordia University.
- Di Labbio, G. and Kadem, L. (2018). Jet collisions and vortex reversal in the human left ventricle. *Journal of biomechanics*, 78:155–160.
- Di Labbio, G. and Kadem, L. (2019). Reduced-order modeling of left ventricular flow subject to aortic valve regurgitation. *Physics of Fluids*, 31(3):031901.
- Doyle, B. J., Morris, L. G., Callanan, A., Kelly, P., Vorp, D. A., and McGloughlin, T. M. (2008). 3D reconstruction and manufacture of real abdominal aortic aneurysms: from CT scan to silicone model. *Journal of biomechanical engineering*, 130(3).
- Dua, M. M. and Dalman, R. L. (2010). Hemodynamic influences on abdominal aortic aneurysm disease: Application of biomechanics to aneurysm pathophysiology. *Vascular pharmacology*, 53(1-2):11–21.
- Egelhoff, C., Budwig, R., Elger, D., Khraishi, T., and Johansen, K. (1999). Model studies of the flow in abdominal aortic aneurysms during resting and exercise conditions. *Journal of biomechanics*, 32(12):1319–1329.
- Engelhard, S., Voorneveld, J., Vos, H. J., Westenberg, J. J., Gijzen, F. J., Taimr, P., Versluis, M., de Jong, N., Bosch, J. G., Reijnen, M. M., et al. (2018). High-frame-rate contrast-enhanced US particle image velocimetry in the abdominal aorta: first human results. *Radiology*, 289(1):119–125.
- Erbel, R. and Eggebrecht, H. (2006). Aortic dimensions and the risk of dissection. *Heart*, 92(1):137–142.
- Espinosa, G., Marchiori, E., Araújo, A. P. d., Caramalho, M. F., and Barzola, P. (2002). Abdominal aorta morphometric study for endovascular treatment of aortic aneurysms: comparison between spiral CT and angiography. *Brazilian Journal of Cardiovascular Surgery*, 17(4):323–330.
- Etebari, A. and Vlachos, P. P. (2005). Improvements on the accuracy of derivative estimation from DPIV velocity measurements. *Experiments in Fluids*, 39(6):1040–1050.

- Fahraeus, R. and Lindqvist, T. (1931). The viscosity of the blood in narrow capillary tubes. *American Journal of Physiology-Legacy Content*, 96(3):562–568.
- Filardo, G., Powell, J. T., Martinez, M. A.-M., and Ballard, D. J. (2015). Surgery for small asymptomatic abdominal aortic aneurysms. *Cochrane Database of Systematic Reviews*, (2).
- Finol, E. A. and Amon, C. H. (2001). Blood flow in abdominal aortic aneurysms: pulsatile flow hemodynamics. *J. Biomech. Eng.*, 123(5):474–484.
- Fraser, K. H., Meagher, S., Blake, J. R., Easson, W. J., and Hoskins, P. R. (2008). Characterization of an abdominal aortic velocity waveform in patients with abdominal aortic aneurysm. *Ultrasound in medicine & biology*, 34(1):73–80.
- Garcia, D., Pibarot, P., Dumesnil, J. G., Sakr, F., and Durand, L.-G. (2000). Assessment of aortic valve stenosis severity: a new index based on the energy loss concept. *Circulation*, 101(7):765–771.
- Gopalakrishnan, S. S., Pier, B., and Biesheuvel, A. (2014). Dynamics of pulsatile flow through model abdominal aortic aneurysms.
- Grinberg, L., Yakhot, A., and Karniadakis, G. E. (2009). Analyzing transient turbulence in a stenosed carotid artery by proper orthogonal decomposition. *Annals of Biomedical Engineering*, 37(11):2200–2217.
- Guibert, R., Mcleod, K., Caiazzo, A., Mansi, T., Fernández, M. A., Sermesant, M., Pennec, X., Vignon-Clementel, I. E., Boudjemline, Y., and Gerbeau, J.-F. (2014). Group-wise construction of reduced models for understanding and characterization of pulmonary blood flows from medical images. *Medical image analysis*, 18(1):63–82.
- Hager, A., Kaemmerer, H., Rapp-Bernhardt, U., Blücher, S., Rapp, K., Bernhardt, T. M., Galanski, M., and Hess, J. (2002). Diameters of the thoracic aorta throughout life as measured with helical computed tomography. *The Journal of thoracic and cardiovascular surgery*, 123(6):1060–1066.
- Harter, L. P., Gross, B. H., Callen, P. W., and Barth, R. A. (1982). Ultrasonic evaluation of abdominal aortic thrombus. *Journal of Ultrasound in Medicine*, 1(8):315–318.
- He, C. M. and Roach, M. R. (1994). The composition and mechanical properties of abdominal aortic aneurysms. *Journal of vascular surgery*, 20(1):6–13.
- Hirsch, A. T., Haskal, Z. J., Hertzner, N. R., Bakal, C. W., Creager, M. A., Halperin, J. L., Hiratzka, L. F., Murphy, W. R., Olin, J. W., Puschett, J. B., et al. (2006). ACC/AHA 2005 practice guidelines for the management of patients with peripheral arterial disease (lower extremity, renal, mesenteric, and abdominal aortic) a collaborative report from the American Association for Vascular Surgery/Society for Vascular Surgery,* Society for Cardiovascular Angiography and Interventions, Society for Vascular Medicine and Biology, Society of Interventional Radiology, and the ACC/AHA Task Force on Practice Guidelines (writing committee to develop guidelines for the management of patients with peripheral arterial disease): endorsed by the American Association of Cardiovascular and Pulmonary Rehabilitation; National Heart, Lung, and Blood Institute; Society for Vascular Nursing; TransAtlantic Inter-Society Consensus; and Vascular Disease Foundation. *circulation*, 113(11):e463–e654.

- Isselbacher, E. M. (2005). Thoracic and abdominal aortic aneurysms. *Circulation*, 111(6):816–828.
- Joly, F., Soulez, G., Lessard, S., Kauffmann, C., and Vignon-Clementel, I. (2020). A cohort longitudinal study identifies morphology and hemodynamics predictors of abdominal aortic aneurysm growths. *Annals of Biomedical Engineering*, 48(2):606–623.
- Karkos, C., Mukhopadhyay, U., Papakostas, I., Ghosh, J., Thomson, G., and Hughes, R. (2000). Abdominal aortic aneurysm: the role of clinical examination and opportunistic detection. *European Journal of Vascular and Endovascular Surgery*, 19(3):299–303.
- Kefayati, S. and Poepping, T. L. (2013). Transitional flow analysis in the carotid artery bifurcation by proper orthogonal decomposition and particle image velocimetry. *Medical engineering & physics*, 35(7):898–909.
- Kemmerling, E. M. and Peattie, R. A. (2018). Abdominal Aortic Aneurysm Pathomechanics: Current Understanding and Future Directions. In *Molecular, Cellular, and Tissue Engineering of the Vascular System*, pages 157–179. Springer.
- Khe, A. K., Chupakhin, A. P., Cherevko, A. A., Eliava, S. S., and Pilipenko, Y. V. (2015). Viscous dissipation energy as a risk factor in multiple cerebral aneurysms. *Russian Journal of Numerical Analysis and Mathematical Modelling*, 30(5):277–287.
- Kleinstreuer, C. and Li, Z. (2006). Analysis and computer program for rupture-risk prediction of abdominal aortic aneurysms. *BioMedical Engineering OnLine*, 5(1):19.
- Kobeissi, E., Hibino, M., Pan, H., and Aune, D. (2019). Blood pressure, hypertension and the risk of abdominal aortic aneurysms: a systematic review and meta-analysis of cohort studies.
- Ku, D. N. (1997). Blood flow in arteries. *Annual review of fluid mechanics*, 29(1):399–434.
- Kung, E. O., Les, A. S., Medina, F., Wicker, R. B., McConnell, M. V., and Taylor, C. A. (2011). In vitro validation of finite-element model of AAA hemodynamics incorporating realistic outlet boundary conditions. *Journal of biomechanical engineering*, 133(4).
- Lasheras, J. C. (2007). The biomechanics of arterial aneurysms. *Annu. Rev. Fluid Mech.*, 39:293–319.
- LaVision, G. (2007). DaVis FlowMaster software manual for DaVis 7.2.
- Les, A. S., Shadden, S. C., Figueroa, C. A., Park, J. M., Tedesco, M. M., Herfkens, R. J., Dalman, R. L., and Taylor, C. A. (2010a). Quantification of hemodynamics in abdominal aortic aneurysms during rest and exercise using magnetic resonance imaging and computational fluid dynamics. *Annals of biomedical engineering*, 38(4):1288–1313.
- Les, A. S., Yeung, J. J., Schultz, G. M., Herfkens, R. J., Dalman, R. L., and Taylor, C. A. (2010b). Supraceliac and infrarenal aortic flow in patients with abdominal aortic aneurysms: mean flows, waveforms, and allometric scaling relationships. *Cardiovascular engineering and technology*, 1(1):39–51.
- Leung, J. H., Wright, A. R., Cheshire, N., Crane, J., Thom, S. A., Hughes, A. D., and Xu, Y. (2006). Fluid structure interaction of patient specific abdominal aortic aneurysms: a comparison with solid stress models. *Biomedical engineering online*, 5(1):33.

- Lo, R. C., Bensley, R. P., Hamdan, A. D., Wyers, M., Adams, J. E., Schermerhorn, M. L., of New England, V. S. G., et al. (2013). Gender differences in abdominal aortic aneurysm presentation, repair, and mortality in the Vascular Study Group of New England. *Journal of vascular surgery*, 57(5):1261–1268.
- Long, A., Rouet, L., Lindholt, J. S., and Allaire, E. (2012). Measuring the maximum diameter of native abdominal aortic aneurysms: review and critical analysis. *European Journal of Vascular and Endovascular Surgery*, 43(5):515–524.
- Lozowy, R. (2017). Hemodynamics in abdominal aorta aneurysms.
- Lumley, J. L. (1967). The structure of inhomogeneous turbulent flows. *Atmospheric turbulence and radio wave propagation*.
- Manzoni, A., Quarteroni, A., and Rozza, G. (2012). Model reduction techniques for fast blood flow simulation in parametrized geometries. *International journal for numerical methods in biomedical engineering*, 28(6-7):604–625.
- Marconi, S., Lanzarone, E., van Bogerijen, G. H., Conti, M., Secchi, F., Trimarchi, S., and Auricchio, F. (2018). A compliant aortic model for in vitro simulations: Design and manufacturing process. *Medical engineering & physics*, 59:21–29.
- McGregor, R., Szczerba, D., von Siebenthal, M., Muralidhar, K., and Székely, G. (2008). Exploring the use of proper orthogonal decomposition for enhancing blood flow images via computational fluid dynamics. In *International Conference on Medical Image Computing and Computer-Assisted Intervention*, pages 782–789. Springer.
- Mendez, M., Balabane, M., and Buchlin, J.-M. (2018). Multi-scale proper orthogonal decomposition of complex fluid flows. *arXiv preprint arXiv:1804.09646*.
- Mix, D. S., Stoner, M. C., Day, S. W., and Richards, M. S. (2018). Manufacturing abdominal aorta hydrogel tissue-mimicking phantoms for ultrasound elastography validation. *JoVE (Journal of Visualized Experiments)*, (139):e57984.
- Moore Jr, J., Ku, D., Zarins, C., and Glagov, S. (1992). Pulsatile flow visualization in the abdominal aorta under differing physiologic conditions: implications for increased susceptibility to atherosclerosis.
- Naidich, T. P., Altman, N. R., and Gonzalez-Arias, S. M. (1993). Phase contrast cine magnetic resonance imaging: normal cerebrospinal fluid oscillation and applications to hydrocephalus. *Neurosurgery Clinics of North America*, 4(4):677–705.
- Olsen, P. S., Schroeder, T., Perko, M., Røder, O. C., Agerskov, K., Sørensen, S., and Lorentzen, J. E. (1990). Renal failure after operation for abdominal aortic aneurysm. *Annals of vascular surgery*, 4(6):580–583.
- Olufsen, M. S., Peskin, C. S., Kim, W. Y., Pedersen, E. M., Nadim, A., and Larsen, J. (2000). Numerical simulation and experimental validation of blood flow in arteries with structured-tree outflow conditions. *Annals of biomedical engineering*, 28(11):1281–1299.

- on Preventive Health Care, C. T. F. (2017). Recommendations on screening for abdominal aortic aneurysm in primary care. *CMAJ*, 189(36):E1137–E1145.
- Owens, D. K., Davidson, K. W., Krist, A. H., Barry, M. J., Cabana, M., Caughey, A. B., Doubeni, C. A., Epling, J. W., Kubik, M., Landefeld, C. S., et al. (2019). Screening for abdominal aortic aneurysm: US Preventive Services Task Force recommendation statement. *Jama*, 322(22):2211–2218.
- Peattie, R. A., Asbury, C. L., Bluth, E. I., and Riehle, T. J. (1996). Steady flow in models of abdominal aortic aneurysms. Part II: Wall stresses and their implication for in vivo thrombosis and rupture. *Journal of ultrasound in medicine*, 15(10):689–696.
- Peattie, R. A., Riehle, T. J., and Bluth, E. I. (2004). Pulsatile flow in fusiform models of abdominal aortic aneurysms: flow fields, velocity patterns and flow-induced wall stresses. *J. Biomech. Eng.*, 126(4):438–446.
- Pedersen, E. M., Yoganathan, A. P., and Lefebvre, X. P. (1992). Pulsatile flow visualization in a model of the human abdominal aorta and aortic bifurcation. *Journal of biomechanics*, 25(8):935–944.
- Pedrizzetti, G. and Domenichini, F. (2005). Nature optimizes the swirling flow in the human left ventricle. *Physical review letters*, 95(10):108101.
- Pedrizzetti, G., Domenichini, F., and Tonti, G. (2010). On the left ventricular vortex reversal after mitral valve replacement. *Annals of biomedical engineering*, 38(3):769–773.
- Poelma, C., Watton, P. N., and Ventikos, Y. (2015). Transitional flow in aneurysms and the computation of haemodynamic parameters. *Journal of The Royal Society Interface*, 12(105):20141394.
- Polanczyk, A., Podgorski, M., Polanczyk, M., Piechota-Polanczyk, A., Neumayer, C., and Stefanczyk, L. (2018). A Novel patient-specific human cardiovascular system phantom (HCSP) for reconstructions of pulsatile blood hemodynamic inside abdominal aortic aneurysm. *IEEE Access*, 6:61896–61903.
- Raffel, M., Willert, C. E., Scarano, F., Kähler, C. J., Wereley, S. T., and Kompenhans, J. (2018). *Particle image velocimetry: a practical guide*. Springer.
- Raghavan, M. L., Hanaoka, M. M., Kratzberg, J. A., de Lourdes Higuchi, M., and Da Silva, E. S. (2011). Biomechanical failure properties and microstructural content of ruptured and unruptured abdominal aortic aneurysms. *Journal of biomechanics*, 44(13):2501–2507.
- Rawat, D. S., Pourquie, M., and Poelma, C. (2019). Numerical investigation of turbulence in abdominal aortic aneurysms. *Journal of biomechanical engineering*, 141(6).
- Sakalihasan, N., Michel, J.-B., Katsargyris, A., Kuivaniemi, H., Defraigne, J.-O., Nchimi, A., Powell, J. T., Yoshimura, K., and Hultgren, R. (2018). Abdominal aortic aneurysms. *Nature reviews Disease primers*, 4(1):1–22.
- Salsac, A.-V. (2006). *Changes in the hemodynamic stresses occurring during the enlargement of abdominal aortic aneurysms*. PhD thesis, University of California, San Diego.

- Scarano, F. and Riethmuller, M. L. (2000). Advances in iterative multigrid PIV image processing. *Experiments in Fluids*, 29(1):S051–S060.
- Scharnowski, S., Grayson, K., de Silva, C. M., Hutchins, N., Marusic, I., and Kähler, C. J. (2017). Generalization of the PIV loss-of-correlation formula introduced by Keane and Adrian. *Experiments in Fluids*, 58(10):150.
- Schermerhorn, M. (2009). A 66-year-old man with an abdominal aortic aneurysm: review of screening and treatment. *JAMA*, 302(18):2015–2022.
- Sciacchitano, A. (2019). Uncertainty quantification in particle image velocimetry. *Measurement Science and Technology*, 30(9):092001.
- Sciacchitano, A., Neal, D. R., Smith, B. L., Warner, S. O., Vlachos, P. P., Wieneke, B., and Scarano, F. (2015). Collaborative framework for PIV uncertainty quantification: comparative assessment of methods. *Measurement Science and Technology*, 26(7):074004.
- Shankaran, H., Alexandridis, P., and Neelamegham, S. (2003). Aspects of hydrodynamic shear regulating shear-induced platelet activation and self-association of von Willebrand factor in suspension. *Blood, The Journal of the American Society of Hematology*, 101(7):2637–2645.
- Shum, J., Martufi, G., Di Martino, E., Washington, C. B., Grisafi, J., Muluk, S. C., and Finol, E. A. (2011). Quantitative assessment of abdominal aortic aneurysm geometry. *Annals of biomedical engineering*, 39(1):277–286.
- Sirovich, L. (1987). Turbulence and the dynamics of coherent structures. I. Coherent structures. *Quarterly of applied mathematics*, 45(3):561–571.
- Stamatopoulos, C., Mathioulakis, D., Papaharilaou, Y., and Katsamouris, A. (2011). Experimental unsteady flow study in a patient-specific abdominal aortic aneurysm model. *Experiments in fluids*, 50(6):1695–1709.
- Stugaard, M., Koriyama, H., Katsuki, K., Masuda, K., Asanuma, T., Takeda, Y., Sakata, Y., Itatani, K., and Nakatani, S. (2015). Energy loss in the left ventricle obtained by vector flow mapping as a new quantitative measure of severity of aortic regurgitation: a combined experimental and clinical study. *European Heart Journal-Cardiovascular Imaging*, 16(7):723–730.
- Sweeting, M., Thompson, S., Brown, L., Powell, J., and collaborators, R. (2012). Meta-analysis of individual patient data to examine factors affecting growth and rupture of small abdominal aortic aneurysms. *British Journal of Surgery*, 99(5):655–665.
- Taira, K., Brunton, S. L., Dawson, S. T., Rowley, C. W., Colonius, T., McKeon, B. J., Schmidt, O. T., Gordeyev, S., Theofilis, V., and Ukeiley, L. S. (2017). Modal analysis of fluid flows: An overview. *Aiaa Journal*, 55(12):4013–4041.
- Takagi, H., Umemoto, T., of Cardiovascular Evidence) Group, A. A.-L. I., et al. (2017). Association of hypertension with abdominal aortic aneurysm expansion. *Annals of vascular surgery*, 39:74–89.
- Taylor, C. A., Hughes, T. J., and Zarins, C. K. (1998). Finite element modeling of three-dimensional pulsatile flow in the abdominal aorta: relevance to atherosclerosis. *Annals of biomedical engineering*, 26(6):975–987.

- Taylor, T. W. and Yamaguchi, T. (1994). Three-dimensional simulation of blood flow in an abdominal aortic aneurysm—steady and unsteady flow cases. *Journal of biomechanical engineering*, 116(1):89–97.
- Timmins, B. H., Wilson, B. W., Smith, B. L., and Vlachos, P. P. (2012). A method for automatic estimation of instantaneous local uncertainty in particle image velocimetry measurements. *Experiments in fluids*, 53(4):1133–1147.
- Towne, A., Schmidt, O. T., and Colonius, T. (2017). Spectral proper orthogonal decomposition and its relationship to dynamic mode decomposition and resolvent analysis. *arXiv preprint arXiv:1708.04393*.
- Van Noort, K., Holewijn, S., Schuurmann, R. C., Boersen, J. T., Overeem, S. P., Jebbink, E. G., Vermeulen, J. J., Reijnen, M. M., Slump, C. H., and de Vries, J.-P. P. (2018). Effect of abdominal aortic endoprostheses on arterial pulse wave velocity in an in vitro abdominal aortic flow model. *Physiological measurement*, 39(10):104001.
- Vitello, D. J., Ripper, R. M., Fettiplace, M. R., Weinberg, G. L., and Vitello, J. M. (2015). Blood density is nearly equal to water density: a validation study of the gravimetric method of measuring intraoperative blood loss. *Journal of veterinary medicine*, 2015.
- Vlachopoulos, C., O'Rourke, M., and Nichols, W. W. (2011). *McDonald's blood flow in arteries: theoretical, experimental and clinical principles*. CRC press.
- Vorp, D. A. (2007). Biomechanics of abdominal aortic aneurysm. *Journal of biomechanics*, 40(9):1887–1902.
- Wang, L. J., Prabhakar, A. M., and Kwolek, C. J. (2018a). Current status of the treatment of infrarenal abdominal aortic aneurysms. *Cardiovascular diagnosis and therapy*, 8(Suppl 1):S191.
- Wang, Y., Joannic, D., Juillion, P., Monnet, A., Delassus, P., Lalande, A., and Fontaine, J.-F. (2018b). Validation of the strain assessment of a phantom of abdominal aortic aneurysm: comparison of results obtained from magnetic resonance imaging and stereovision measurements. *Journal of biomechanical engineering*, 140(3).
- Wang, Y., Joannic, D., Patrick, J., Keromnes, A., Aurélien, M., Lalande, A., and Fontaine, J.-F. (2016). Comparison of Flow Measurement by 4D Flow Magnetic Resonance Imaging and by Particles Image Velocimetry on Phantom of Abdominal Aortic Aneurysm.
- Wanhainen, A., Verzini, F., Van Herzele, I., Allaire, E., Bown, M., Cohnert, T., Dick, F., van Herwaarden, J., Karkos, C., Koelemay, M., et al. (2019). Editor's choice—European society for vascular surgery (ESVS) 2019 clinical practice guidelines on the management of abdominal aorto-iliac artery aneurysms. *European Journal of Vascular and Endovascular Surgery*, 57(1):8–93.
- Wassef, M., Upchurch Jr, G. R., Kuivaniemi, H., Thompson, R. W., and Tilson III, M. (2007). Challenges and opportunities in abdominal aortic aneurysm research. *Journal of vascular surgery*, 45(1):192–198.
- Westerweel, J. (1994). Efficient detection of spurious vectors in particle image velocimetry data. *Experiments in Fluids*, 16(3-4):236–247.

- Westerweel, J. and Scarano, F. (2005). Universal outlier detection for PIV data. *Experiments in fluids*, 39(6):1096–1100.
- Wieneke, B. (2015). PIV uncertainty quantification from correlation statistics. *Measurement Science and Technology*, 26(7):074002.
- Wilmink, A., Hubbard, C. S., Day, N., and Quick, C. (2001). The incidence of small abdominal aortic aneurysms and the change in normal infrarenal aortic diameter: implications for screening. *European Journal of Vascular and Endovascular Surgery*, 21(2):165–170.
- Xue, Z., Charonko, J. J., and Vlachos, P. P. (2014). Particle image velocimetry correlation signal-to-noise ratio metrics and measurement uncertainty quantification. *Measurement Science and Technology*, 25(11):115301.
- Yip, T. and Yu, S. (2002). Oscillatory flows in straight tubes with an axisymmetric bulge. *Experimental thermal and fluid science*, 26(8):947–961.
- Yousif, M. Y., Holdsworth, D. W., and Poepping, T. L. (2011). A blood-mimicking fluid for particle image velocimetry with silicone vascular models. *Experiments in fluids*, 50(3):769–774.
- Yu, S. (2000). Steady and pulsatile flow studies in abdominal aortic aneurysm models using particle image velocimetry. *International journal of heat and fluid flow*, 21(1):74–83.
- Zhang, F., Lanning, C., Mazzaro, L., Barker, A. J., Gates, P. E., Strain, W. D., Fulford, J., Gosling, O. E., Shore, A. C., Bellenger, N. G., et al. (2011). In vitro and preliminary in vivo validation of echo particle image velocimetry in carotid vascular imaging. *Ultrasound in medicine & biology*, 37(3):450–464.
- Ziegler, M., Welander, M., Lantz, J., Lindenberger, M., Bjarnegård, N., Karlsson, M., Ebbers, T., Länne, T., and Dyverfeldt, P. (2019). Visualizing and quantifying flow stasis in abdominal aortic aneurysms in men using 4D flow MR. *Magnetic resonance imaging*, 57:103–110.